NASA CK-17716

NASA Contractor Report 174760

NASA-CR-174760
19840024320

A Theoretical and Experimental Study
of Turbulent Evaporating Sprays

A.S.P. Solomon, J-S. Shuen, Q-F. Zhang and G. M. Faeth

The Pennsylvania State University
University Park, Pennsylvania

September 1984

Prepared for

A Theoretical and Experimental Study
of Turbulent Evaporating Sprays

SUMMARY

A study of the structure of sprays, limited to the properties of evaporating sprays, is described. Several models of these processes were evaluated by comparison of predictions with new measurements in evaporating sprays completed during this investigation. Analysis and measurements were limited to the dilute portions of the flows, where the volume fraction of the continuous phase was greater than 99.1%.

Three models of the process were evaluated: (1) a locally homogeneous flow (LHF) model, where slip between the phases was neglected and the flow was assumed to be in local thermodynamic equilibrium; (2) a deterministic separated flow (DSF) model, where slip was considered but effects of turbulent fluctuations on interphase transport rates and drop dispersion by the turbulence were ignored; and (3) a stochastic separated flow (SSF) model, where effects of interphase slip, turbulent fluctuations and turbulent dispersion were considered using random sampling for turbulence properties in conjunction with random-walk computations for drop motion. All three models used a k-ε model which was extensively evaluated for constant and variable density single-phase jets during earlier work in this laboratory.

The new experiments employed Freon 11 sprays, produced by an air-atomizing injector in a still environment. Mean and fluctuating velocities and Reynolds stress were measured in the continuous phase using laser Doppler anemometry. Liquid mass fluxes were measured by slide impaction. Drop sizes were measured by slide impaction and photography. Simultaneous measurements of drop size and velocity were obtained using a multiflash photographic technique. Mean concentration of injected fluid was measured by isokinetic sampling and analysis with a gas chromatograph. Mean gas-phase temperatures were measured using shielded fine-wire thermocouples.

The LHF and DSF models did not provide very satisfactory predictions over the present measurements. The DSF model generally underestimated the rate of spread of the dispersed phase as a result of ignoring effects of turbulent dispersion. The LHF model provided reasonably good predictions for flows containing small drops, but was unsatisfactory for most practical flows. In earlier evaluations, LHF models generally overestimate the rate of spread of dispersed phases due to neglect of slip. However, the LHF model underestimated spread rates for the present evaporating sprays. This indicates that LHF models do not always provide an upper bound on the rate of development of dilute drop-laden flows--as suggested in the past. Differences between measurements and predictions of the DSF and LHF models were smaller than observed for nonevaporating sprays, however, since decreasing mass of the dispersed phase by evaporation causes the flow to approach a single-phase flow.

In contrast to the other models, the SSF model provided reasonably good predictions of the present measurements. While this result is encouraging, uncertainties in initial conditions for some of the data limits the thoroughness of the evaluation of the SSF model. Some effects of drops on turbulence properties were observed in dense regions of the sprays. Treatment of such dense flow effects will require extension of the present SSF model. The SSF approach, however, appears to provide an attractive formulation for treating nonlinear interphase transport processes in drop-laden turbulent flows. Current work in this laboratory is considering extension of the method to combusting sprays as well as consideration of effects of turbulence modulation.

TABLE OF CONTENTS

iv

NOMENCLATURE

Symbol	Description
a	acceleration of gravity
B	mass transfer driving potential, Equation (2.20)
c_f	drop concentration
C_D	drag coefficient
C_i	parameters in turbulence model
C_p	specific heat at constant pressure
d	injector diameter
d_p	drop diameter
D	mass diffusivity
f	mixture fraction
g	square of mixture fraction or gas-phase mass fraction fluctuations
G	liquid mass flux
h	heat transfer coefficient
h_i	enthalpy of species i
k	turbulence kinetic energy
L_e	dissipation length scale
m	drop mass
$\dot{m}$	mass flow rate
$\dot{m}''$	mass flux at drop surface
M_i	molecular weight of species i
n	number of drop groups
$\dot{n}_i$	number of drops per unit time in group i
N_P, N_S	convection correction, Equation (2.21)
p	pressure

P	probability density function (PDF)
Pr	Prandtl number
r	radial distance
R	ideal gas constant
Re	Reynolds number
Sc	Schmidt number
S_ϕ	source term
$S_{p\phi}$	drop source term
SMD	Sauter mean diameter
t	time
t_e	eddy lifetime
T	temperature
u	axial velocity
$\vec{u}_p$	drop velocity vector
v	radial velocity
v_i	specific volume of species i
V_j	volume of computational cell j
w	tangential velocity
x	axial distance
$\vec{x}_p$	drop position vector
$\Delta\vec{x}_p$	path length of drops in an eddy
Y_i	mass fraction of species i
Δt	time of drop residence in an eddy
α	average property factor, Equation (2.24)
ε	rate of dissipation of turbulence kinetic energy
μ	value of maximum probability
μ_t	turbulent viscosity

ρ	density
τ	drop relaxation time
σ_i	turbulent Prandtl/Schmidt number
ϕ	generic property
σ	standard deviation of PDF

Subscripts

a	air
avg	average value
c	centerline quantity
f	liquid-phase property
F	Freon-11
g	gas-phase property
i	drop group or coordinate direction
o	injector exit condition
p	drop property
s	drop surface condition
∞	ambient condition

Superscripts

$(\bar{\ })$	time-averaged quantity
$(\ )'$	time-averaged fluctuating quantity
$(\tilde{\ })$	Favre-averaged quantity
$(\ )''$	Favre-averaged fluctuating quantity
$(\vec{\ })$	vector quantity

1. INTRODUCTION

The objective of this investigation was to complete measurements of spray structure, useful for evaluation of models of the process. The work was motivated by the need for additional experimental information on sprays, as expressed in several recent reviews [1,2][1] The tests considered evaporating sprays, generated by an air-atomizing injector, in a still environment. This arrangement has simple geometry and well-defined boundary conditions, which facilitates model evaluation. Furthermore, evaporating sprays highlight effects of turbulence on drop dispersion and drop heat and mass transfer phenomena, as well as effects of drops on the properties of the continuous phase, while minimizing complications due to combustion. Data obtained in the present investigation was also used to begin model evaluation considering methods typical of recent spray models. The present report is part of a systematic investigation undertaken in this laboratory, to aid in spray model development and evaluation [3-11].

During the first phase of this investigation [3-6], models of particle-laden jets were developed and evaluated, using existing measurements in particle-laden jets available in the literature. While predictions for some models were encouraging, the evaluation was inhibited throughout by insufficient information concerning initial conditions. Moreover, the flow structure data available in the existing measurements were not complete in some cases, which further hindered model evaluation.

Subsequently, complete measurements of the structure of particle-laden jets were undertaken in this laboratory to supplement the data base of existing measurements in the literature [7,8]. The experiments considered dilute solid-particle-laden jets in a still environment, considering three particle-size groups and two loading ratios. Measurements included mean and fluctuating velocities of both phases, particle-mass fluxes, particle-size distributions, and calibration of particle drag properties. Particular attention was given to defining initial conditions of the flows, to obtain definitive evaluation of spray models. Simplified models ignoring either interphase slip or turbulent dispersion yielded poor agreement with the measurements [7,8]. In contrast, a stochastic separated flow model of the process, which treated effects of interphase slip and turbulent dispersion performed reasonably well over the new data base, encouraging its extension to liquid sprays.

The next phase of the study considered nonevaporating sprays injecting into a stagnant environment [6,9]. Mean and fluctuating velocities of the continuous phase were measured, using laser Doppler anemometry (LDA) techniques. Drop sizes were measured using the Fraunhofer diffraction and slide impaction methods. Liquid fluxes in the sprays were obtained using an isokinetic sampling probe. Model

---

[1]Number in brackets denote references.

evaluation was limited, however, due to lack of measurements of drop properties and incomplete initial conditions.

Subsequently, the nonevaporating spray work was extended by completing measurements of drop properties and initial conditions [10,11]. A multiflash photographic technique was employed to obtain simultaneous measurements of drop size and velocity in the entire spray. New predictions using typical recent spray models were then compared with the completed structure measurements to obtain a more convincing evaluation of the models. As in the case of the particle-laden jets [7,8], simplified models ignoring either turbulent dispersion of drops or slip between the phases performed poorly. On the other hand, the stochastic separated flow model, which included effects of slip and turbulent dispersion, predicted the structure of the nonevaporating sprays reasonably well [10,11]. A notable feature of the results was that the stochastic model performed quite well in spite of significant effects of turbulent dispersion exhibited by the sprays. There was no modification of the model from its original calibration for particle-laden jets (where effects of turbulent dispersion were not significant). These and other results [10,11] encouraged further extension of the stochastic model to evaporating sprays.

Existing data on the mean and turbulent structure of evaporating sprays is limited. A recent review discusses early work in the field [1]. Yule et al. [12] have since reported measurements in evaporating kerosene sprays from a twin-fluid injector in a coflowing stream which could be preheated. Measurements of particle size were undertaken using a laser tomographic light-scattering technique while mean drop and continuous-phase velocities were measured using LDA.

Tishkoff et al. [13,14] have also reported measurements for evaporating sprays. The system studied was an n-heptane spray from a solid cone atomizer which was injected into a low velocity, coaxial flow of air. The spray plume shape was studied using photographic, shadowgraph and light-scattering techniques. In addition, droplet-size distributions, liquid-phase volume fractions, and vapor-concentration measurements were made at two axial locations. Drop size and velocity measurements were obtained using an imaging technique.

The existing measurements in evaporating sprays are generally inadequate for evaluating spray models due to lack of complete information on flow structure, awkward flow configurations or incomplete characterization of injector properties. The present investigation seeks to provide data on evaporating sprays useful for evaluating spray models, by considering a simple spray configuration with well-defined initial and boundary conditions and relatively complete structure measurements. Predictions using typical recent spray models are also compared with the completed structure measurements, to gain further understanding of two-phase/turbulence interactions in evaporating situations.

The structure of sprays is generally influenced by turbulent dispersion of the discrete phase. Turbulent dispersion of drops is examined during this investigation by comparing predictions of several

theoretical models with the present measurements in evaporating sprays. Past models of turbulent particle-laden jets and sprays often consider two limiting cases instead of treating turbulent drop dispersion [1,2]. At one limit the drops and the continuous phase are assumed to have equal rates of turbulent diffusion. The locally homogeneous flow (LHF) approximation provides a consistent formulation of this limit. This implies that interphase transport rates are infinitely fast, so that both phases have the same velocity at each point in the flow. The LHF approximation provides best results for flows containing small drops, where characteristic response times of drops are small in comparison to characteristic times of turbulent fluctuations. LHF models have been extensively evaluated during earlier work in this laboratory, but only yielded accurate predictions for drop sizes smaller than most practical applications [15-17].

Turbulent drop dispersion is neglected entirely at the other limit. This implies that drops follow deterministic trajectories since they only interact with mean properties of the continuous phase, yielding a deterministic separated flow (DSF) model. Such an approximation is appropriate for flows containing large drops, where characteristic drop response times to flow disturbances are large in comparison to characteristic turbulent fluctuation times. Several spray models have been proposed along these lines, e.g., El Banhawy and Whitelaw [18], Mongia and Smith [19], Boyson and Swithenbank [20] , and Faeth and coworkers [1-11], among others [1]. Due to the complexities of sprays and uncertainties in initial conditions, however, the value of DSF models has not been clearly established as yet.

Most practical particle-laden flows exhibit properties between these limits and require consideration of turbulent particle dispersion. Early dispersion models, discussed by Yuu et al. [21] apply a gradient diffusion approximation with empirical correlations of turbulent particle exchange coefficients. This approach is not practical, however, since such exchange coefficients are influenced by both particle and turbulence properties--requiring excessive effort to accumulate a data base sufficient for general application of the method.

Several recent studies of turbulent drop dispersion use stochastic separated flow (SSF) methods to circumvent the limitations of the gradient diffusion approach. Stochastic analysis requires an estimate of the mean and turbulent properties of the continuous phase. Drop trajectories are then computed by random sampling to find instantaneous continuous phase properties. Mean and fluctuating drop properties are found by Monte Carlo methods--where a statistically significant number of drop trajectories are averaged to obtain system properties.

SSF models have been applied to particle-laden jets. Yuu et al. [21] use empirical correlations of mean and turbulent properties for SSF analysis of their particle dispersion measurements. Gosman and Ioannides [22] propose a more comprehensive approach, where flow properties for the stochastic calculations are computed with a k-ε turbulence model. This approach has been adopted by the present

authors in their study of particle-laden jets and sprays, after only minor modification [1-11].

In the following, the models are described first of all. Experimental methods used for measurements in evaporating sprays are then discussed. The report concludes with an evaluation of the models using the new spray measurements.

2. THEORY

2.1 Introduction

Three theoretical models of spray processes were considered: (1) a locally homogeneous flow (LHF) model, where slip between the phases is neglected and the flow is assumed to be in local thermodynamic equilibrium; (2) a deterministic separated flow (DSF) model, where slip and finite interphase transport rates are considered but effects of drop dispersion by turbulence and effects of turbulence on interphase transport rates are ignored; and (3) a stochastic separated flow (SSF) model, where effects of interphase slip, turbulent dispersion and turbulent fluctuations are considered using random sampling for turbulence properties in conjunction with random-walk computations for drop motion.

All models employ the widely adopted procedures of k-ε-g turbulence models for the gas phase, since this approach has been thoroughly calibrated during earlier work [1-11,15-17]. Major assumptions for the gas phase are: exchange coefficients of all species and heat are the same, buoyancy only affects the mean flow, and kinetic energy is negligible. Effects of buoyancy are generally small in practical sprays, and neglecting kinetic energy limits the model to low Mach number flows, which is appropriate for the test conditions to be examined as well as for most practical combustion chambers. The assumption of equal exchange coefficients is widely recognized as being acceptable for high Reynolds number turbulent flows typical of spray processes. Other assumptions will be described when introduced since they differ for each model.

In order to ensure adequate numerical closure with reasonable computation costs, the models are limited to boundary-layer flows with no recirculation. The present test flows are axisymmetric with no swirl; therefore, the analysis is posed accordingly. The advantage of these conditions is that they correspond to cases where the turbulence models were developed [23] and have high reliability.

2.2 Locally Homogeneous Flow Model

2.2.1 Governing Equations

The basic premise of the LHF model is that the rates of interphase transport are fast in comparison to the rate of development of the flow as a whole. This implies that all phases have the same velocity and temperature at each point in the flow.

Past formulations of the LHF model [15-17] use the Reynolds-averaged form of the governing equations. However, the Favre-averaged form of the equations has been proposed as a more formally correct treatment of the physical processes occurring in turbulent variable density and combusting flows [24]. Furthermore, the Favre-averaged form of the governing equations reduces to the Reynolds-averaged form for constant density flows. Jeng and Faeth [25] used the Favre-averaged equations and established a single set of turbulence model constants which satisfactorily predict both constant and variable density jets. Following Jeng and Faeth [25], the Favre-averaged governing equations for the LHF model based on the assumptions discussed in Section 2.1 are written as follows:

$$\frac{\partial}{\partial x}(\overline{\rho}\tilde{u}\tilde{\phi}) + \frac{1}{r}\frac{\partial}{\partial r}(r\overline{\rho}\tilde{v}\tilde{\phi}) = \frac{1}{r}\frac{\partial}{\partial r}\left(r\mu_{eff,\phi}\frac{\partial\tilde{\phi}}{\partial r}\right) + S_\phi \qquad (2.1)$$

where

$$\tilde{\phi} = \frac{\overline{\rho\phi}}{\overline{\rho}} \qquad (2.2)$$

is a Favre-averaged quantity and ϕ is a generic quantity. The conservation equations of mass ($\phi = 1$), momentum, mixture fraction, turbulent kinetic energy, rate of dissipation of turbulent kinetic energy and the square of the mixture fraction fluctuations are obtained using Equation (2.1) and the expressions for $\tilde{\phi}$, $\mu_{eff,\phi}$ and S_ϕ shown in Table 1 along with the appropriate empirical constants. The empirical constants were established for noncombusting and combusting single-phase flows and are not changed when sprays are considered [1,15-17,25].

The turbulent viscosity is calculated from the turbulent kinetic energy and the rate of dissipation as follows:

$$\mu_t = C_\mu \overline{\rho} \frac{k^2}{\varepsilon} \qquad (2.3)$$

2.2.2 State Relationships

Under the LHF approximation, the flow is equivalent to a single-phase flow and effects of the dispersed phase only appear in the representation of thermodynamic properties (temperature, density, enthalpy, etc.) and molecular transport properties (viscosity, thermal conductivity, etc.). The representation of these properties is generally called the state relationships for the flow. Finding state relationships for thermodynamic properties involves conventional adiabatic mixing calculations, with the local state of the mixture specified by the mixture fraction, $\tilde{f}$, (the fraction of material at a point which originated at the injector). State relationships used for the present LHF predictions for the case 1 and case 2 evaporating sprays followed past practice [1] and are summarized in Appendix B.

6

Table 1.   Source Terms in Equation (2.1)

$\tilde{\phi}$	$\mu_{eff,\phi}$	S_ϕ
1	--	0
$\tilde{u}$	$\mu + \mu_t$	$a(\rho_\infty - \bar{\rho})$
$\tilde{f}$	$(\mu/Sc) + (\mu_t/\sigma_f)$	0
k	$\mu + (\mu_t/\sigma_k)$	$\mu_t \left(\frac{\partial \tilde{u}}{\partial r}\right)^2 - \bar{\rho}\varepsilon$
ε	$\mu + (\mu_t/\sigma_\varepsilon)$	$\left(C_{\varepsilon 1}\mu_t\left(\frac{\partial \tilde{u}}{\partial r}\right)^2 - C_{\varepsilon 2}\bar{\rho}\varepsilon\right)(\varepsilon/k)$
g	$(\mu/SC) + (\mu_t/\sigma_g)$	$C_{g1}\mu_t\left(\frac{\partial \tilde{f}}{\partial r}\right)^2 - C_{g2}\bar{\rho}g\varepsilon/k$

C_μ	$C_{\varepsilon 1}$	C_{g1}	$C_{\varepsilon 2}=C_{g2}$	σ_k	σ_ε	$\sigma_f=\sigma_g$	Sc
0.09	1.44	2.8	1.87	1.0	1.3	0.7	0.7

With equal exchange coefficients, instantaneous properties are only a function of mixture fraction. This allows determination of all scalar properties (temperature, composition and density), as a function of mixture fraction—once and for all [1,23]. The mass-averaged mean and variance of the flow properties are then found from the mass-averaged probability density function for mixture fraction, $\tilde{P}(f)$ as follows [24,25]

$$\tilde{\phi} = \frac{\overline{\rho\phi}}{\overline{\rho}} = \int_0^1 \phi(f)\ \tilde{P}(f)\ df \tag{2.4}$$

$$\phi''^2 = \frac{\overline{\rho\phi''^2}}{\overline{\rho}} = \int_0^1 (\phi(f) - \tilde{\phi})^2\ \tilde{P}(f)\ df \tag{2.5}$$

where $\overline{\rho}$ is obtained from

$$\overline{\rho} = \left(\int_0^1 \frac{1}{\rho(f)}\ \tilde{P}(f)\ df\right)^{-1} \tag{2.6}$$

Similarly, time-averaged means and variances are expressed as follows:

$$\overline{\phi} = \overline{\rho} \int_0^1 \left(\phi(f)/\rho(f)\right)\ \tilde{P}(f)\ df \tag{2.7}$$

$$\overline{\phi'^2} = \int_0^1 \frac{1}{\rho(f)}\ \left(\phi(f) - \tilde{\phi}(f)\right)^2\ \tilde{P}(f)\ df \tag{2.8}$$

In Equations (2.4) and (2.5), $\phi(f)$ is known from the state relationships, cf., Appendix B. A functional form must be assumed for $\tilde{P}(f)$, although the specific form used has little effect on predictions. A clipped Gaussian function [24,25] was employed for the Favre probability density function, $\tilde{P}(f)$. $\tilde{P}(f)$ depends on the most probable value μ and the standard deviation σ of the distribution which can be found from the local values of $\tilde{f}$ and g as follows:

$$\tilde{f} = \int_0^1 f\ \tilde{P}(f)\ df \tag{2.9}$$

$$g = \int_0^1 (f - \tilde{f})^2\ \tilde{P}(f)\ df \tag{2.10}$$

Both $\tilde{f}$ and g are known from the solution of the equations. Therefore, Equations (2.9) and (2.10) provide two implicit equations to solve for the most probable value μ and standard deviation σ of $\tilde{P}(f)$. This completes the specification of the probability density function. Mass and time-averaged values of the density, temperature

and composition can then be obtained from Equations (2.4) and (2.7), respectively, where $\phi(f)$ is specified by the equation of state.

2.2.3 Computations

Initial conditions for the calculations are prescribed at the injector exit similar to past work [15-17]. In the absence of other information, all properties are assumed to be constant at the injector exit, aside from a shear layer having a thickness equal to 1% of the injector radius at the passage wall. The constant property portion of the flow is specified as follows:

$$x = 0, \ r < 0.99d/2; \ \tilde{u}_o = \dot{M}_o/\dot{m}_o, \ \tilde{f}_o = 1, \ k_o = (0.02\tilde{u}_o)^2,$$

$$\varepsilon_o = 2.84 \times 10^{-5} \ \tilde{u}_o^{\ 3}/d \ , \ g_o = 0 \tag{2.11}$$

The initial variation of $\tilde{u}$ and $\tilde{f}$ in the shear layer was assumed to be linear. Equation (2.11) provides the inner boundary condition until the shear layer reaches the spray axis after which all gradients at the axis are zero. In the shear layer, initial values of k and ε were found by solving their transport equations while neglecting convection and diffusion terms; while g was assumed to be proportional to the local kinetic energy, k. The ambient values of $\tilde{u}$, $\tilde{f}$, k, ε and g are all zero for the flows considered here.

The calculations were performed using a modified version of GENMIX [26]. The computational grid was similar to past work [15-17]: 33 cross-stream grid nodes; streamwise step sizes limited to 6% of the current flow width or an entrainment increase of 5%--whichever was smaller.

2.3 Deterministic Separated Flow Model

2.3.1 Discrete Phase

The deterministic separated flow model adopts the main features of the LHF model, but only for the gas phase. The liquid phase is treated by solving the Lagrangian equations of motion of the drops and then computing the source terms in the governing equations for the gas phase, resulting from interphase transport processes. This general procedure corresponds to the particle tracking or particle-source-in-cell methods used in most recent two-phase models and is often called a discrete droplet model (DDM) [1,2].

The main assumptions related to momentum coupling between the two phases, of the drop trajectory calculations, are as follows: dilute spray with a drag coefficient equivalent to a single solid sphere in an infinite environment; ambient conditions given by mean-flow properties; quasisteady gas phase; negligible drop shattering; and negligible collisions.

Drops leaving the injector are divided into n groups, defined by the initial position, size, velocity and direction. The subsequent motion of each group is given by

$$\vec{x}_{pi} = \vec{x}_{poi} + \int_o^t \tilde{u}_{pi} \, dt \quad , \quad i = 1,2,3 \tag{2.12}$$

The mean drop velocity is determined by integrating the equation for conservation of momentum

$$m \frac{d\tilde{u}_{pi}}{dt} = - (\pi/8) \, d_p^2 \, \bar{\rho} \, C_D \left| \vec{\tilde{u}}_p - \vec{\tilde{u}} \right| (\tilde{u}_{p_i} - \tilde{u}_i) + a_i \quad , \quad i = 1,2,3 \tag{2.13}$$

The standard drag coefficient ¡for solid spheres is employed in the calculations, approximated as follows [1]:

$$C_D = \frac{24}{Re} \left(1 + \frac{Re^{2/3}}{6} \right) \quad , \quad Re < 1000$$

$$= 0.44 \qquad \qquad , \quad Re > 1000 \tag{2.14}$$

$$\text{where,} \quad Re = \frac{d_p \left| \vec{\tilde{u}}_p - \vec{\tilde{u}} \right|}{\nu} \tag{2.15}$$

The following additional assumptions, related to heat and mass transfer coupling between the two phases, are made for the drop trajectory and life history calculations: the radial velocity of the liquid surface due to evaporation of liquid is neglected; the solubility of ambient gases in the liquid is negligible; the vapor pressure of the liquid at the drop surface temperature is used to determine the vapor mass fraction at the liquid surface; effects of curvature (surface tension) on vapor pressure is ignored since it is generally found that this effect is small for pressures greater than 1 atm and drop diameters greater than 1 micron [1]; the gas-phase Lewis number is unity; Dufour and Soret effects are neglected; effects of forced convection are represented by empirical correlations; transport processes within the drop are represented by the limiting case of the thin skin model; and drop transport characteristics are computed from mean gas-phase properties in the vicinity of the drop neglecting effects due to turbulent fluctuations. The last assumption is characteristic of the DSF model and will be relaxed for the SSF model. All the above assumptions are common for dilute spray models and their justification is discussed by Faeth [1].

It is generally necessary to treat transient effects of drop heating throughout the lifetime of a drop, since transport processes within a drop have characteristic times which are comparable to drop lifetimes [1]. Exact analysis of internal drop transport processes is not feasible, therefore, two limiting cases have usually been examined by past investigators [1]. In the first case, or thin skin model for

the liquid-phase transport, heat and mass diffusivities in the liquid phase are assumed to be zero so that the bulk-liquid properties remain at the injected condition. However, an infinitely thin surface layer is assumed to be heated and has composition changes required by phase equilibrium. The second case, or uniform temperature model, involves the assumption of infinite thermal diffusivity. In this case, the drop temperature is spatially uniform, but time varying. Both models have been shown to predict quite similar evaporation rates (which is the most important variable of interest) for evaporating and combusting sprays at atmospheric pressure [1]. The thin skin model was chosen in the present study since it affords other major simplifications for the continuous-phase analysis, as will be seen later.

With the above assumptions, the following drop conservation equations are solved, in addition to Equations (2.12)-(2.15), for each drop group i:

$$\frac{d\ d_{pi}}{dx_{pi}} = -2\dot{m}_i''/(u_{pi}\ \rho_f) \tag{2.16}$$

$$h(\bar{T} - T_{Psi}) = \dot{m}_i''\ h_{fg} \tag{2.17}$$

where,

$$\frac{\dot{m}_i''\ d_{pi}}{\rho\ D} = 2\ N_S\ \ln\ (1 + B) \tag{2.18}$$

$$\frac{h\ d_{pi}}{k} = 2\ N_P\ \ln\ (1 + B)/B \tag{2.19}$$

$$B = (Y_{Fg_s} - Y_{Fg_\infty})/(1 - Y_{Fg_s}) \tag{2.20}$$

$$N_P\ \text{or}\ N_S = 1 + \frac{0.276\ Re^{1/2}\ (Pr\ \text{or}\ Sc)^{1/3}}{(1 + 1.232/(Re\ (Pr\ \text{or}\ Sc)^{4/3}))^{1/2}} \tag{2.21}$$

In Equation (2.19), h is a heat transfer coefficient that has been corrected for convection and mass transfer effects. Equation (2.21) is a multiplicative correction for heat and mass transfer with convection proposed by Faeth [1], and provides a reasonable correlation of existing data for Re < 2000.

In Equation (2.20), Y_{Fg_s} is determined, knowing the liquid surface temperature and the pressure, from the vapor pressure characteristic of the liquid

$$Y_{Fg_s} = f\ (T_{p_s}, p) \tag{2.22}$$

The particular vapor pressure relationship, along with other properties of Freon-11, and the mixing rules used in the present calculations are presented in Appendix A.

In Equation (2.13), the size and mass of the drop are related as follows:

$$m_i = (\pi/6) \; \rho_{bf} \; d_{pi}^3 \tag{2.23}$$

where ρ_{bf} is the bulk liquid density which remains constant at the injected condition under the assumptions of the thin skin model. All other properties in Equations (2.12)-(2.21) are either at the surface state or an average condition for the flow field around the drop. Average properties were computed at a mean state defined as follows:

$$\phi_{avg} = \alpha \; \phi_{g_s} + (1 - \alpha) \; \bar{\phi}_{g_\infty} \tag{2.24}$$

where ϕ is a generic quantity representing either mass fraction or temperature, and $0 \leq \alpha \leq 1$.

Uncertainties in proper average transport properties to be used in the drop trajectory calculations are a potential source of error. This error was minimized by calibrating the drop life history calculations with single drop experiments. A description of the calibration experiments and the results are described in Appendix C. Based on the present tests, a value of $\alpha = 0.75$ was used in Equation (2.24).

2.3.2 Continuous Phase

2.3.2.1 Description of Model

This portion of the analysis also utilizes the dilute spray approximation. This implies that the void fraction is unity and that the presence of drops does not contribute directly to the generation or dissipation of turbulence (the latter effect is frequently called turbulence modulation).

The interaction between the liquid and gas phases yields an additional source terms S_p on the RHS of Equation (2.1). For conservation of momentum, this term is found by computing the net change of momentum of each drop class i as it passes across a computational cell j.[2] The momentum source term per unit cell volume is as follows:

---

[2] Only one index is needed to define a cell since the calculation is parabolic and each computational cell is defined by its radial position.

Momentum: $S_{p\vec{u}_j} = \left(\sum_{i=1}^{n} \dot{n}_i \left((m_i \vec{u}_{pi})_{in} - (m_i \vec{u}_{po})_{out} \right)_j \right)/V_j$ (2.25)

where $\dot{n}_i$ is the number of drops per unit time in each class and in and out denote drop conditions entering and leaving the computational cell. This procedure allows for complete momentum coupling between the two phases.

The following assumptions are used to treat heat and mass transfer effects: the gas-phase Lewis number is unity; the mixing process in the gas-phase is adiabatic, and the transport processes in the liquid-phase is represented by the thin skin model. The last assumption precludes the need to solve the energy equation, since all the heat reaching the drops is used to gasify the liquid. Furthermore, the conserved scalar approach (for mixture fraction) is no longer used. Instead, the conservation equation for Freon-11 vapor mass fraction, $\tilde{Y}_{Fg}$, is solved. All other scalar properties of the gas-phase, e.g., temperature, density and composition, can then be determined, provided state relationships relating these scalar properties as a function of Freon-11 vapor mass fraction can be constructed. The state relationships used in the present study are described in the next section.

The conservation equation for $\tilde{Y}_{Fg}$ has a source term $S_{pY_{Fg}}$ on the RHS of Equation (3.1). This term is found by computing the net change of mass of each drop group i as it passes across a computational cell j, and is given as follows:

$$S_{pY_{Fg_j}} = \left[\sum_{i=1}^{n} \dot{n}_i \left((m_i)_{in} - (m_i)_{out} \right)_j \right]/V_j \qquad (2.26)$$

The conservation equation for mass also has a source term S_{pm} on the RHS of Equation (2.1), which is identical to Equation (2.26). Inclusion of this source term requires a fundamental restructuring of the GENMIX computational code, since the governing equations are solved in the dimensionless stream function domain [26]. For dilute sprays considered in the present study, this distributed source term S_{pm} has a negligible contribution to the total mass flow rate at any cross-section of the flow, since entrainment rates are much higher. For instance, it was found that the contribution of S_{pm} to the total mass flow rate of the continuous phase between x/d = 50 and 250 was approximately 1.5-3% of the entrained flow in the case 1 and case 2 evaporating sprays, respectively. Therefore, S_{pm} was not included in the conservation equation for mass, since the relatively significant effort required for program modification was not warranted in the present study.
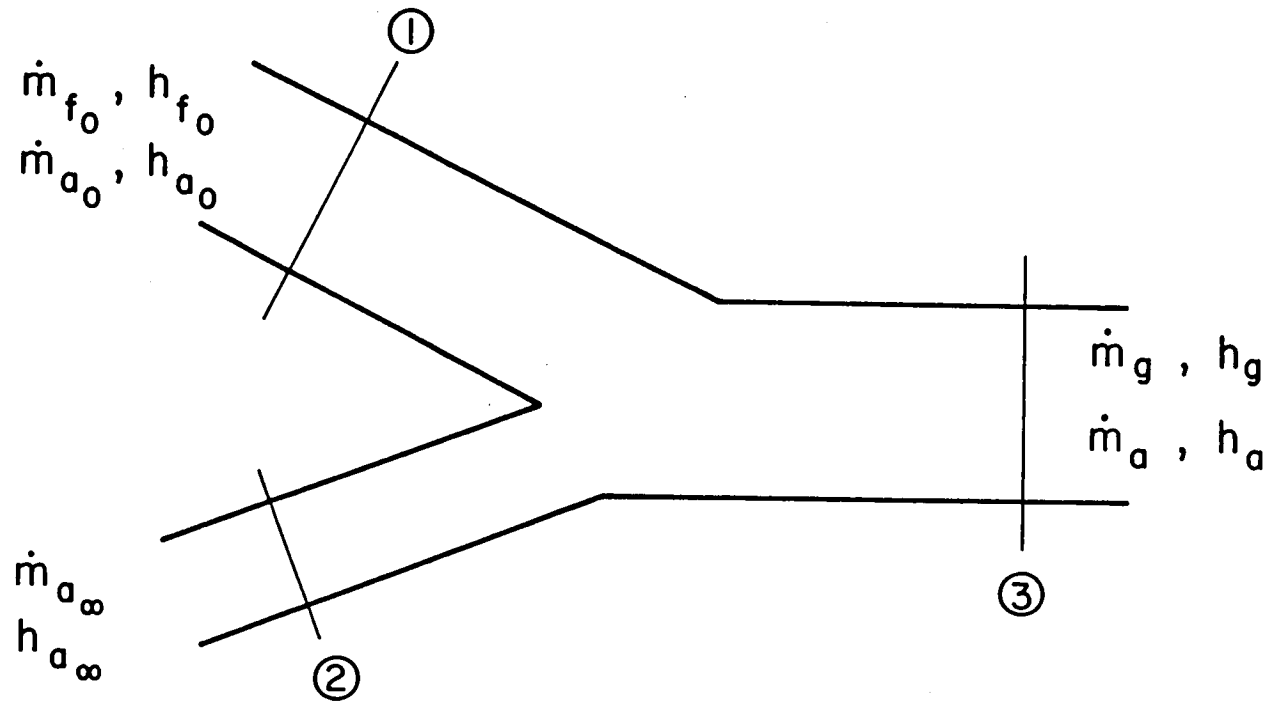
Figure 1. Schematic representation of the mixing process.

14

Finally, the conservation equation for Freon-11 vapor mass fraction fluctuations, g_{Fg} equivalent to the g-equation in Equation (2.1), is solved as required by the second-order turbulence model. The remainder of the continuous-phase analysis is similar to the LHF model except for the state relationships and the probability density function model, which is described in the following sections.

2.3.2.2 State Relationships

For the separated flow models, the variations of of enthalpy, composition, temperature and density of the gaseous mixture with Freon-11 vapor mass fraction are provided by the state relationships. All gases are assumed to be ideal gases, since the experimental results were all obtained at relatively low pressures. Combustion is not treated, therefore, chemical reaction is ignored. Furthermore, under the assumptions of the present analysis, the mixing process is adiabatic and occurs at constant pressure.

With the above assumptions, the adiabatic mixing process at any point in the flow can be shown schematically as in Figure 1. Stream 1 originates from upstream of the injector exit, and consists of Freon-11 liquid and air since an air-atomizing injector was used. Stream 2 represents ambient air, which does not contain any Freon-11. Conservation of species yields

$$\dot{m}_g = \dot{m}_{fo} \tag{2.27}$$

$$\dot{m}_a = \dot{m}_{ao} + \dot{m}_{a\infty} \tag{2.28}$$

Conservation of energy yields

$$\dot{m}_{fo} h_{fo} + \dot{m}_{ao} h_{ao} + \dot{m}_{a\infty} h_{a\infty} = \dot{m}_g h_g + \dot{m}_a h_a \tag{2.29}$$

It is assumed that the ambient air and injector air are at the same state, which closely approximates experimental conditions; therefore,

$$h_{a_o} = h_{a_\infty} \tag{2.30}$$

Using the ideal gas assumption, and combining Equations (2.27)-(2.30), we have, in terms of gas-phase mass fractions,

$$Y_{Fg} (h_{fgo} + C_{Pg} (T_o - T)) + Y_a C_{pa} (T_o - T) = 0 \tag{2.31}$$

where,

$$Y_a = 1 - Y_{Fg} \tag{2.32}$$

Therefore, the properties at each point in the flow correspond to the thermodynamic state reached when an amount Y_{Fg} of injected Freon-11 at its initial state and $(1 - Y_{Fg})$ of air at ambient conditions, are adiabatically mixed at the ambient pressure of the jet. Given the Freon-11 vapor mass fraction, the composition and temperature of the

gaseous mixture is obtained from Equations (2.31) and (2.32). The mixture specific volume is obtained from

$$v = \left[Y_{Fg}/\rho_g + Y_a/\rho_a \right]$$ (2.33)

where the air and vapor densities are obtained from the ideal gas expression at the temperature and total pressure of the mixture.

At a Freon-11 vapor mass fraction of $Y_{Fg} = 0.292$, the Freon-11 vapor-air mixture becomes completely saturated. For present conditions, the saturation temperature at this state is 240.3 K. Any further increase in the Freon-11 vapor mass fraction Y_{Fg} is assumed to result in the condensation of the excess vapor which then remains suspended as foglike droplets in the gas-phase. The total mixture is very likely to follow the locally homogeneous approximation, so that the temperature of the mixture is assumed to remain constant at the saturation value. At such conditions, however, the specific volume of the gaseous mixture is recalculated to account for the condensed portion of the Freon-11 vapor, as follows:

$$v = \left[(Y_{Fg} - 0.292)/\rho_f + 0.292/\rho_g + Y_a/\rho_a \right]$$ (2.34)

In Equation (2.34), the densities are evaluated at the saturation temperature, 240.3 K. Figure 2 shows the state relationship obtained from the analysis described above. The properties of the spray fluids used to construct the state relationship are presented in Appendix A.

2.3.2.3 Probability Density Function Model

The mean value of any scalar quantity ϕ (other than k, ε and g_{Fg}) can be determined from its variation with Y_{Fg} if the probability density function of Y_{Fg}, $\tilde{P}(Y_{Fg})$, is known as a function of position in the flow. Given $\tilde{P}(Y_{Fg})$, the mass-averaged means and variances of any scalar ϕ is given by Equations (2.4) and (2.5), respectively, with f replaced by Y_{Fg}. As before, a clipped Gaussian function was assumed for $\tilde{P}(Y_{Fg})$. $\tilde{P}(Y_{Fg})$ is characterized by the most probable value μ, and the standard deviation σ of the distribution which can be found from the local values of $\tilde{Y}_{Fg}$ and g_{Fg} as follows:

$$\tilde{Y}_{Fg} = \int_0^1 Y_{Fg} \, \tilde{P}(Y_{Fg}) \, dY_{Fg}$$ (2.35)

$$g_{Fg} = \int_0^1 (Y_{Fg} - \tilde{Y}_{Fg})^2 \, \tilde{P}(Y_{Fg}) \, dY_{Fg}$$ (2.36)

Both $\tilde{Y}_{Fg}$ and g_{Fg} are known from the solution of their respective conservation equations. Therefore, Equations (2.35) and (2.36) provide two implicit equations to solve for μ and σ. This completes the specification of the probability density function.
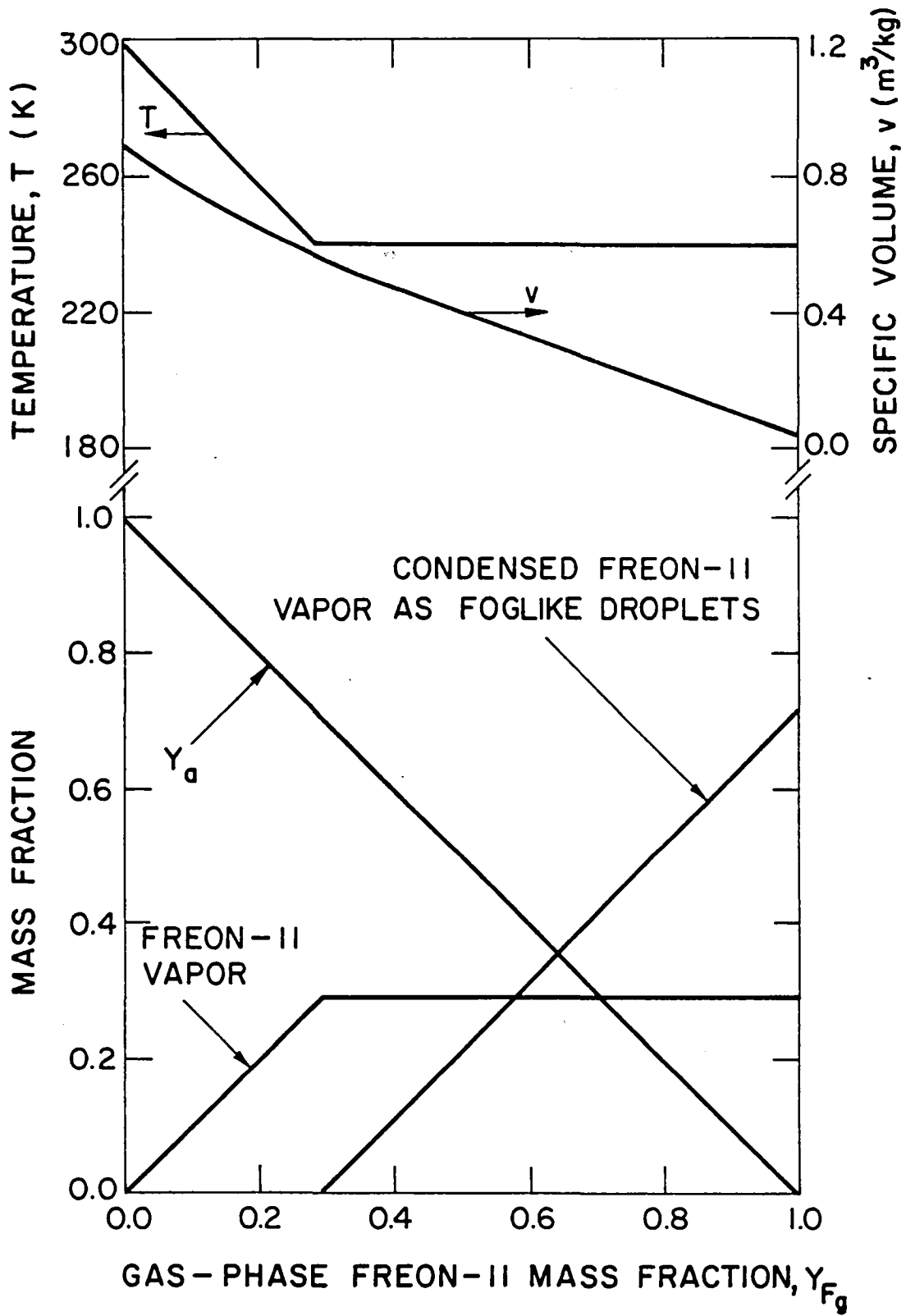
Figure 2. State relationship for the Freon-11
vapor-air mixture (SF Model).

Time-averaged scalar properties of the continuous phase are needed in the drop trajectory and life history computations, Equations (2.13)-(2.21). These were found, as before, from Equations (2.6)-(2.8), with f replaced by Y_{Fg}.

Time-averaged velocity of the continuous phase surrounding the drops is also needed in the discrete phase computations. However, to obtain the time-averaged velocity from the Favre-averaged velocity, the correlation involving fluctuating density and fluctuating velocity must be known, since

$$\tilde{u} = \bar{u} + \frac{\overline{\rho'u'}}{\bar{\rho}} \qquad (2.37)$$

In the present study, this correlation was assumed to be zero, so that the Favre- and time-averaged velocities are equal.

The gas-phase equations are solved in the same manner as the LHF model. The only change in this portion of he program involves addition of the new source terms given in Equations (2.25) and (2.26). The drop motion equations, Equations (2.12)-(2.21), are solved at the same time, in a stepwise fashion, using a second-order finite difference algorithm.

Computations with the separated flow models were initiated at x/d = 50 for all the test sprays, which was the position nearest the injector where adequate spatial resolution was obtained so that profile measurements could provide initial conditions for the calculations. These initial conditions included measurements of mean and fluctuating gas-phase properties, liquid flux, drop size and axial components of the mean and fluctuating drop velocities for both evaporating sprays. Initial conditions for ε were computed using Equation (2.3) and the measured values of $\bar{u}$, k and the Reynolds stress.

Downstream of x/d = 50 the void fraction was always greater than 99.1%; therefore, the dilute spray approximation was justified with little error. The computations for the DSF model employed no less than 1800 drop groups.

2.4 Stochastic Separated Flow Model

The DSF model considers only deterministic trajectories for drop groups. The stochastic separated flow model, however, includes effects of turbulent fluctuations on drop dispersion and interphase momentum transport rates by using a technique proposed by Gosman and Ioannides [22].

The stochastic model involves computing the trajectories of a statistically significant sample of individual drops as they move away from the injector and encounter a random distribution of turbulent eddies—utilizing Monte Carlo methods. The key elements of this approach are the methods for specifying the properties of each eddy and the time of interaction of a drop with a particular eddy.

Properties within a particular eddy are assumed to be uniform, but properties change in a random fashion from eddy to eddy. The trajectory calculation is the same as the DSF model, involving solution of Equations (2.12)-(2.21); however, mean-gas properties in these equations are replaced by the instantaneous properties of each eddy.

The properties of each eddy were found at the start of drop.eddy interaction by making a random selection from the probability density function (PDF) of velocity. Velocity fluctuations were assumed to be isotropic with a Gaussian PDF having a standard deviation of $(2k/3)^{1/2}$ and mean components $\bar{u}$, $\bar{v}$, 0. This ignores the distinction between Favre- and time-averaged velocities (the latter being the quantity that should be sampled), since, as mentioned earlier, the correlation involving fluctuating density and fluctuating velocity was assumed to be zero. The cumulative distribution function for each velocity component was constructed and sampled. This involved randomly selecting three numbers in the range 0-1 and computing the velocity components for these three values of the cumulative distribution function.

The instantaneous scalar properties of each eddy were found in a similar manner. Scalar properties of the continuous phase are only a function of Freon-11 vapor mass fraction Y_{Fg}. The instantaneous scalar properties of each eddy are also only a function of the instantaneous value of Y_{Fg}. At any point in the flow, the Favre clipped Gaussian distribution function of Y_{Fg} was constructed knowing the values of $\tilde{Y}_{Fg}$ and g_{Fg}. This Favre PDF can be used to calculate the conventional time-averaged probability density function, $P(Y_{Fg})$, as follows [25]:

$$\rho(Y_{Fg}) \, P(Y_{Fg}) = \bar{\rho} \, \tilde{P}(Y_{Fg}) \tag{2.38}$$

The cumulative distribution function for Y_{Fg} can be constructed from the time-averaged PDF. This distribution was randomly sampled by selecting a random number in the range 0-1 to find the instantaneous value of Y_{Fg}. The instantaneous temperature, composition and density of the eddy was found by using the instantaneous value of Y_{Fg} in conjunction with the state relationships, Figure 2.

A drop was assumed to interact with an eddy for a time which was decided from either the eddy lifetime or the characteristic size of an eddy [1-5]. The characteristic size of an eddy was taken to be the dissipation length scale.

$$L_e = C_\mu^{3/4} \, K^{3/2}/\varepsilon \tag{2.39}$$

The eddy lifetime was computed from the following:

$$t_e = L_e/(2k/3)^{1/2} \tag{2.40}$$

Drops were assumed to interact with an eddy as long as the time of interaction, Δt, and the distance of interaction $|\Delta \vec{x}_p|$, satisfied the following criteria:

$$\Delta t \leq t_e \quad , \quad \left| \Delta \vec{x}_p \right| \leq L_e \tag{2.41}$$

Drop capture by an eddy corresponds to ending the interaction with the first criterion while a drop traverses an eddy when the interaction is ended with the second criterion.

The remaining computations are similar to the DSF model, except that the source terms of Equations (2.16) and (2.26) are computed for the random-walk trajectories of the drops—as opposed to the deterministic solution. Also, more drop trajectories must be considered to obtain statistically significant drop properties (generally 5000-6000 trajectories were used). A by-product of the additional calculations, however, is that the SSF model yields both mean and fluctuating drop properties. This provides an additional test of model performance.

3. EXPERIMENTAL METHODS

3.1 Introduction

The experimental apparatus provided convenient optical and probe access to the flow. The injector and the fluid delivery system allowed selection of fine and coarse sprays and assured long-term repeatability of the test spray conditions.

The following flows were examined during the present study:

1. An isothermal air jet—to check experimental techniques.

2. Two evaporating sprays (with Sauter mean diameters of 30 and 58 μm).

Nonintrusive instrumentation included the laser-Doppler anemometer and multiflash photography. Other measurements involved probes such as isokinetic sampling probes, shielded thermocouples and slide impactors.

3.2 Test Apparatus

The requirement for a flow configuration having no zones of recirculation, a simple geometry and well-defined boundary conditions is met with the apparatus illustrated in Figure 3. The injector was mounted on a two-dimensional traversing mechanism at the center of a cage assembly (1 m square by 2.5 m high). For all the test flows, injection was vertically downward into stagnant room air. The flow was protected from room disturbances using 16-mesh screens all around the cage. Major traversing, to obtain radial profiles of flow quantities, involved moving the entire cage assembly, which was mounted on a bearing track. This approach keeps the flow nearly concentric with the vertical axis of the cage, which minimizes disturbance of the axisymmetric flow due to off-center screen positions, and also allows
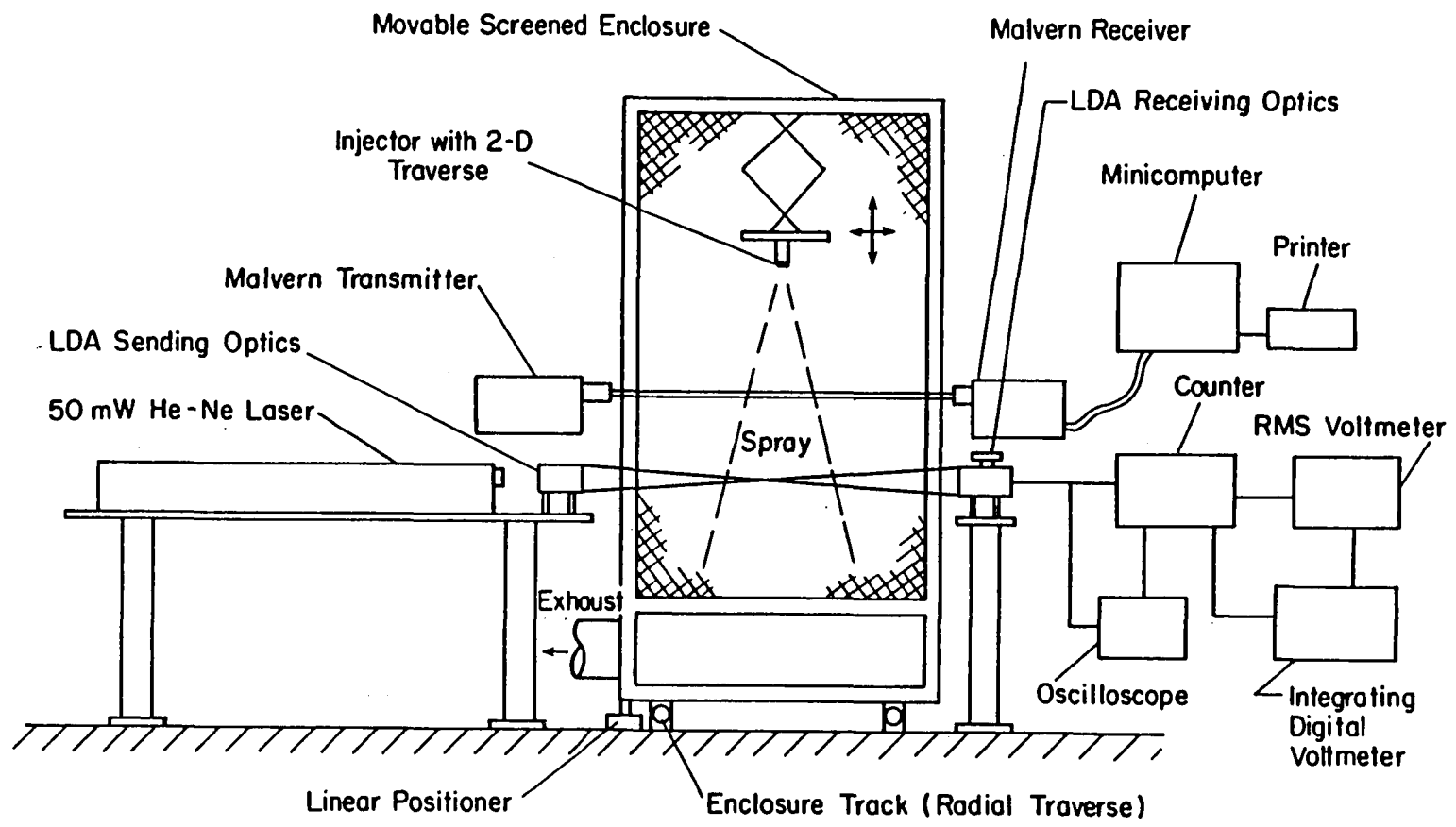
Figure 3. Sketch of the experimental apparatus.

optical instrumentation to be mounted on a rigid base. Unislide arrangements were used to position the injector relative to the measurement location.

A plenum chamber with an exhaust system was included at the bottom of the cage. The inlet to the plenum chamber is screened and is 1 m below the plane of instrumentation. The screened inlet provides uniform suction thus keeping the flow axisymmetric. The only purpose of the exhaust system was to prevent the smallest drops from recirculating and its operation did not introduce a coflow of any significance. Testing showed that the disturbance levels were less than 1% at the measurement location.

Measurements from this arrangement should be attractive for those wishing to evaluate models. The flow is analogous to a jet in stagnant surroundings, yielding a parabolic (boundary layer) flow. The turbulence characteristics of such a flow can be modeled more reliably than flows with recirculation. Naturally, boundary layer flows greatly simplify problems of obtaining accurate numerical solutions, releasing computer time for use in the two-phase portion of the problem. The absence of coflow eliminates problems of flow separation on bulky injector elements. Boundary conditions are well-defined, since there are no uncertainties regarding wall friction and heat losses and inlet flow properties which are encountered in enclosed chambers.

The flow system of the injector is illustrated in Figure 4. A Spraying Systems Company air atomizing injector (model 1/4 J2050 fluid nozzle and 67147 air nozzle with outlet diameter of 1.194 mm) was used for all the spray tests. The injector delivers a full-cone spray with no swirl. This injector is identical to that used by Faeth and coworkers [15-17].

The air flow to the injector is controlled with a pressure regulator and metered with a critical flow orifice to ensure long-term stable operation. The pressure regulator was a Matheson model 4 regulator with a 0-21 MPa output capacity. The pressure upstream of the critical-flow orifice was measured with a Heise absolute pressure gauge with a 0-2.1 MPa capacity. The pressure gauge was calibrated with a dead-weight tester and the orifice was calibrated with a Precision Scientific Company wet-test meter (0.283 liters/rev.).

The liquid was stored in a tank under pressure. Since the tank was not agitated and pressure levels were moderate (0.3-0.8 MPa), the dissolved air content of the spray liquids was negligible. The liquid flow is controlled with a valve and metered with rotameters. A Matheson model 604 rotameter, used to meter the evaporating spray liquid, was calibrated with a sight-gauge apparatus.

The spray liquid must be well-defined material in order to facilitate use of the measurements by others. Freon 11 supplied by Pennwalt Corporation was used for tests with the evaporating sprays. The properties of Freon 11 are summarized in Appendix A. In order to maintain repeatable flow and atomization conditions the entire test cell was heated to above-normal temperatures--to 27 ± 1°C.

CRITICAL FLOW ORIFICE

20 MPa AIR SUPPLY

SPRAY

INJECTOR

VENT

LIQUID SUPPLY TANK

ROTAMETER

LIQUID PRESSURE FEED TANK
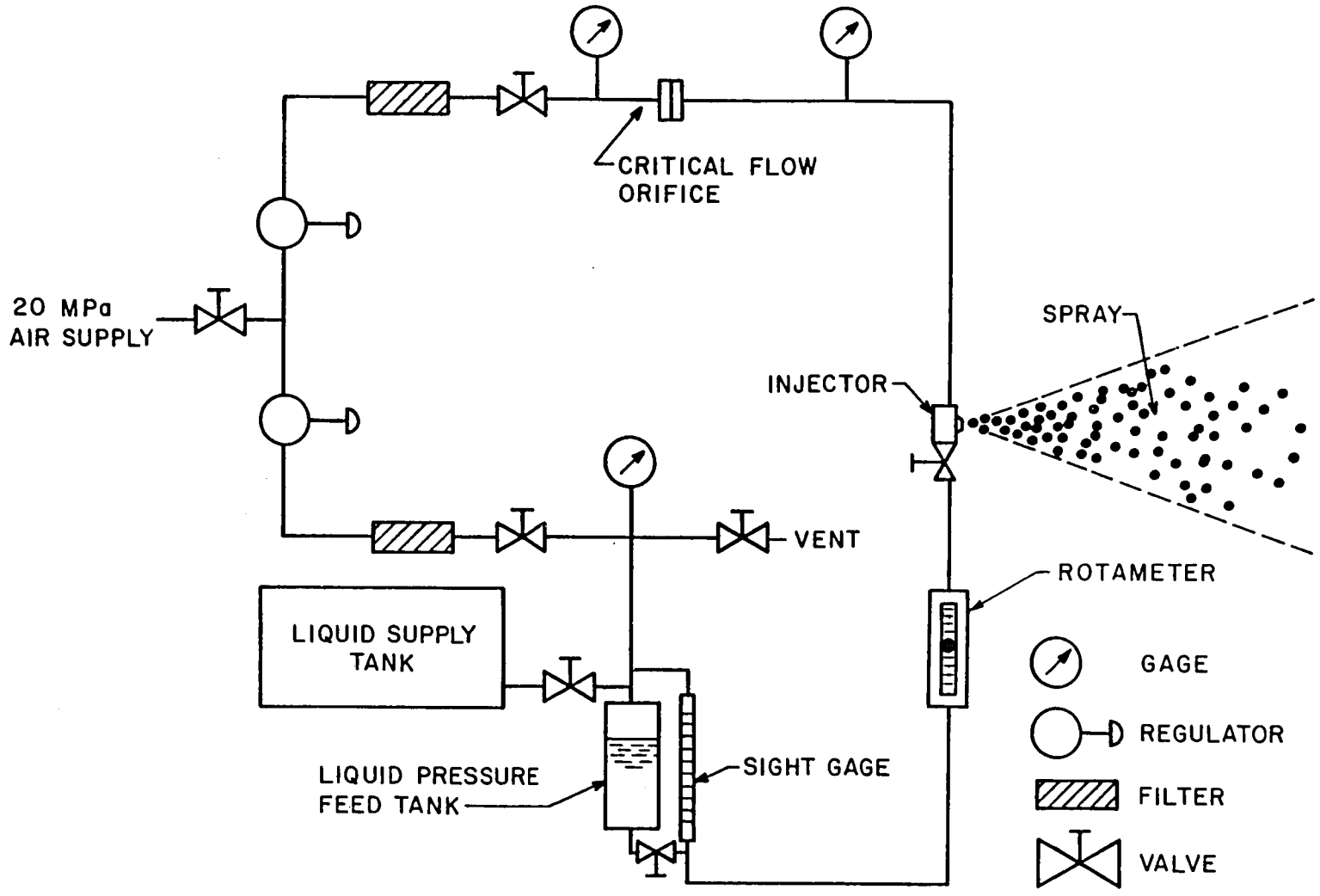
SIGHT GAGE

GAGE

REGULATOR

FILTER

VALVE

Figure 4. Sketch of the injector flow system.

3.3 Measurement Techniques and Instrumentation

3.3.1 Gas-Phase Properties

3.3.1.1 Velocity Measurement

Table 2 is a summary of the flow structure measurements made and the techniques employed for each measurement.

Mean and fluctuating gas velocities were measured using a dual-beam, single-channel, frequency-shifted laser-Doppler anemometer (LDA). An equipment list for the LDA system appears in Table 3. The sending and receiving optics had a focal length of 242 mm with a 11.61° angle between beams. A 200 mm focal length lens was used to focus the scattered light onto a photomultiplier. The aperture diameter of the photomultiplier was 0.25 mm. The receiving lens was masked with a beam-stop which provided a collection aperture having a diameter of 25 mm. The above optical configuration produced a measuring volume 0.470 mm in length and 0.098 mm in diameter, with a fringe spacing of 3.128 μm.

Seeding particles for operation of the LDA were provided in two ways. In the two-phase region, the smallest drops provided adequate seeding, while erroneous signals from large drops were eliminated by setting a low signal amplitude limit on the counter data processor, since large drops yield large pedestal signals. This natural source was supplemented by seeding the surroundings of the spray using oil particles which are present suspended in the exhaust of a vacuum pump. The average diameter of the particles was 0.6 μm at a concentration of 2.8 x 10^{10} particles/m^3. Photographic measurements showed that the maximum concentration of spray drops was about 3.0 x 10^9 drops/m^3 at x/d = 40 in the 30 μm SMD evaporating spray. The concentration of spray drops was over two orders of magnitude less than the concentration of the seeding particles in other downstream positions of the test sprays. Therefore, gas velocities were primarily measured, with a small bias due to spray drops. The seeding techniques provided a relatively high signal rate so that concentration biasing was eliminated by using time averages. This procedure involved adjusting external seeding until intermittency was no longer observed on the oscilloscope trace of the LDA detector output.

Mean and fluctuating velocity components of the gas phase were measured at various axial and radial locations in all the four test sprays. An integration period of one minute or more was used to determine the mean quantities. Radial profiles were obtained in a single traverse across the spray and components of mean and fluctuating velocities were recorded by employing different beam orientations at each radial location. Measurements of the tangential component of the fluctuating velocity $(\overline{w'^2})^{1/2}$ were made with a separate traverse in the third direction. The use of several beam orientations allowed measurement of Reynolds stress. Reynolds stress measurements are valuable for checking model predictions and for locating the flow centerline (since Reynolds stress is zero at the centerline and doesn't

Table 2. Summary of Instrumentation for Spray Structure Measurements

Measurement	Technique	Equipment
Mean and fluctuating gas velocities.	Dual-beam, forward scatter laser-Doppler anemometer, frequency shifted with tracker and burst counter data processing.	Spectra Physics Model 125A (50 mW) He Ne laser, rest TSI, Inc.
Drop size and velocity.	Double-flash shadow photography.	In-house design.
Drop size distributions.	a)Slide impaction. b)Photography.	In-house design. In-house design.
Liquid flux.	Slide impaction.	In-house design.
Mean gas-phase temperature.	Fine-wire thermocouple shielded from drop impacts.	In-House design, 25 μm diameter wires.
Mean composition of major species.	Isokinetic sampling and analysis with gas chromatograph.	Varian model 920 gas chromatograph with hot-wire detector.

Table 3. LDA Equipment List

Component	Manufacturer	Model
Helium-Neon Laser	Spectra Physics	125A
Integrated Optics	Thermo-Systems	900
Frequency Shifter	Thermo-Systems	9180
Photodetector	Thermo-Systems	960
Frequency Tracker	Thermo-Systems	1090
Burst Counter	Thermo-Systems	1980
RMS Voltmeter	Thermo-Systems	1060
Dual-Beam Oscilloscope	Thermo-Systems	561A
Integrating Digital Voltmeter	Hewlett-Packard	240IC

exhibit the broad maxima encountered for other variables). The above measurements were found to be repeatable within 5%.

3.3.1.2 Temperature Measurement

Mean-gas temperatures in the evaporating spray were measured using a fine-wire thermocouple. It is difficult to obtain accurate mean temperature measurements in sprays due to effects of drop impaction. For this reason a shielded temperature probe which circumvented most of the difficulties was used [16]. A sketch of the thermocouple probe is shown in Figure 5. A 25 μm diameter chromel-alumel butt-welded thermocouple was located along the centerline of a 1.6 mm OD hemispherical shield. The shield was positioned upstream of the probe so that all but the smallest drops (diameter less than 10 μm generally) impinged on it.

The thermocouple was spot welded onto 0.75 mm diameter lead wires of the same material. The reference junction was placed in a reference cell, manufactured by Thermo-Electric Company, maintained at 0°C. A Hewlett-Packard integrating digital voltmeter, model 240 IC, was used to integrate the signal over one minute periods to determine the mean temperature. The measurements were repeatable to within 15%.

Temperature measurements in the evaporating spray were restricted to distances greater than x/d = 250 and x/d = 500 in the case 1 (30 μm SMD) and case 2 (58 μm SMD) evaporating sprays, respectively. Measurement at closer distances were unobtainable due to the formation of ice on the thermocouple shield.

3.3.2 Liquid-Phase Properties

3.3.2.1 Drop Size Measurement

Two methods were used to determine the drop size distributions and Sauter mean diameters (SMD) at various locations in the test sprays. The first method used for drop size measurements involved inertial impaction [15]. A sketch of the slide impactor is shown in Figure 6. Small glass slides coated with a layer of magnesium oxide are momentarily exposed to the flow using a pneumatically driven shutter. Drops leave a crater in the coating, which can be related to the initial drop size [15]. The slides are then viewed under a microscope and each drop impression is sized and counted. Typically, 2000 drops were counted at each measurement location to obtain statistically reliable results. The collection efficiency of the shutter mechanism was calculated for a range of droplet sizes for a given gas velocity [15]. This was then used to correct the number of droplets actually collected. The SMD at each location was calculated directly from the drop size distributions. A measurement of liquid mass-flux is also possible by the slide impaction method and will be described in a subsequent section.

The second method used to determine drop-size distributions involved an imaging technique, viz., double-flash photography, which was primarily used for simultaneous measurements of drop size and

16mm

THERMOCOUPLE WIRE
0.025 mm DIA.,
CHROMEL—ALUMEL

CERAMIC INSULATOR

HALF WIDTH, STAINLESS
STEEL HYPODERMIC NEEDLE
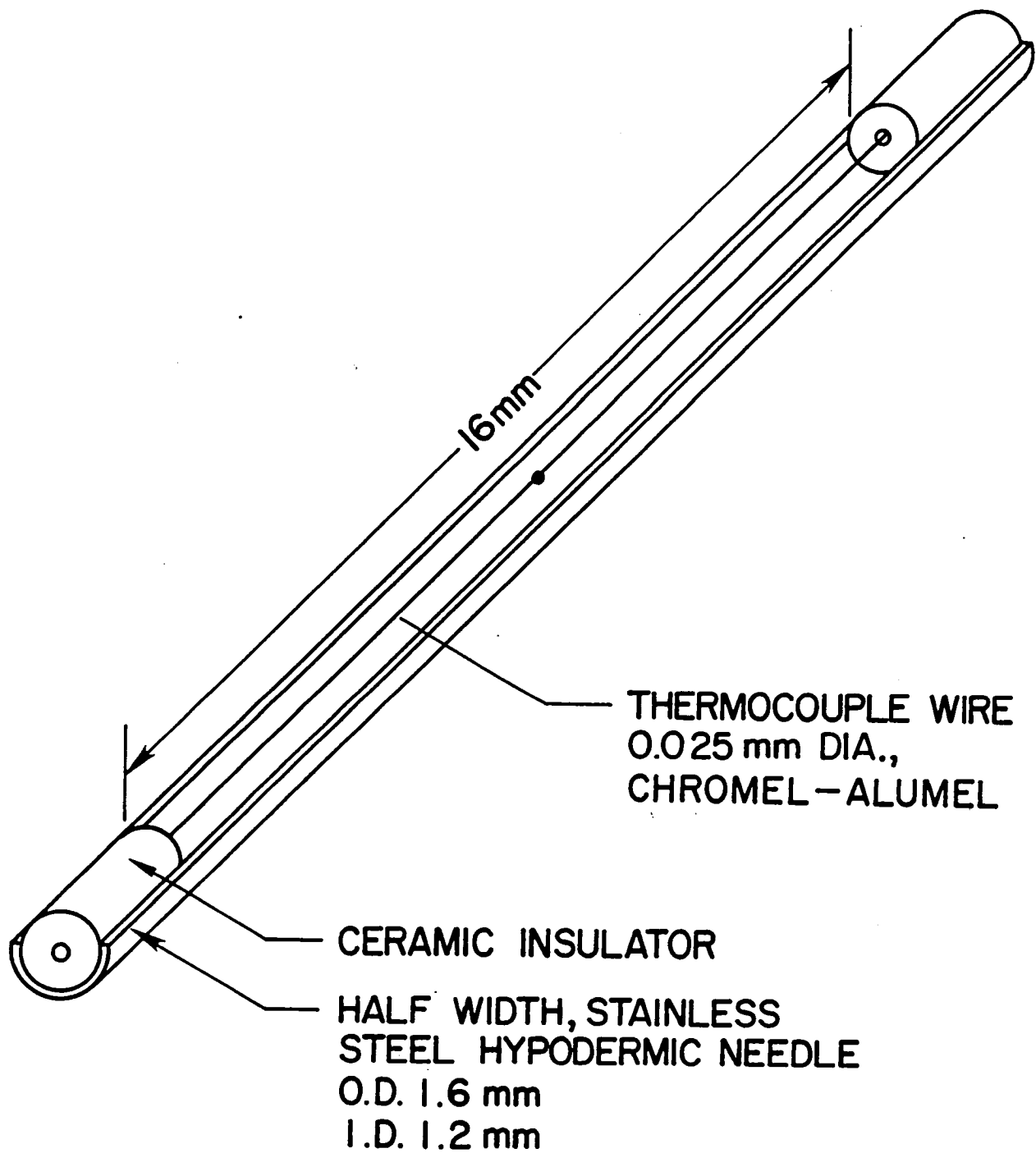O.D. 1.6 mm
I.D. 1.2 mm
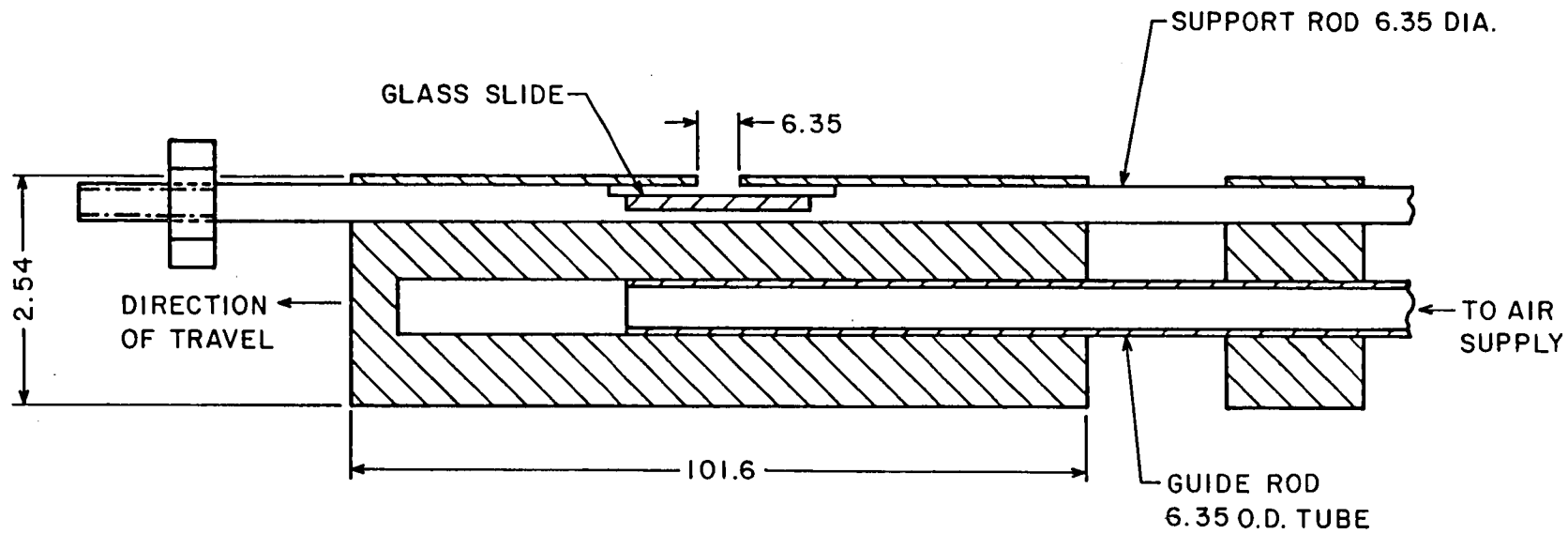
Figure 5.   Sketch of the thermocouple probe.

Figure 6.   Sketch of the droplet impactor.

velocity. A description of the imaging technique is given in the next section.

3.3.2.2 Drop Size and Velocity Correlation Measurement

The optical system used for the double-flash shadow photograph technique for drop size and velocity measurements is shown in Figure 7. The arrangement consists of two submicrosecond flash sources, a lens system to focus the light and a camera, all arranged on the same optical axis [27]. The flashes are fired consecutively, at electronically controlled times, so that two images of each of the moving droplets are obtained on the same photographic negative. Subsequent magnification of the negative, measurement of the size and distance traveled by the droplet, as well as knowledge of the time interval between the flashes yields the size and velocity of the droplets. A typical double-flash shadow photograph is shown in Figure 8.

A General Radio type 1538-A Strobotac and type 1539-A Stroboslave were used as the first and second flash sources, respectively, cf., Figure 7. They produced flashes having durations of 0.5 µs and 0.8 µs, respectively, and effectively stopped the motion of the droplets. The first flash was located at the focal point of lens 1 so that a parallel beam illuminated the field of view, yielding the sharpest shadow image. The second flash was arranged so that the light was focused onto the point of origin of the first flash. Since the second flash was of longer duration, it produced a darker image than the first--providing a means for identifying flow reversals.

The strobe units were triggered consecutively by means of a specially-designed pulse generator. The generator delivered pulses that met the input specifications of the strobe units and was also equipped with a variable time delay circuit so that the time interval between the pulses could be selected in the range 0.1-1000 µs. These pulses were recorded, as well, with a two-channel Nicolet Explorer III digital oscilloscope, model 204-A, so that the' time interval could be measured within 0.05 µs. Typical intervals used for the present test conditions ranged from 2-80 µs.

Various configurations of camera lenses, film and data reduction methods were used in different regions of the sprays. Obtaining initial conditions of drop size and velocity required good spatial resolution in relatively dense regions of the sprays. In these regions a Graphlex Optar, f/4.7, 135 mm focal length lens, in conjunction with a rectangular magnifier lens (27 mm x 40 mm, 60 mm focal length), was used as the imaging lens system. A Graphlex 4 x 5 still camera was located at the end of an extension tunnel to give a primary magnification of 38:1. The resulting rectangular area of the spray viewed (2.34 mm x 2.29 mm) provided satisfactory spatial resolution at x/d = 50. Polaroid type 57 film (3000 ASA) was used with this setup and measurements of drop diameter and interimage distances were made by further magnification under a calibrated microscope.
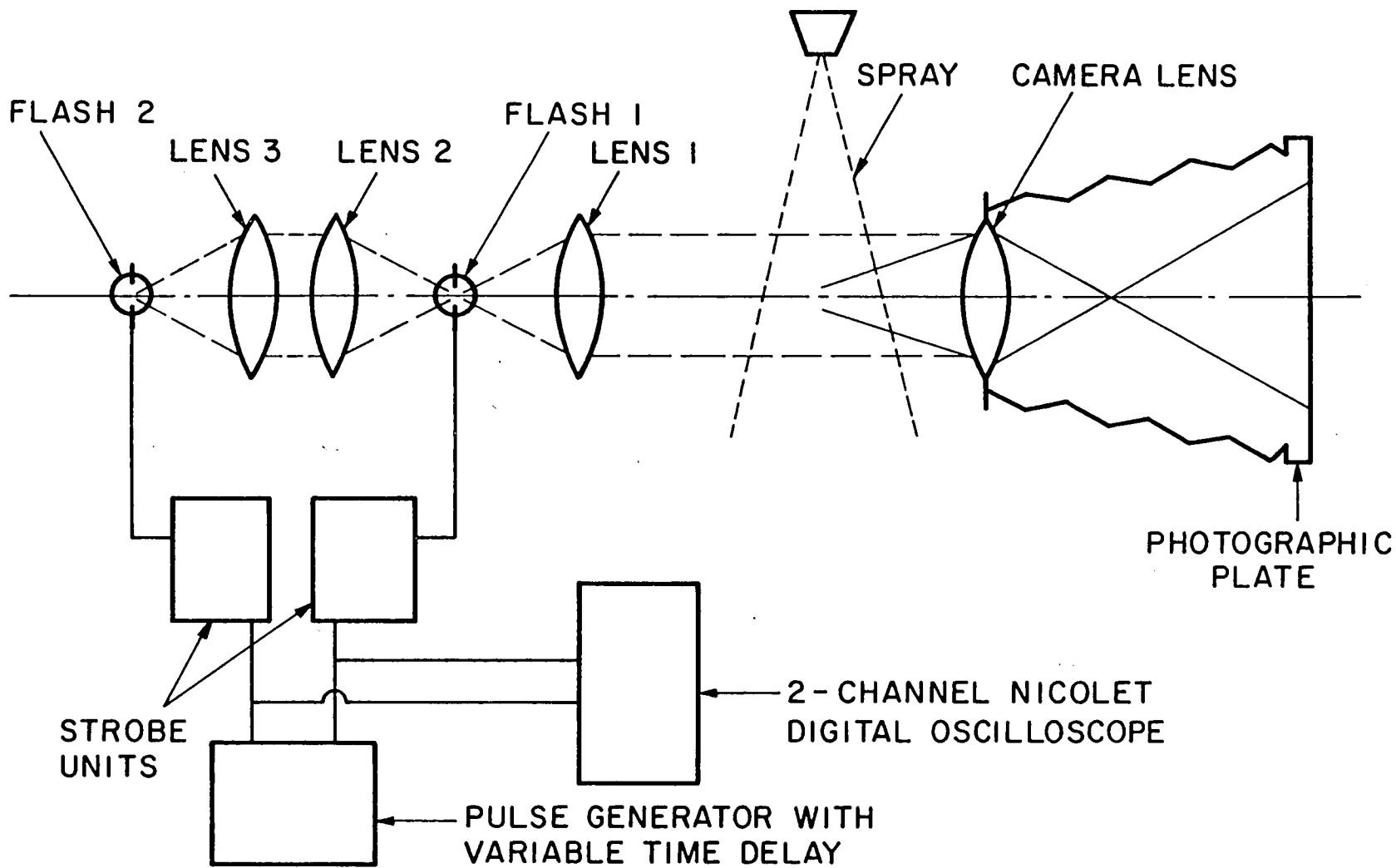
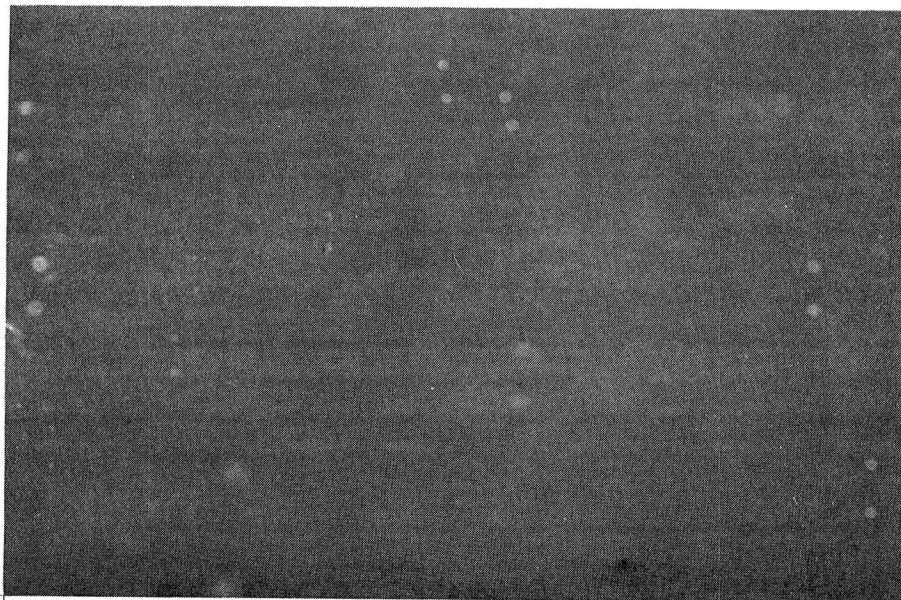Figure 7. Sketch of the double-flash photography system.

Figure 8. A typical double-flash photograph.

In the dilute regions of the sprays (x/d ≥ 100) the primary magnification was reduced to 6:1 and Agfa pan Vario-XL Professional 35 mm film (50-1600 ASA) was used. The negatives were projected on a screen at greatly increased magnifications to make measurements of size and distance between images. The spray area viewed with this arrangement was 5.7 mm x 8.0 mm.

The depth-of-field in which droplets appear to be in focus in the optical sampling volume increases with increasing drop size. This behavior results in an underestimation of the relative number of small drops. Depth-of-field bias corrections were applied to all photographic measurements of drop size distributions in the present study using a procedure similar to Reference [11]. Also, only the axial component of the drop velocities was recorded.

The overall accuracy of the present method for velocity measurements was estimated to be ± 10%. The uncertainty associated with size was on the order of ± 10% for drops having diameters greater than 25 µm. This uncertainty increased to ± 25% for drops whose diameters were smaller than 25 µm. The minimum drop size measurable within the above limits of error was 10 µm. Approximately 600 to 800 drops were counted at each measurement location to obtain drop size and velocity distributions, which were processed to find mean and fluctuating axial velocities and the SMD. Since the number frequency of the large drops (> 60 µm) at any given measurement location was relatively low, measurements of fluctuating velocities for the large drops are only qualitative. The SMD data obtained by this imaging method and the slide impaction method agreed within 15%.

3.3.2.3 Liquid Flux Measurement

Liquid flux measurements for the evaporating sprays employed slide impaction. As described earlier, the slide impaction method provides a measurement of drop size distributions. In addition, a measurement of liquid mass-flux was also obtained by measuring the time of exposure of the magnesium oxide coated glass slide and the area over which the drop impressions are sized and counted.

The slide impactor, shown in Figure 6, is equipped with a pneumatically driven shutter mechanism designed to expose the slide to the spray for a given time period. Perforations in the body of the shutter allow determination of the shutter speed by means of a laser beam-photodiode combination, the output of the photodiode being fed into a Nicolet digital oscilloscope. The liquid mass-flux was determined by dividing the total liquid mass (after correction of the number of droplets collected, as described previously) by the collection area and the exposure time. The overall uncertainty associated with the technique was estimated to be ± 20 percent for liquid mass-flux, based on measurements of this quantity in nonevaporating sprays [11].

3.3.3 Other Measurements

3.3.3.1 Concentration Measurement

The mean composition of injected fluid for the evaporating sprays was determined by isokinetic sampling and subsequent analysis with a gas chromatograph. The technique provided a direct measurement of the local mixture fraction of the flow.

A sketch of the sampling probe, which was similar to the one used by Shearer et al. [15], is shown in Figure 9. The tip of the sampling probe is heated to prevent moisture in the air from condensing and freezing at the probe inlet during the evaporating spray tests. Suction was applied to the sampling probe by a vacuum pump. The suction flow rate was measured by a Precision Scientific wet-test meter and the flow rate was adjusted to match the local gas velocity determined earlier from the velocity measurements.

The samples were analyzed by a Varian, model 920, gas chromatograph using a hot-wire detector. A 5 ml gas-tight syringe was used to transfer the sample from the sampling port to the gas chromatograph. The separating column was stainless steel, 3.175 mm OD by 183 cm in length packed with PORAPAK Q (80-100 mesh). The oven and detector temperatures of the gas chromatograph were maintained at 160°C and 200°C, respectively. Helium was used as the carrier gas at a flow rate of 20.0 cc/min. Various mixtures of 99.9% purity Freon-11 (purchased from Matheson Gas Products) and air were used to calibrate the chromatograph. The calibration procedure indicated that the peaks were symmetrical and that the concentration was a linear function of peak height for the concentration range of interest.

The mean injected-fluid concentration data was integrated over the cross-section of the sprays at far downstream locations (e.g., x/d = x/d = 250 and 500 for the case 1 spray and x/d = 500 for the case 2 spray), by assuming locally homogeneous conditions. This was checked against injector liquid mass flow rates to determine the collection efficiency of the technique.

3.3.3.2 Jet Momentum Measurement

The momentum of each of the test sprays was determined by measuring the axial force on an impingement plate held near the exit of the nozzle (95 mm diameter plate, 25 mm from the nozzle). A Unimeasure 80 force transducer was used to measure the force. The transducer was calibrated by placing known weights on the plate. The exit velocity of the two-phase spray was then calculated from the jet momentum and the mass flow rate. This calculation assumes locally homogeneous flow, and serves as initial conditions for the LHF spray model.

3.4 Experimental Conditions

Table 4 shows the experimental conditions for the case 1 and case 2 evaporating sprays. Case 1 is a finer spray than case 2.

34
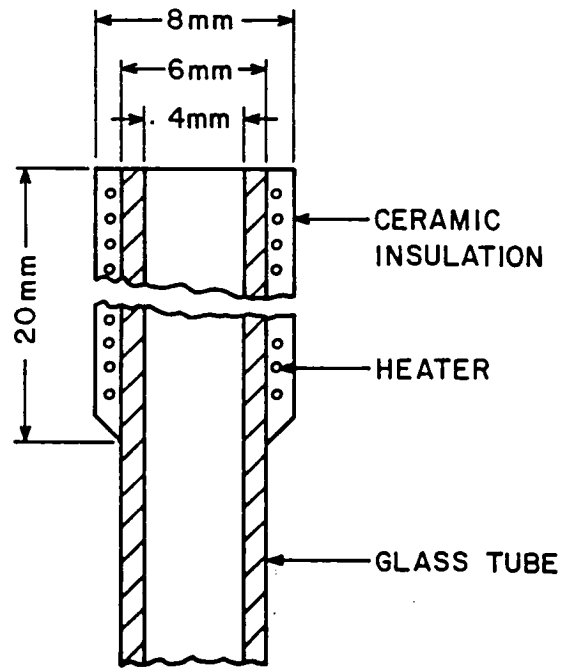
Figure 9. Sketch of the sampling probe for concentration measurements.

Table 4. Summary of Test Conditions for Evaporating Sprays[a]

Flow	Air Jet	Sprays	
Case	--	1	2
Injected fluids	air	air and Freon-11[b]	air and Freon-11[b]
Injector flow rates, mg/s			
Gas	338	138	120
Liquid	0	1450	1894
Loading ratio[c]	0	7.71	15.78
Jet momentum, mN	120.1	105.7	59.7
Initial velocity, m/s[d]	175	64.5	29.64
Reynolds number[d]	2.6×10^4	4.1×10^4	3.6×10^4
SMD, μm[e]	0	30.6	58.1
Spray angle[f]	--	27	29

[a]All flows employ Spraying Systems air-atomizing injector (model 1/4J2050 nozzle, No. 67147 air nozzle, 1.194 mm injector exit diameter). Ambient and injector inlet temperature 300 ± 1 K, ambient pressure, 97 kPa.

[b]Manufactured by Pennwalt Corporation, refrigerant grade, 99.8 purity.

[c]Ratio of injected liquid to gas flow rates.

[d]Assuming LHF. The viscosity of air was employed for the Reynolds number.

[e]Area-weighted average SMD measured by slide impaction at x/d = 50.

[f]Determined from concentration measurements at x/d = 50.

Selection of the SMD of these sprays was done with the aid of slide impaction measurements at x/d = 50. Also shown in Table 4 are the experimental conditions for an air jet test which was used to check experimental techniques [11].

The loading ratio of the sprays was selected to be within the range of most practical liquid-fuel injection systems. Axial and radial profiles of various flow quantities in the sprays were measured using the techniques discussed earlier to obtain a detailed knowledge of the spray structure. In addition, initial conditions of flow quantities were measured so that predictions of the various spray models could be compared with the present measurements.

4. RESULTS AND DISCUSSION

4.1 Introduction

In the following sections the experimental findings concerning the structure of the two evaporating sprays, cf., Table 4 for operating conditions, will be presented. In addition, the comparison of measurements and the predictions of the three theoretical models of spray processes (LHF, DSF and SSF, cf., Section II) will be discussed.

Time-averaged mean and fluctuating velocities were measured but are compared here with predicted Favre averages (the former since Favre- and time-averaged velocities are usually nearly the same [25], the latter due to reasons mentioned in Chapter II). Since concentration measurements by isokinetic sampling are Favre averages and time- and Favre-averaged drop properties are identical, predicted Favre averages apply directly for these properties. Since temperatures were measured with a relatively small thermocouple and are, therefore, closer to time-averaged values, predicted Favre-averaged temperatures were first converted to time averages, using Equation (2.7), before comparing with measurements.

The measurements of mean and fluctuating velocities in the air jet were in good agreement with earlier measurements by Shearer et al. [15] using a similar twin-fluid injector. The comparison between measurements and predictions were also satisfactory. This established an acceptable baseline for measurements in the sprays and these results will not be considered any further here.

4.2 Initial Conditions

4.2.1 Jet Momentum, Spray Angle and Gas-Phase Properties

Due to its small size, measurements at the exit of the injector were limited to mass flow rate and momentum of the two-phase jet. The latter measurement was completed using an impact plate, similar to Reference [15].

Spray angles for the evaporating sprays were determined from concentration measurements, at x/d = 50, to determine the presence of Freon-11 at the edges of the sprays. The values for the case 1 and case 2 sprays are 27° and 29°, respectively.

Due to limitations of spatial resolution, profiles of spray properties were only measured at x/d ≥ 50. For the continuous phase, detailed measurements of mean and fluctuating gas velocities, Reynolds stress and kinetic energy of the gas phase were undertaken at x/d = 50, in order to define initial conditions for the SF computations. These measurements will be illustrated later, when all gas-phase properties are discussed. Also, for the SF computations, initial conditions of mean Freon-11 vapor mass fractions were deduced from liquid flux, drop velocity and total Freon-11 concentration measurements at x/d = 50, while Freon-11 vapor mass fraction fluctuations were estimated from LHF predictions of the fluctuation intensity of the square of mixture fraction fluctuations at x/d = 50. The analysis and procedure for the last two initial conditions for the continuous phase are presented in Appendix D.

4.2.2 Liquid-Phase Properties

Detailed measurements of liquid flux, drop-size distributions and mean and fluctuating drop velocities were also undertaken at x/d = 50 for both the evaporating sprays. Liquid flux measurements were completed by the slide impaction technique as described in Section 3.3.2.3. The results for the case 1 and case 2 sprays are illustrated in Figure 10.

As in the case of the nonevaporating sprays, two techniques were used to measure drop-size distributions at x/d = 50. Drop-size distributions for various radial positions at x/d = 50 for the case 1 and case 2 sprays using the slide impaction technique are illustrated in Figure 11. The same measurements using the double-flash photographic technique are shown in Figure 12. Figure 13 illustrates the radial distribution of SMD across the sprays as calculated from the drop-size distribution data using both techniques. The double-flash photographic technique also yields measurements of drop velocity as a function of size, and these data, at x/d = 50, are illustrated in Figures 14 and 15 for the case 1 and case 2 sprays, respectively.

From Figures 11 and 12, the gross properties of the size distributions for both the case 1 and case 2 sprays do not change with radial location except in small detail, e.g., the increase in the number fraction of the smallest drops. It is difficult to compare the drop-size distributions obtained by the slide impaction and photographic techniques, since: (1) the slide impaction technique yields a temporal average while the photographic technique yields a spatial average; (2) drops with diameters less than 15 μm were not measured by the photographic technique, while the slide impaction data indicates a large number fraction in these sizes; and (3) the size ranges used with each of the techniques are dissimilar. For the case 1 spray, if drops with diameters < 15 μm are disregarded in the slide impaction results, then the peaks of the size distributions obtained by
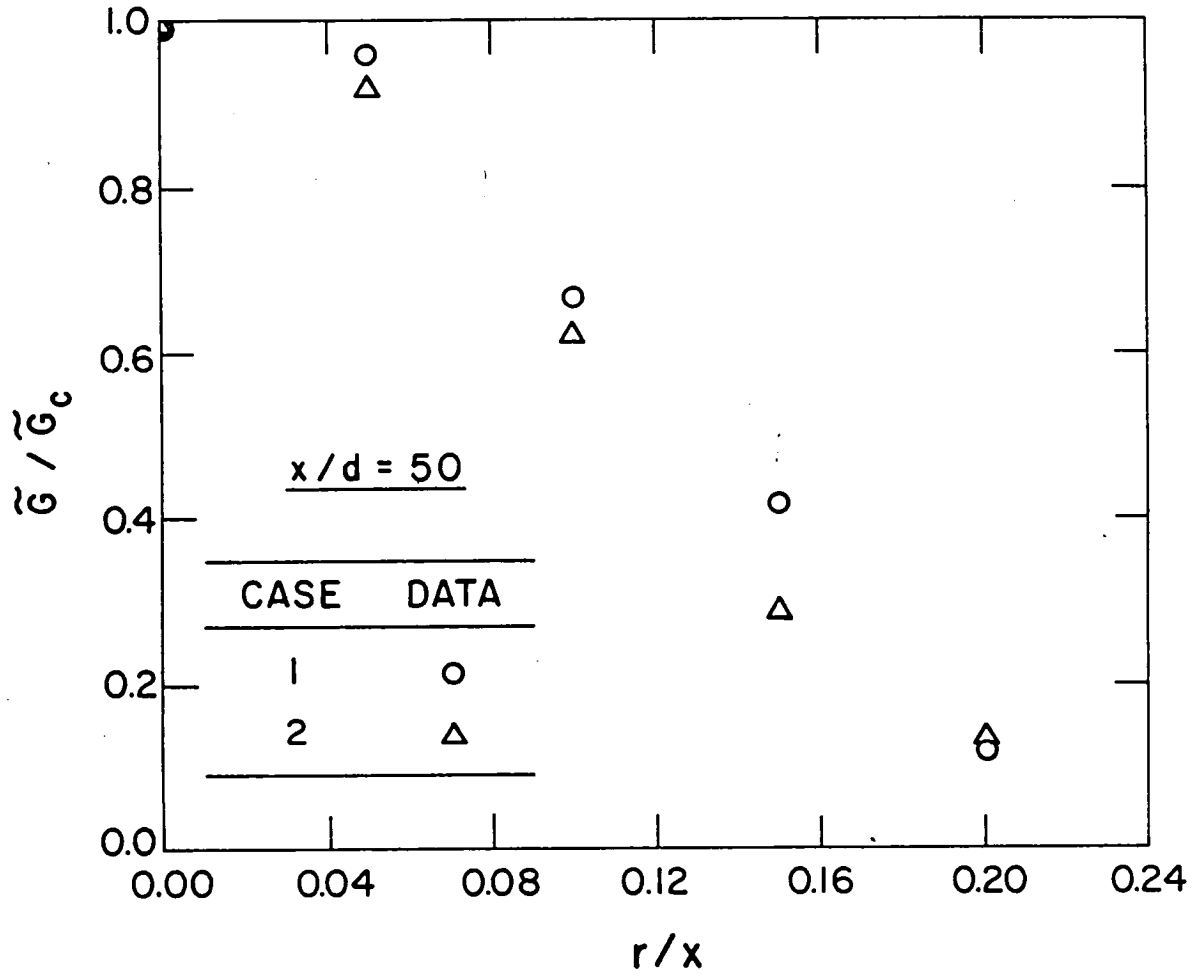
Figure 10.   Initial conditions of liquid flux for
the evaporating sprays at x/d = 50.
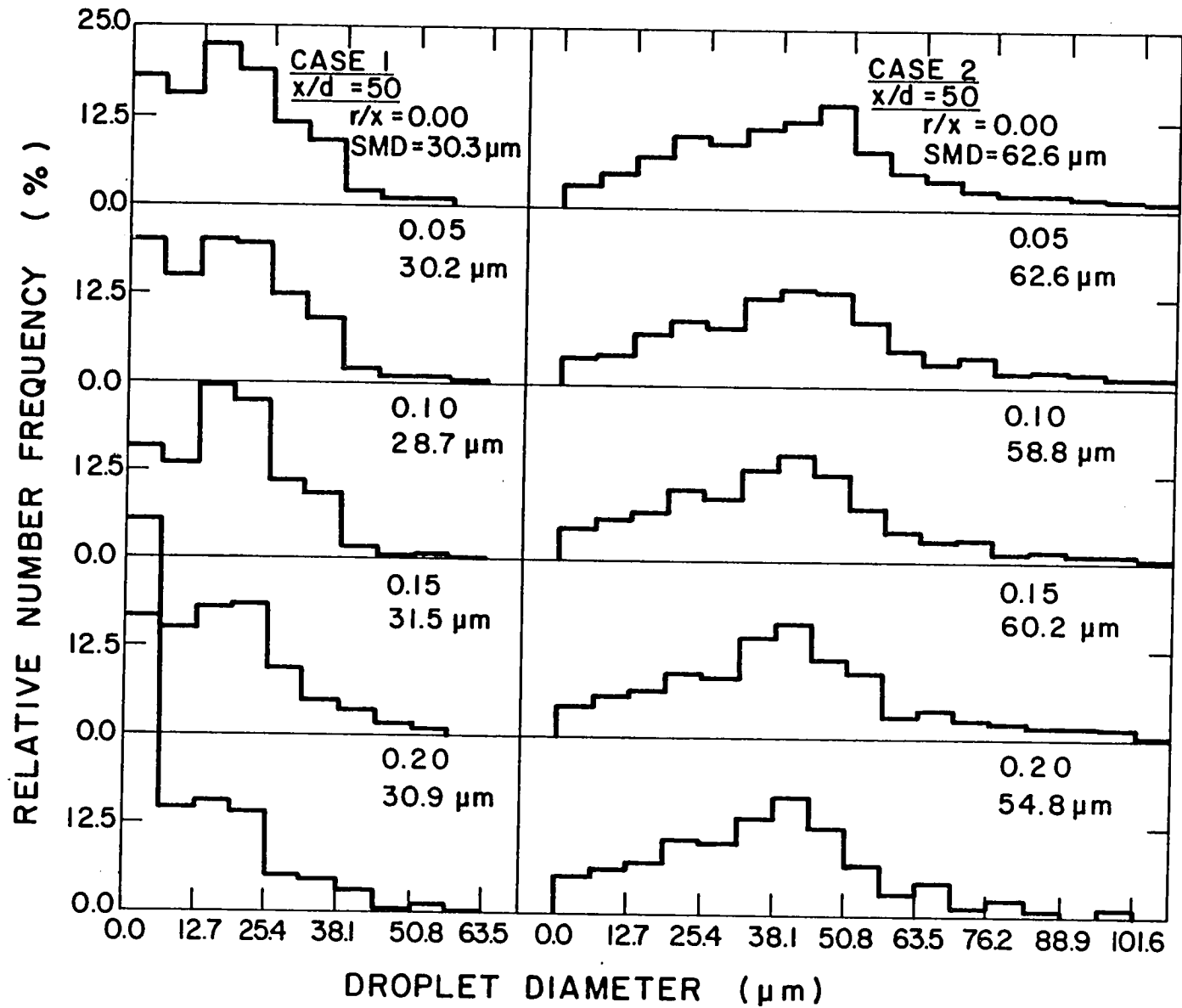
Figure 11. Drop-size distributions for the evaporating sprays at x/d = 50 (slide impaction results).

40
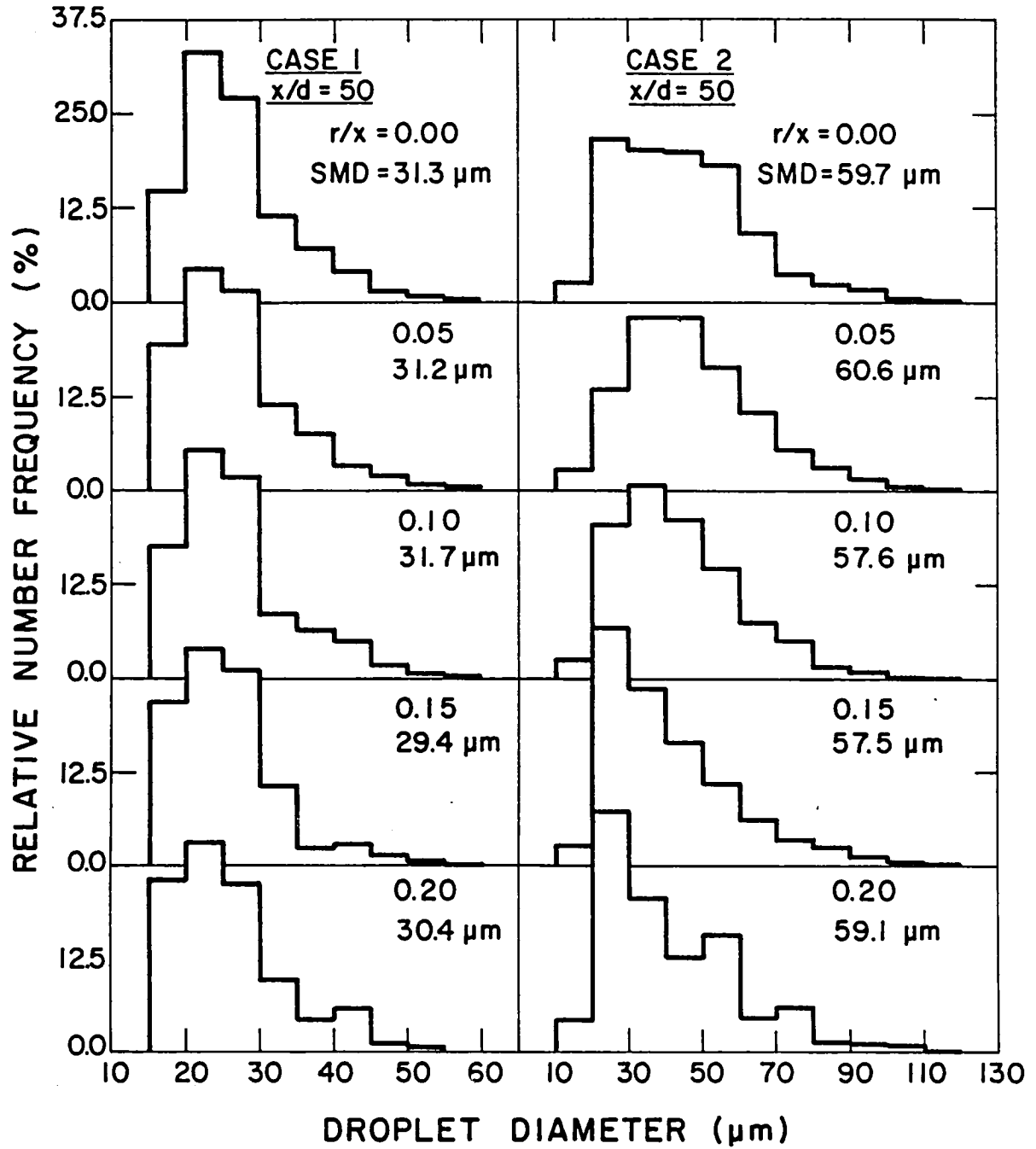
Figure 12. Drop-size distributions for the evaporating
sprays at x/d = 50 (photographic results).
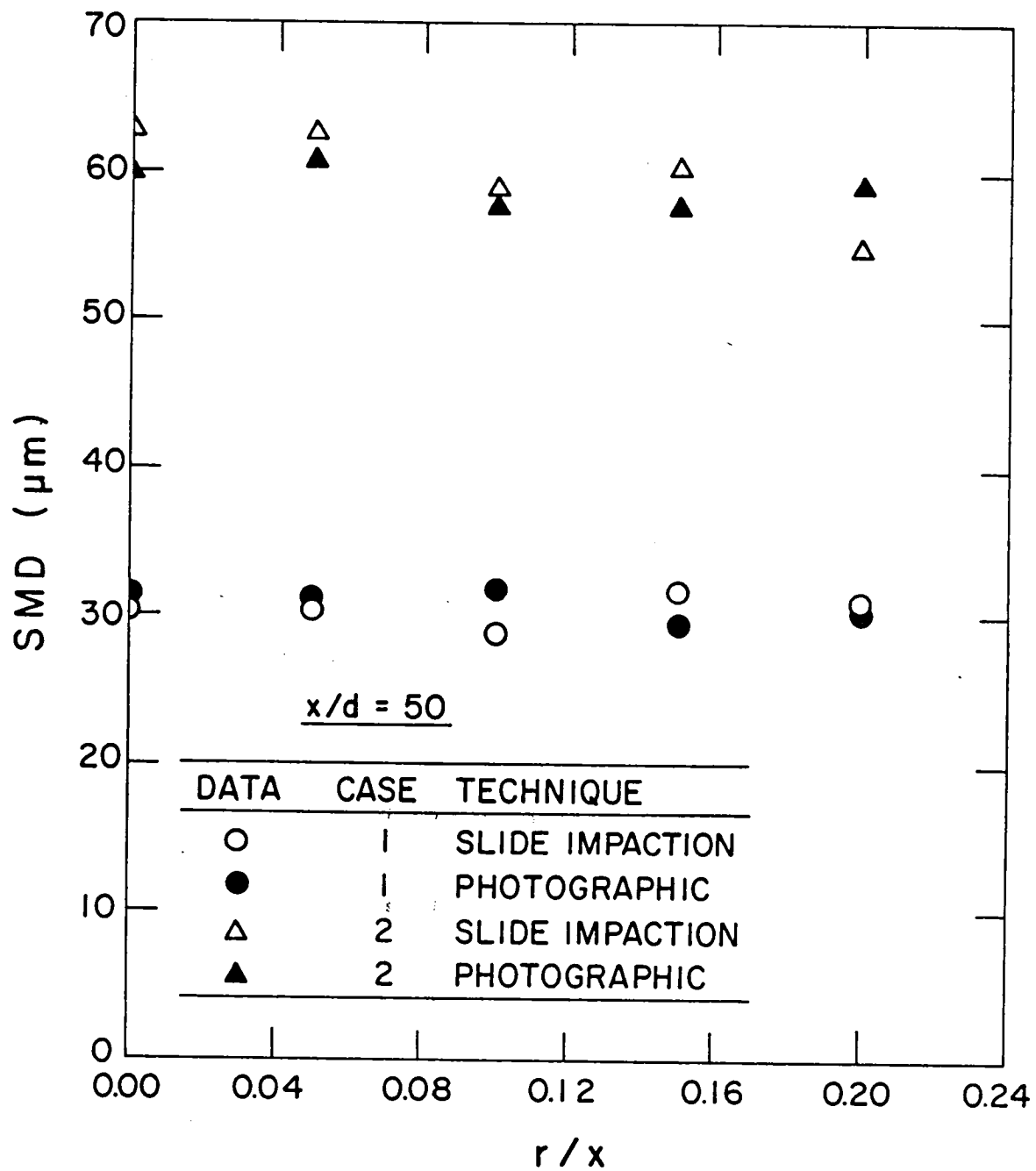
Figure 13. Radial variation of SMD in the evaporating sprays at x/d = 50.
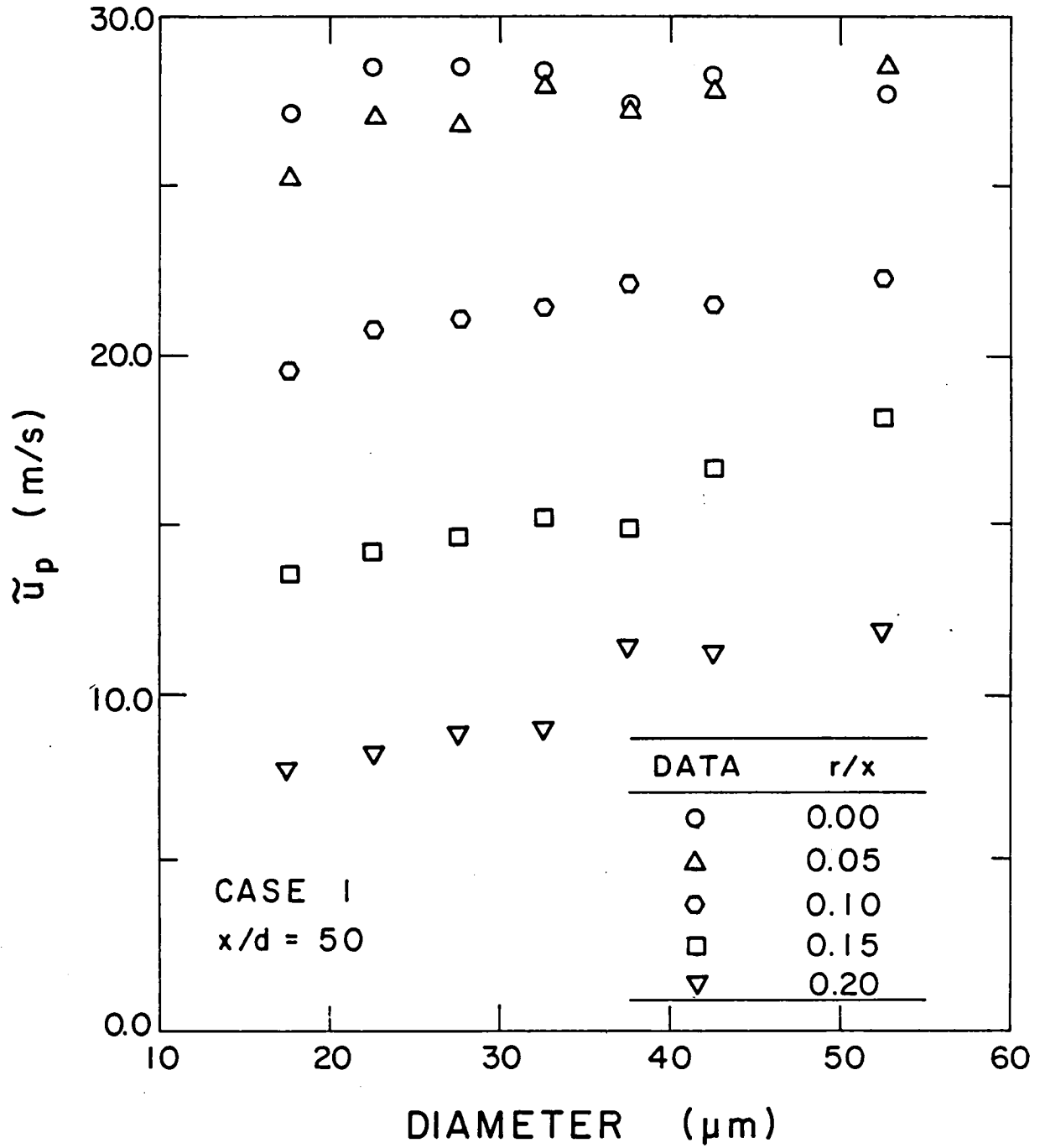
Figure 14. Initial conditions of mean axial drop velocity versus drop size at x/d = 50 for the case 1 evaporating spray.
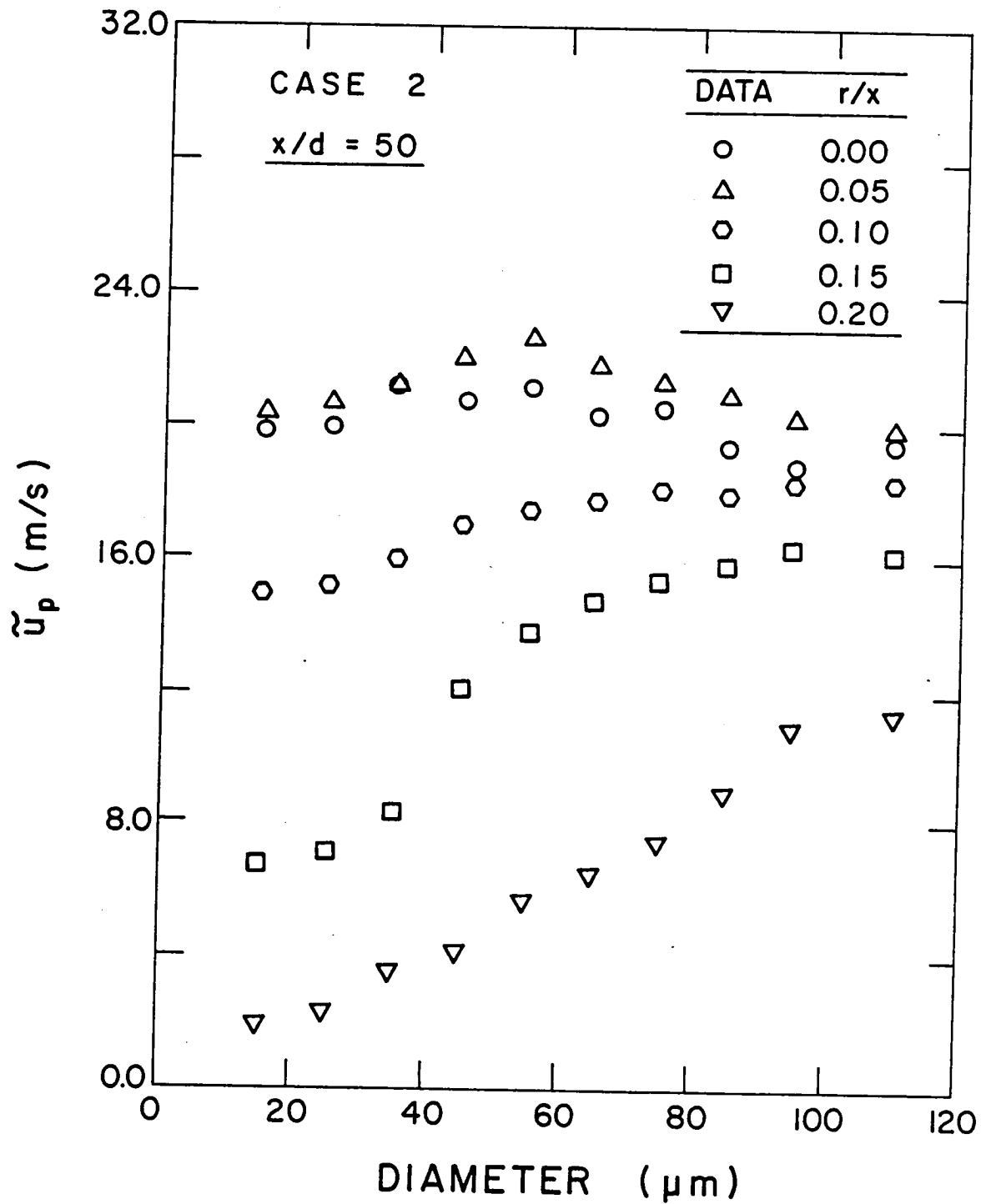
Figure 15. Initial conditions of mean axial drop velocity versus drop size at x/d = 50 for the case 2 evaporating spray.

the two techniques coincide approximately, cf., Figures 11 and 12.
This behavior is expected, since the variation of drop velocity with
size is moderate at this location, cf., Figure 14. The same general
observation can be made for the case 2 spray, however, with increasing
r/x positions the peaks in the size distributions obtained using the
slide impaction technique occur at diameters larger than in the case of
the photographic technique since the drop velocity varies significantly
with drop size at larger r/x positions, cf., Figure 15.

Except for the details noted above, differences between the slide
impaction and photographic techniques are small, since the SMD obtained
using both techniques compare well, cf., Figure 13. This is due to the
relatively insignificant contribution to the SMD of the smallest size
drops, and also suggests only moderate influence of velocity bias.
Finally, the SMD is nearly invariant over the cross-section of the
spray, similar to the behavior observed with the nonevaporating sprays
for the same location and injector [10,11].

The variation of mean drop velocity as a function of drop size and
radial position at x/d = 50 is illustrated in Figures 14 and 15 for the
two sprays. Drop velocities are relatively independent of size near
the axis, but tend to increase with size near the edge of the flow.
With the exception of drops having diameters $\leq$ 25 μm at the edges of
the case 2 spray, drops of all sizes and at all radial positions in
both sprays were found to possess axial velocities 5-400% above the
local gas-phase velocities (to be shown later).

Initial conditions of fluctuating axial drop velocities as a
function of drop size and radial location at x/d = 50 are illustrated
in Figures 16 and 17 for the two sprays. The measurements exhibit a
great deal of scatter, similar to the data for the nonevaporating
sprays for the same location and injector [10,11]. This behavior is
expected at this location due to the relative proximity of the injector
exit. The relative fluctuation levels (relative to the mean axial drop
velocities at the centerline) were between 6-17%, which is lower than
the nonevaporating spray data at the same location.

As mentioned earlier, the photographic method did not provide
sufficient resolution to measure mean and fluctuating radial drop
velocities. Hence, for SF model computations, the initial mean radial
drop velocity was assumed to increase linearly from the spray axis to
the edge of the flow, matching the spray angle at the latter condition,
viz., $\bar{v}_p$ = 0.7 $\bar{u}_p$ r/x. Initial conditions of fluctuating radial drop
velocities were specified to be a constant ratio of the corresponding
measured fluctuating axial drop velocity, viz., $(\bar{v}_p''^2)^{1/2} = (\bar{u}_p''^2)^{1/2}/3.0$.
These specifications were made with the help of limited photographic
observations and are exactly the same as that used for the
nonevaporating sprays [10,11], since the injector and the location are
the same for both types of sprays. The sensitivity of the predictions
of these estimates and other initial conditions will be considered
later.
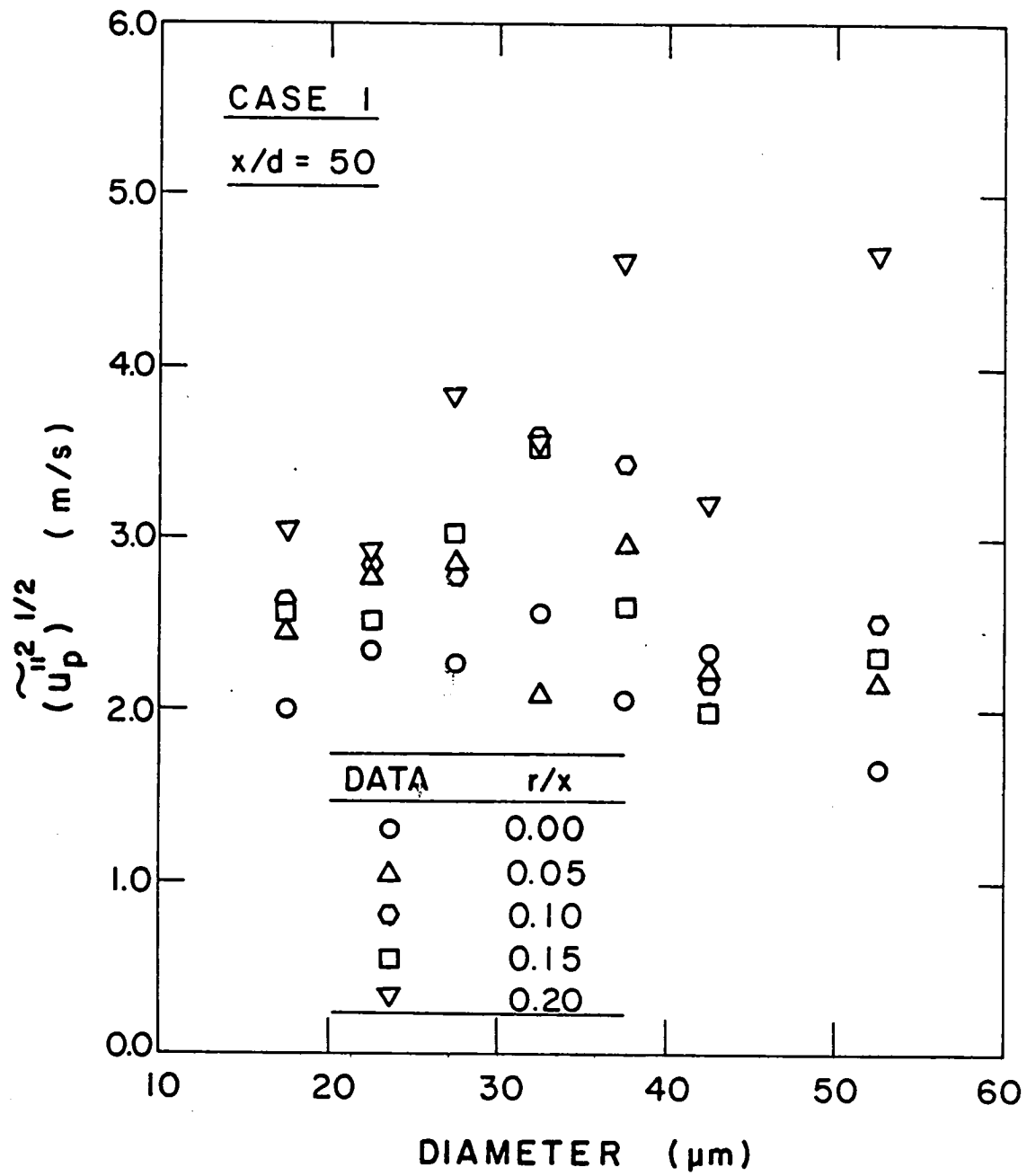
Figure 16.   Initial conditions of fluctuating axial drop velocity versus drop size at x/d = 50 for the case 1 evaporating spray.
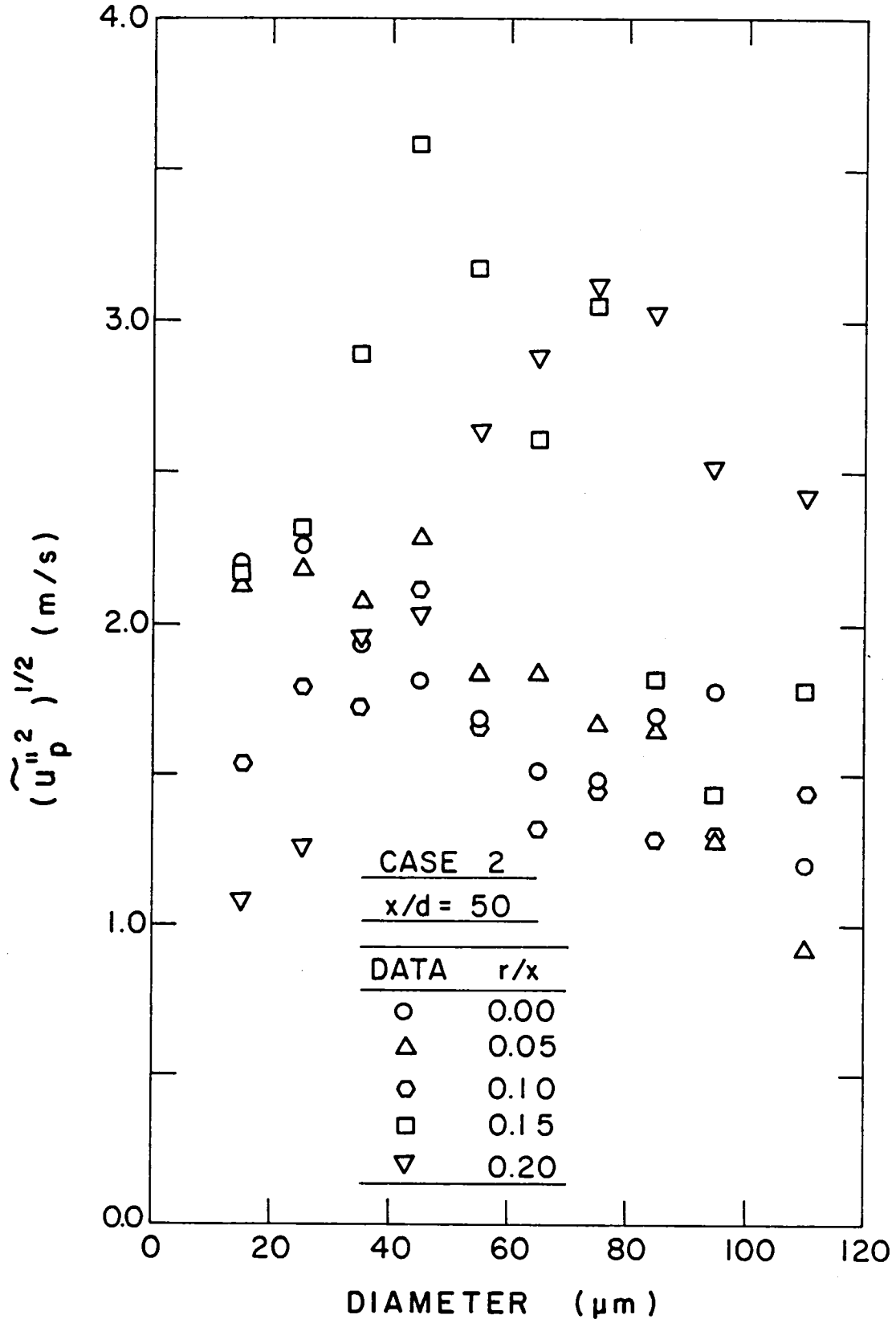
Figure 17. Initial conditions of fluctuating axial drop velocity versus
drop size at x/d = 50 for the case 2 evaporating spray.

## 4.3 Axial Variation of Spray Properties

Having established initial conditions, the remaining measurements were used to evaluate model predictions; beginning at the injector exit for the LHF model and at x/d = 50 for both the SF models.

Predicted (LHF and SSF models) and measured mean gas-phase velocities along the axis of the two sprays are illustrated in Figure 18. The LHF model overestimates the rate of development of the sprays, with performance deteriorating as the SMD of the spray increases. This behavior is similar to the recent nonevaporating spray results in this laboratory [10-11], as well as past findings for evaporating sprays [1,15]. In contrast, the SSF model provides satisfactory predictions for both sprays.

Similar results for mean total mass fraction of Freon-11 (both liquid and gas phases) are shown in Figure 19. In this case, predicted mean mixture fraction is illustrated for the LHF model, since the two quantities are proportional under the LHF approximation. The data of Shearer et al. [15] for a Freon-11 spray with SMD and loading ratio very similar to the case 1 spray of the present study is also shown for comparison. The performance of the LHF model is again poor, due to neglect of slip and loss of thermodynamic equilibrium. In general, the SSF model provides reasonably good predictions over the range where it was used.

Predicted (DSF and SSF models) and measured mean axial drop velocities for the two sprays are illustrated in Figures 20 and 21. The SSF model predicts a somewhat more rapid deceleration than the DSF model for each drop size, due to the nonlinearity of the drop drag law interacting with turbulent fluctuations. Both models provide fair agreement with measurements particularly at large x/d. Larger errors at x/d near 100 probably result from errors in the specification of initial conditions, since initial rates of dispersion are sensitive to estimates of initial velocity fluctuations.

SSF model predictions of fluctuating axial drop velocities generally underestimated the measurements, just as in the case of the nonevaporating spray study [10,11]. As described in Section 3.3.2.2, measurements of fluctuating axial drop velocities were of limited accuracy and were generally inconclusive for SSF model evaluation due to the added uncertainties in the initial conditions for these properties; therefore, these results will not be considered here.

Figure 22 is an illustration of the variation of SMD along the axis of the two sprays. For nonevaporating sprays, turbulent drop dispersion causes the SMD to increase with increasing x/d due to drop dispersion, [10,11]. For the evaporating sprays, however, this effect is counteracted by drop evaporation; therefore, the SMD remains relatively constant until the largest drops finally evaporate. Predictions of both the DSF and SSF models are comparable and are in fair agreement with measurements, suggesting that effects of dispersion are less significant for evaporating sprays than for nonevaporating sprays.

48
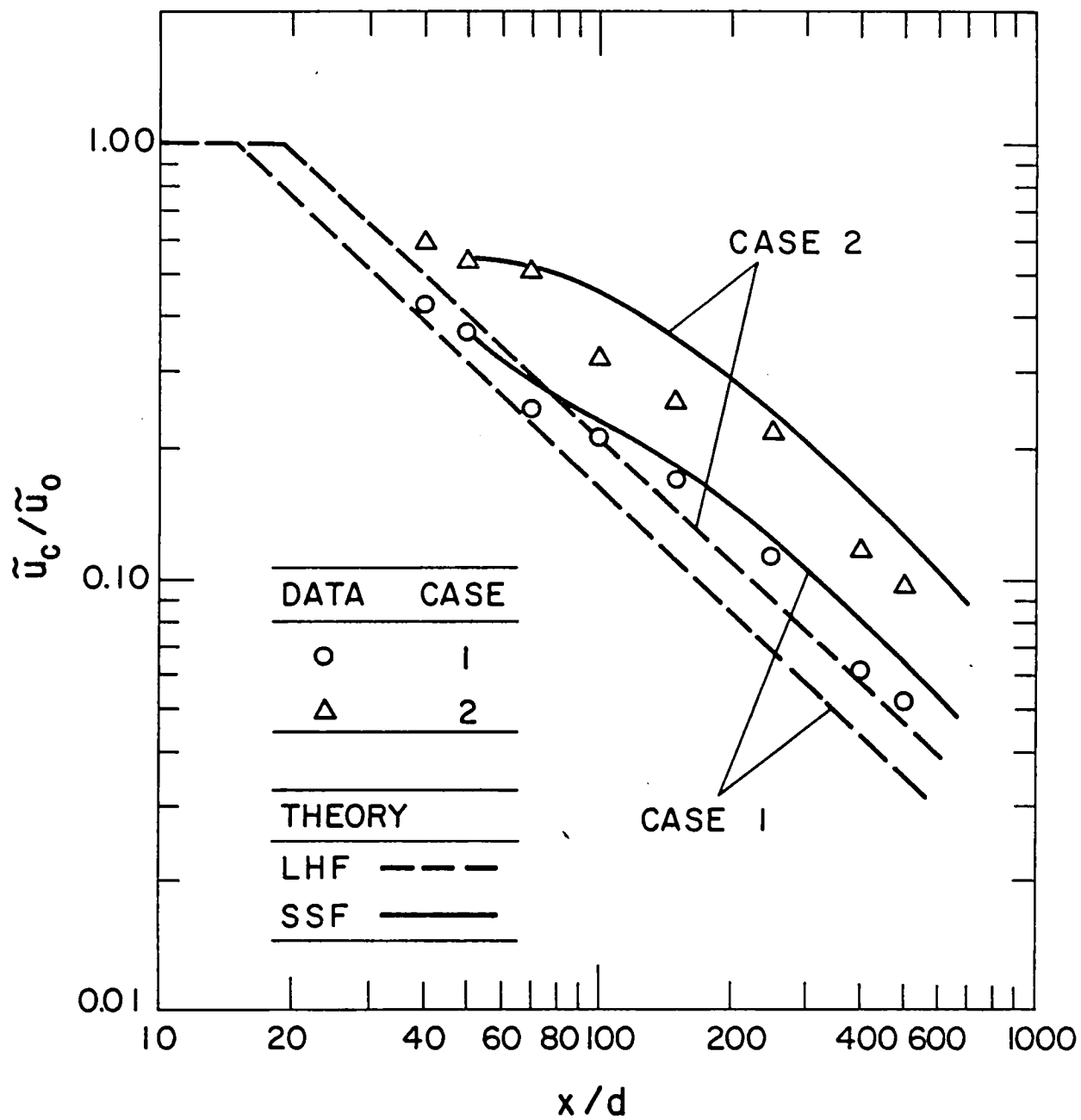
Figure 18. Predicted and measured mean gas-phase velocities along the axis of the evaporating sprays.
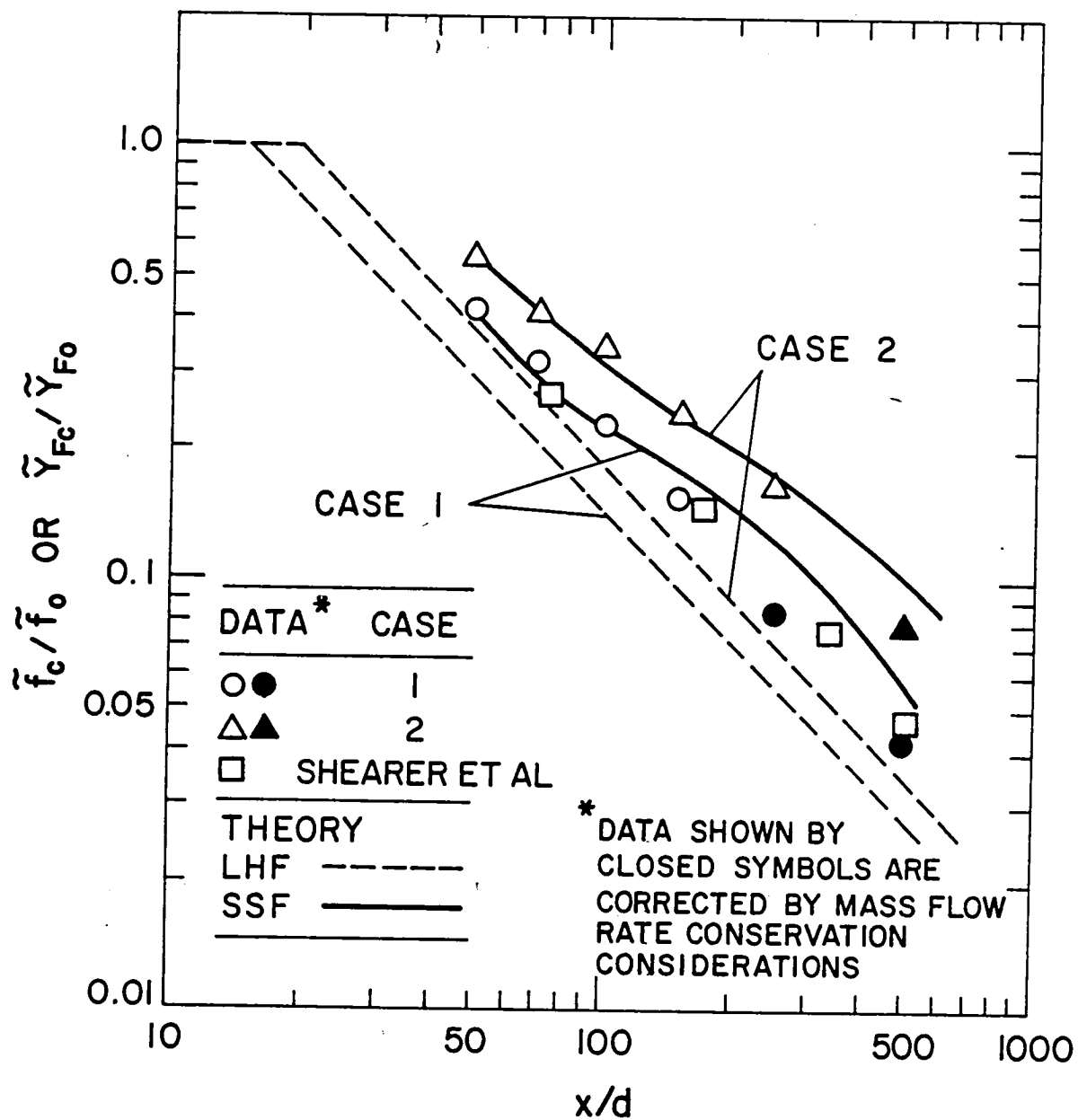
Figure 19. Predicted and measured mean mixture fraction
(LHF) or total Freon-11 mass fraction (SSF)
along the axis of the evaporating sprays.
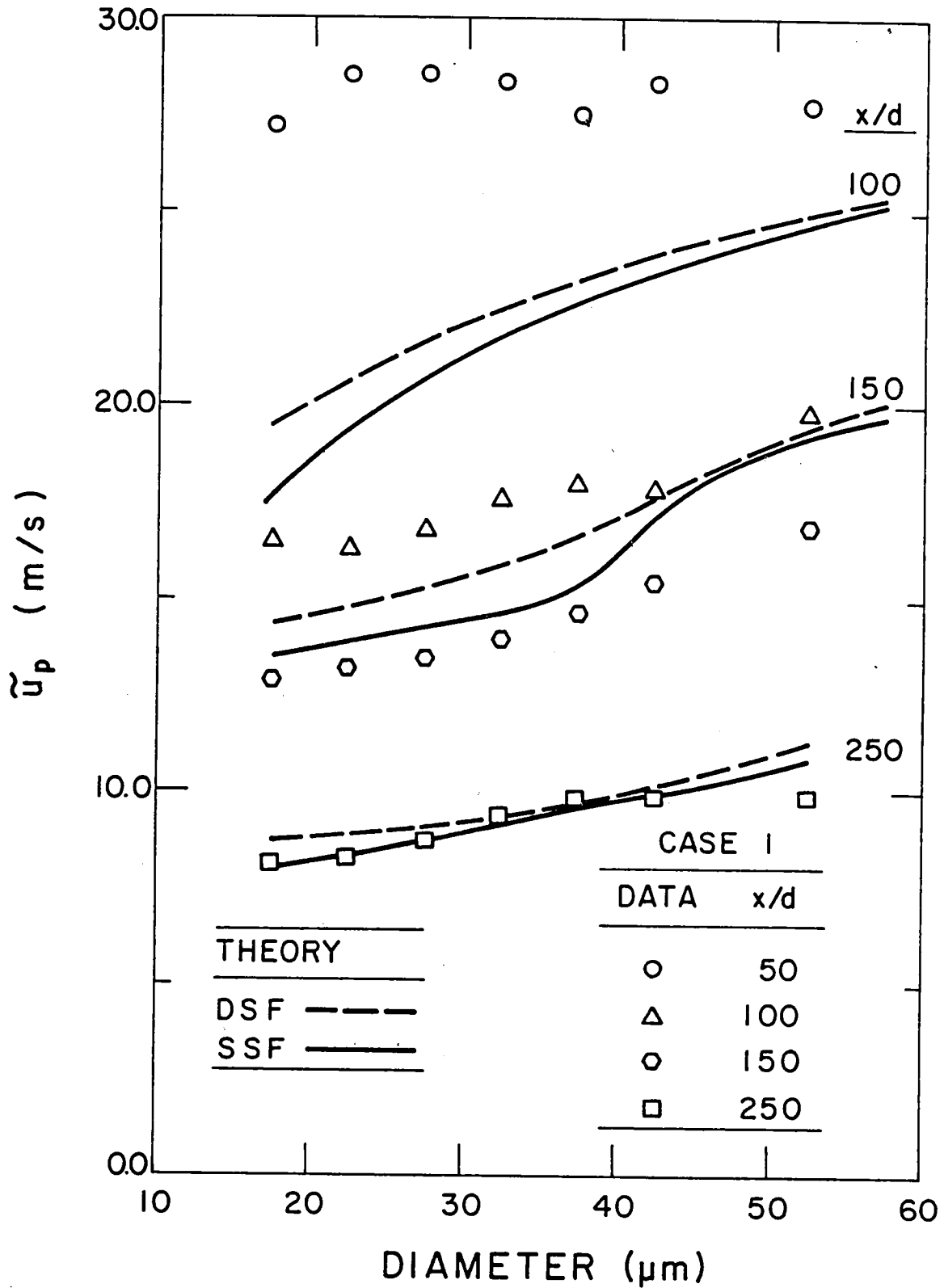
Figure 20. Predicted and measured mean axial drop velocities along the axis of the case 1 evaporating spray.
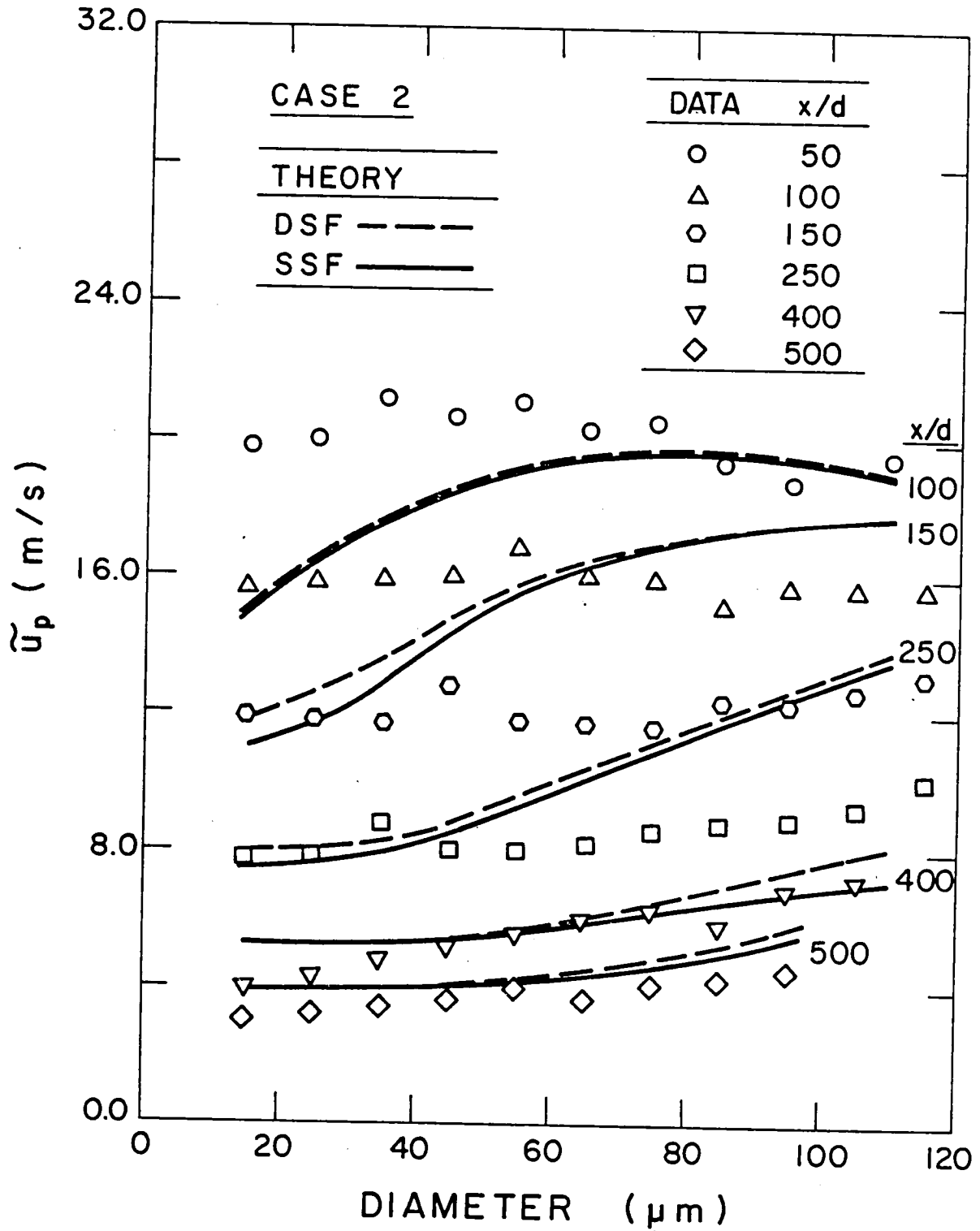
Figure 21.   Predicted and measured mean axial drop velocities
along the axis of the case 2 evaporating spray.
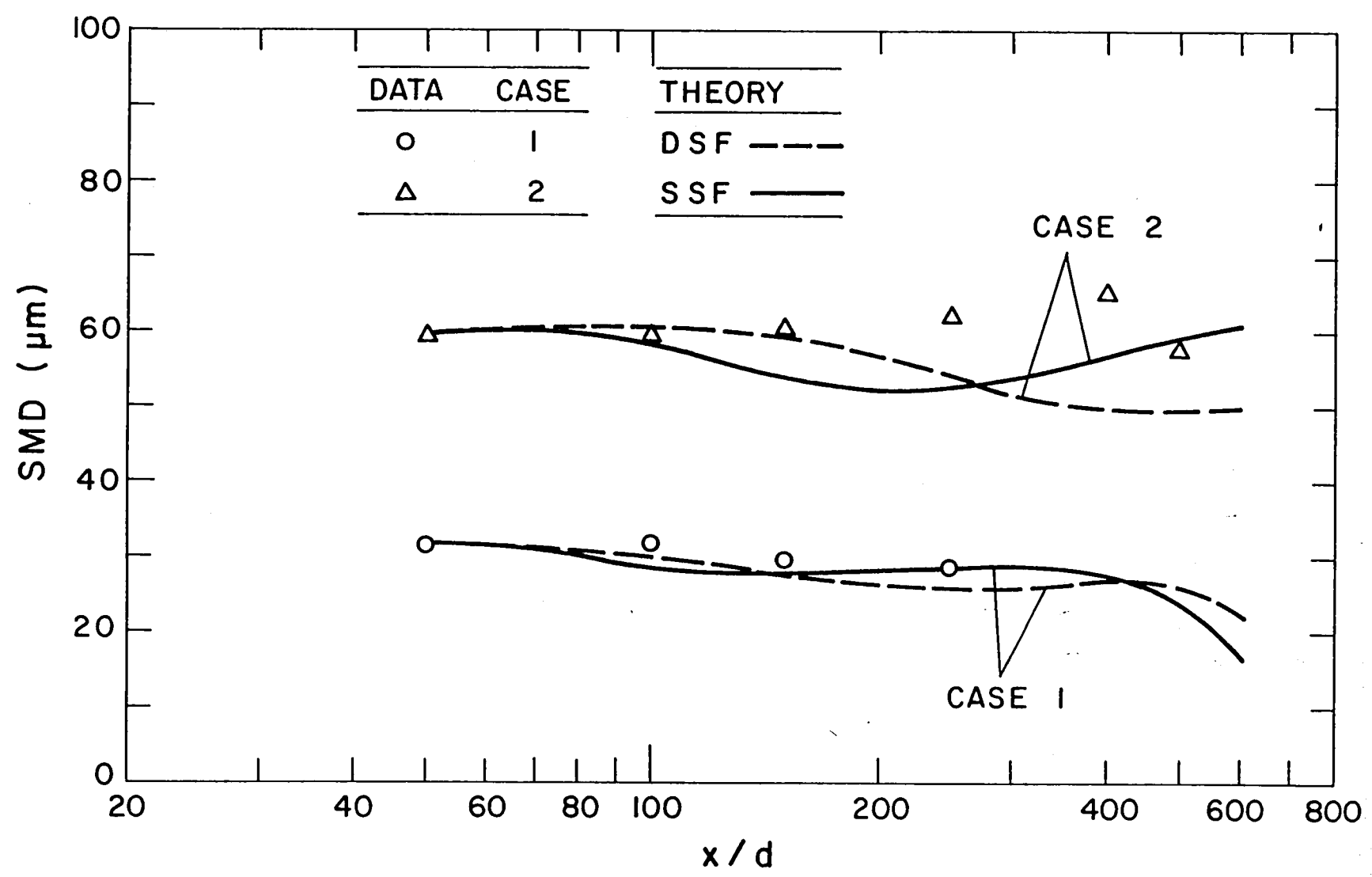
Figure 22. Predicted and measured SMD along the axis of the evaporating sprays.

Measurements of drop-size distributions along the axis of the two sprays are illustrated in Figure 23. Drop evaporation and drop dispersion counteract one another, so that the overall character of the size distributions remain approximately the same, until the largest drops finally begin to disappear.

Figure 24 is an illustration of the comparison between the predictions (LHF and SSF models) of the axial variation of the mean gas-phase temperature with some limited experimental results. Predictions of the LHF and SSF models shown are time-averaged values. The poor performance of the LHF model is similar to the results of Shearer et al [15], and shows the effect of the loss of kinematic and thermodynamic equilibrium. The SSF model, on the other hand, better predicts the measurements and tends to approach the data at large values of x/d for the case 1 spray. The discrepancies between the measurements and the predictions of the SSF model at smaller values of x/d for the case 1 spray, and where data is available for the case 2 spray, may probably be attributed to errors in the measurements. In spite of the fact that a shielded thermocouple was used for the measurements, the smaller drops could impinge and subsequently vaporize on the thermocouple bead--due to the lower collection efficiency of the shield for the smaller drops, cf., Section 3.3.1.2.

Predicted (DSF and SSF models) mean liquid flux along the axis of the two evaporating sprays is illustrated in Figure 25. The predicted centerline liquid fluxes are normalized by the initial condition values at x/d = 50. Both models predict similar results up to x/d ≅ 250 for the case 1 spray. However, the SSF model predicts a slightly more rapid decrease in liquid flux in the remaining downstream region of the flow. For the case 2 spray, the DSF model predicts a more rapid decrease of the centerline liquid flux than the SSF model. However, as will be seen later, the DSF model predicts peaked radial profiles, suggesting that DSF model predictions of centerline liquid flux are largely dominated by initial conditions of drop properties.

4.4 Radial Variation of Mean Spray Properties

Predicted (LHF and SSF models) and measured radial profiles of mean gas-phase velocity are illustrated in Figure 26. In this and the following figures, radial distances are normalized by distance from the injector (which is the similarity variable for fully-developed constant density single-phase jets [1]) so that model predictions of flow width can be seen directly. Unlike most particle-laden jets [1], the flow-widths of these sprays are generally greater than predictions of the LHF model due to enhanced dispersion of drops by turbulence. This behavior, however, was much more pronounced for the nonevaporating sprays investigated earlier [10,11]. The effect is reduced here, since drops evaporate quite rapidly as they reach nearly pure air near the edge of the flow--tending to limit their radial dispersion as drops.

Predicted and measured radial profiles of total (gas and liquid) mean Freon-11 concentration are illustrated in Figure 27 for both sprays. Predictions of all three models are shown (the LHF prediction

54
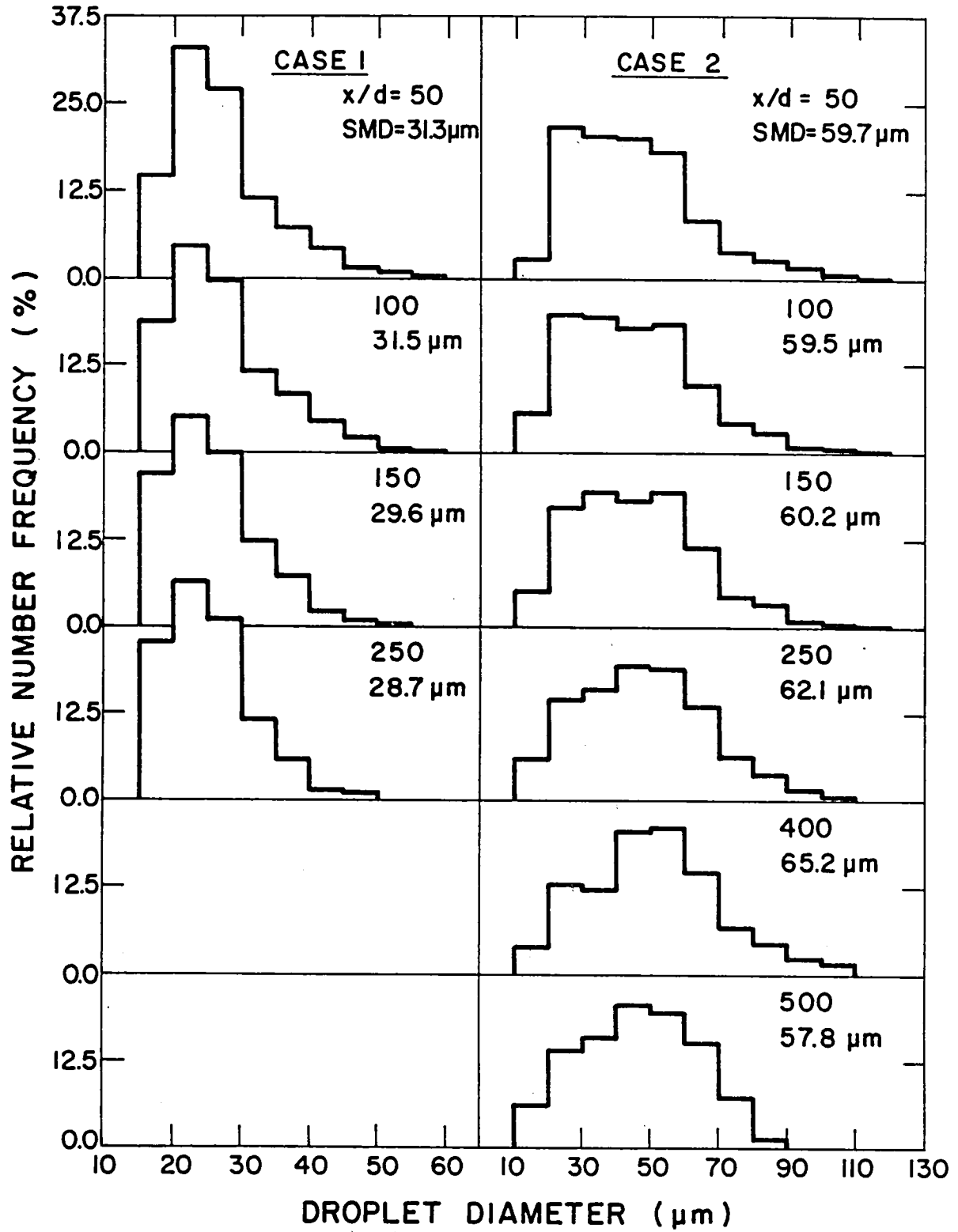
Figure 23. Drop-size distributions along the axis of
the case 1 and case 2 evaporating sprays.
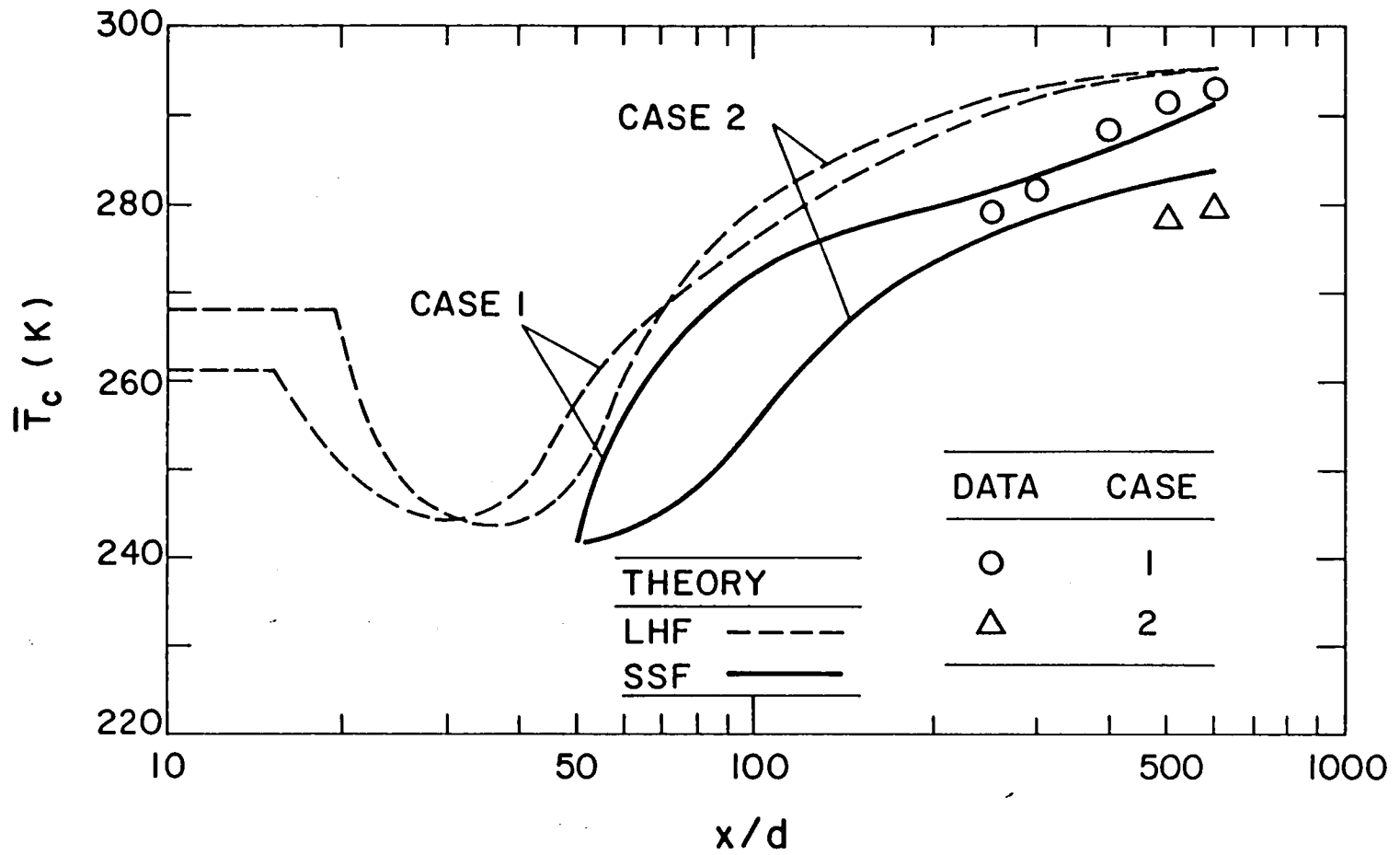
Figure 24. Predicted and measured mean gas-phase temperature along the axis of the evaporating sprays.
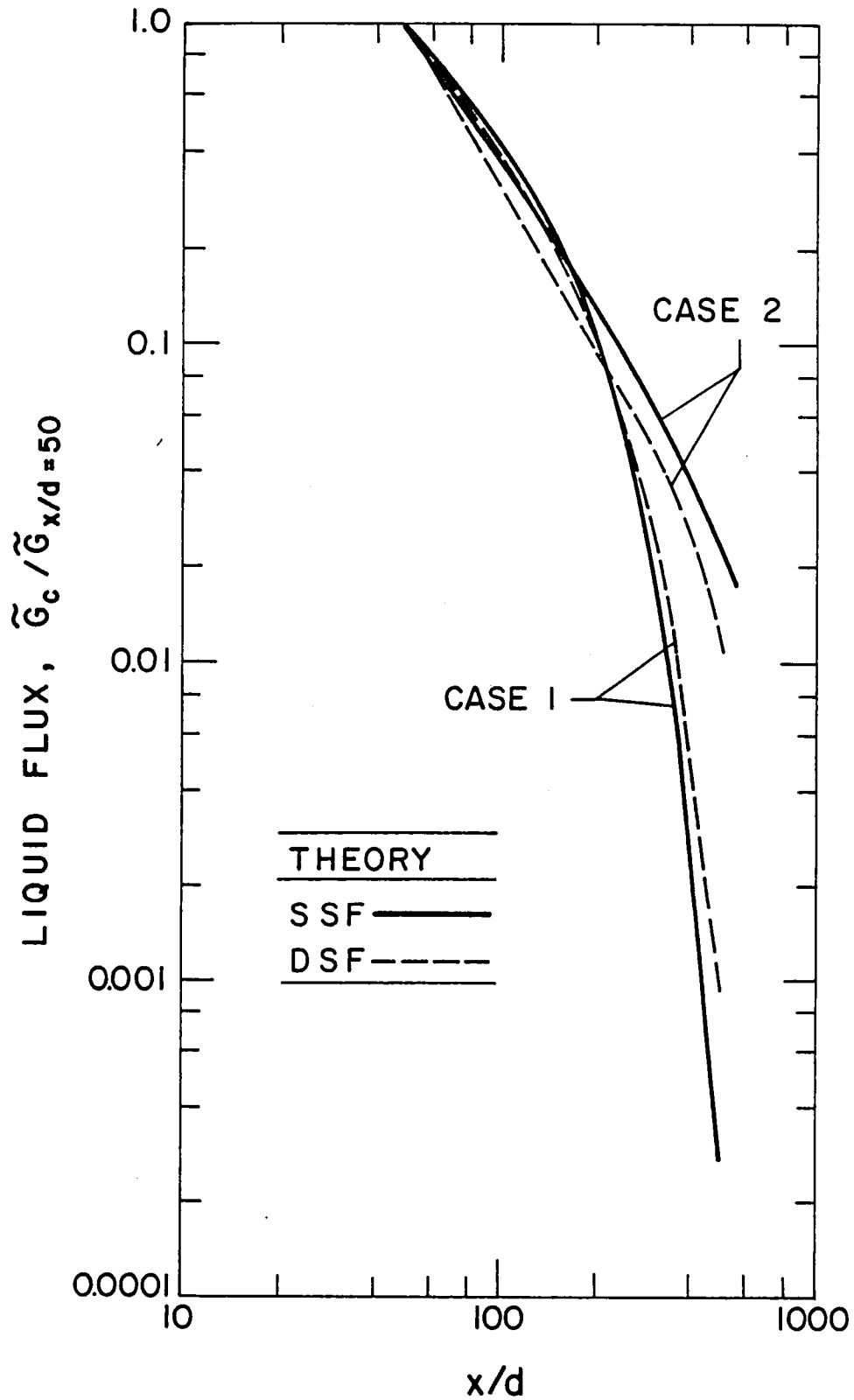
Figure 25. DSF and SSF model predictions of mean liquid
flux along the axis of the evaporating sprays.
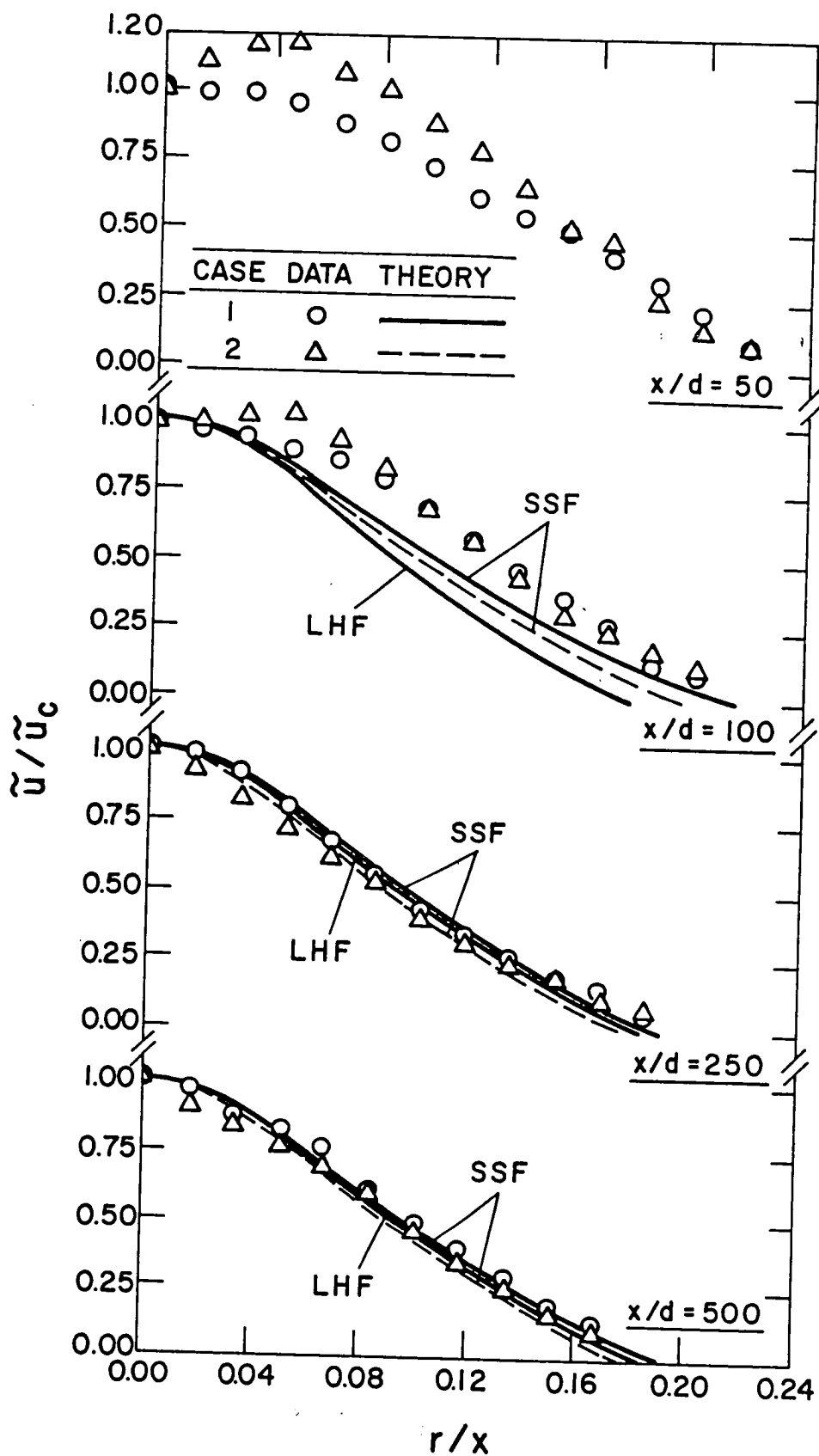
Figure 26. Predicted and measured radial variation of mean
gas-phase velocities in the nonevaporating sprays.
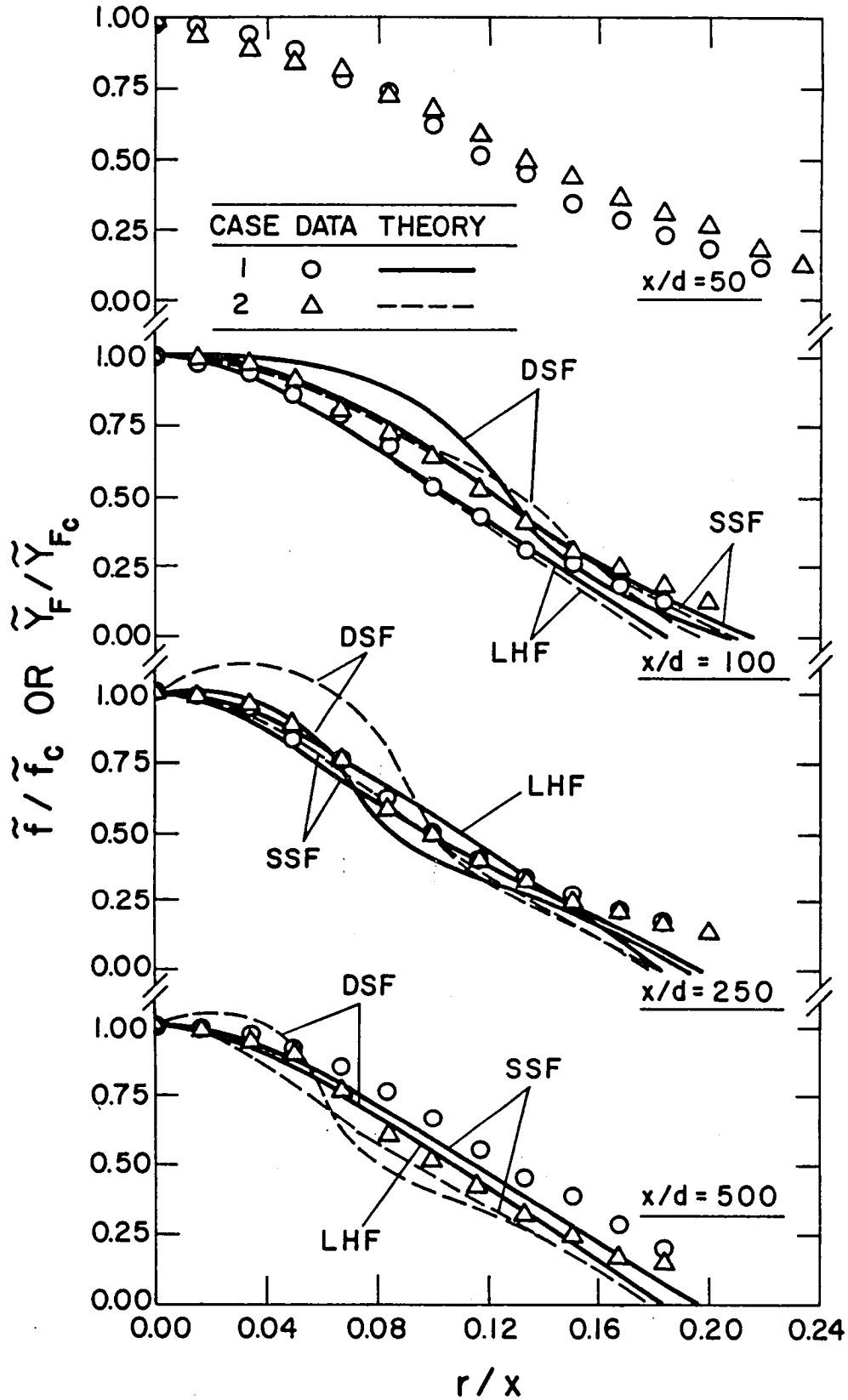
Figure 27. Predicted and measured radial variation of
mixture fraction (LHF) or total Freon-11
mass fraction (SSF) for the evaporating sprays.

formally being $\tilde{f}/\tilde{f}_c$ as before). The DSF model yields a peaked profile due to neglect of turbulent dispersion of drops, while the LHF and SSF models provide better agreement with measurements. In general, discrepancies between the LHF and DSF models and measurements are smaller than comparable measurements in the nonevaporating sprays, since Freon-11 vapor tends to dominate the concentration measurement for present test conditions. Turbulent dispersion of drops, however, increases the width of the flow in comparison to single-phase jets [1]--an effect which decreases at large x/d where the drops have evaporated.

Predicted (LHF and SSF models) and measured radial variation of the normalized gas-phase temperature decrement for the two sprays are illustrated in Figure 28. The data at x/d = 250 in the case 1 spray and x/d = 500 in the case 2 spray show some evidence of bias in the measurements, due to drop impingement on the thermocouple at the center of the spray. Far downstream at x/d = 500 in the case 1 spray, where all the drops have evaporated, the profile is reasonable and agrees well with the predictions--particularly the SSF model.

Predicted (DSF and SSF models) radial variation of mean liquid flux at various axial locations in the two sprays are illustrated in Figure 29. Similar to the results obtained for the nonevaporating sprays, the DSF model predicts peaked profiles and narrower flow widths than the SSF model, due to the neglect of turbulent dispersion of drops. The comparison between the results of the DSF and SSF models shown in Figure 29, in conjunction with those shown in Figure 25 for the axial variation of liquid flux emphasizes the effect of turbulent dispersion on interphase transport rates.

4.5 Radial Variation of Gas-Phase Turbulence Properties

Figures 30 and 31 illustrate results for gas-phase turbulence kinetic energy and Reynolds stress for the two evaporating sprays. Both these quantities are quadratic, which amplifies discrepancies between predictions and measurements. The comparison between predictions and measurements is reasonably good for the case 1 spray, but poorer agreement is observed for the more heavily-loaded case 2 spray. This trend could be due to effects of turbulence modulation, discussed by Al Taweel and Landau [28], which were ignored during the present calculations. Unusually low values of Reynolds stress are observed for the more heavily-loaded case 2 spray at x/d = 100 and 250. This effect could be due to bias of the measurements by drops, since fluctuating radial particle velocities are significantly smaller than radial gas fluctuations in two-phase jets [7,8].

Effects of the presence of drops on turbulence properties are more evident when individual components of velocity fluctuations are examined. Measured radial profiles of u', v' and w' are illustrated in Figures 32 and 33 for the case 1 and case 2 sprays. Predictions of the SSF model were obtained assuming $(\bar{u}''^2:\bar{v}''^2:\bar{w}''^2) = (1:0.5:0.5)$ k, which is approximately observed in the fully-developed region of single-phase round jets [29,30]. The results are similar to those
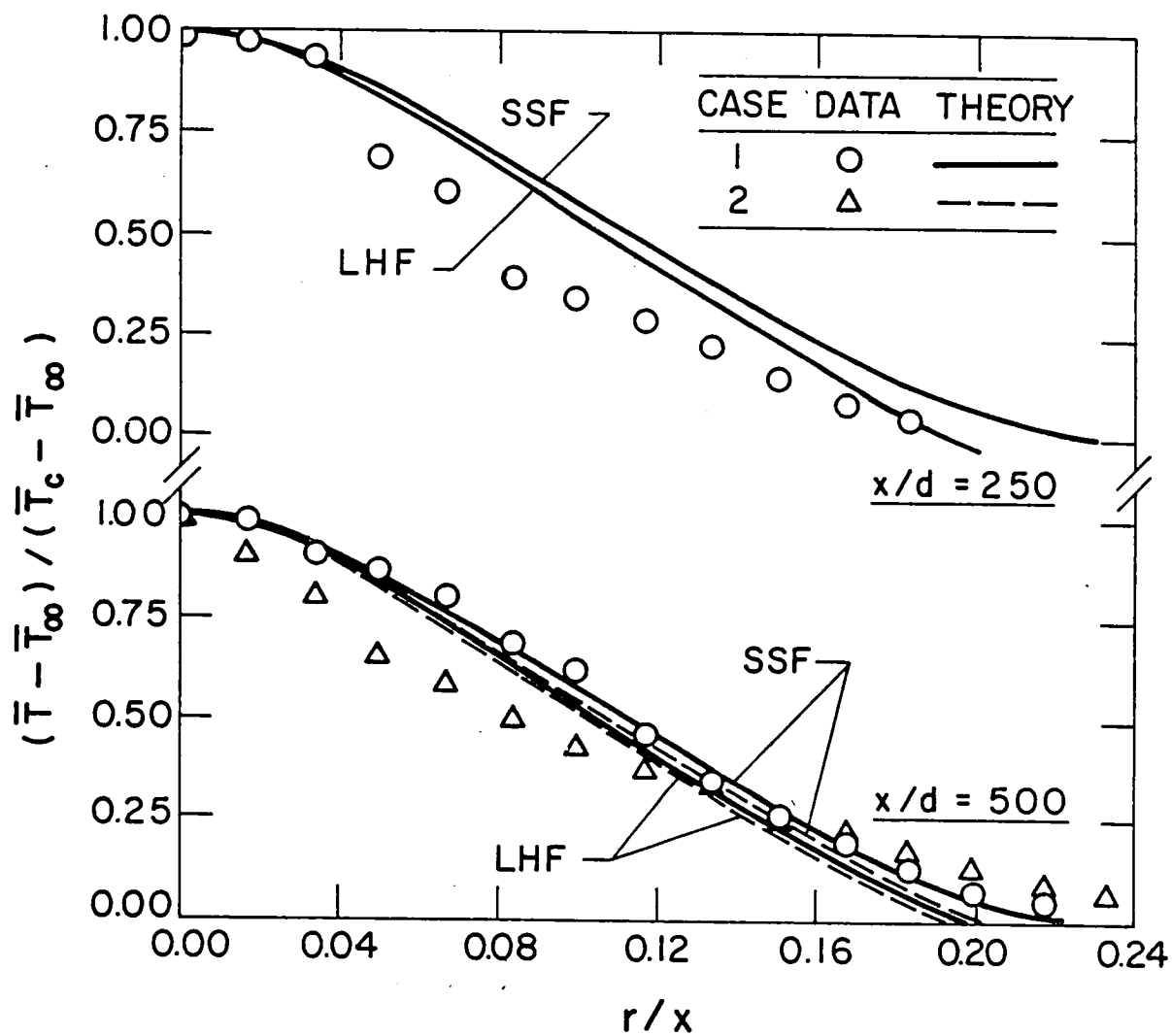
Figure 28. Predicted and measured radial variation of mean
gas-phase temperature in the evaporating spray.
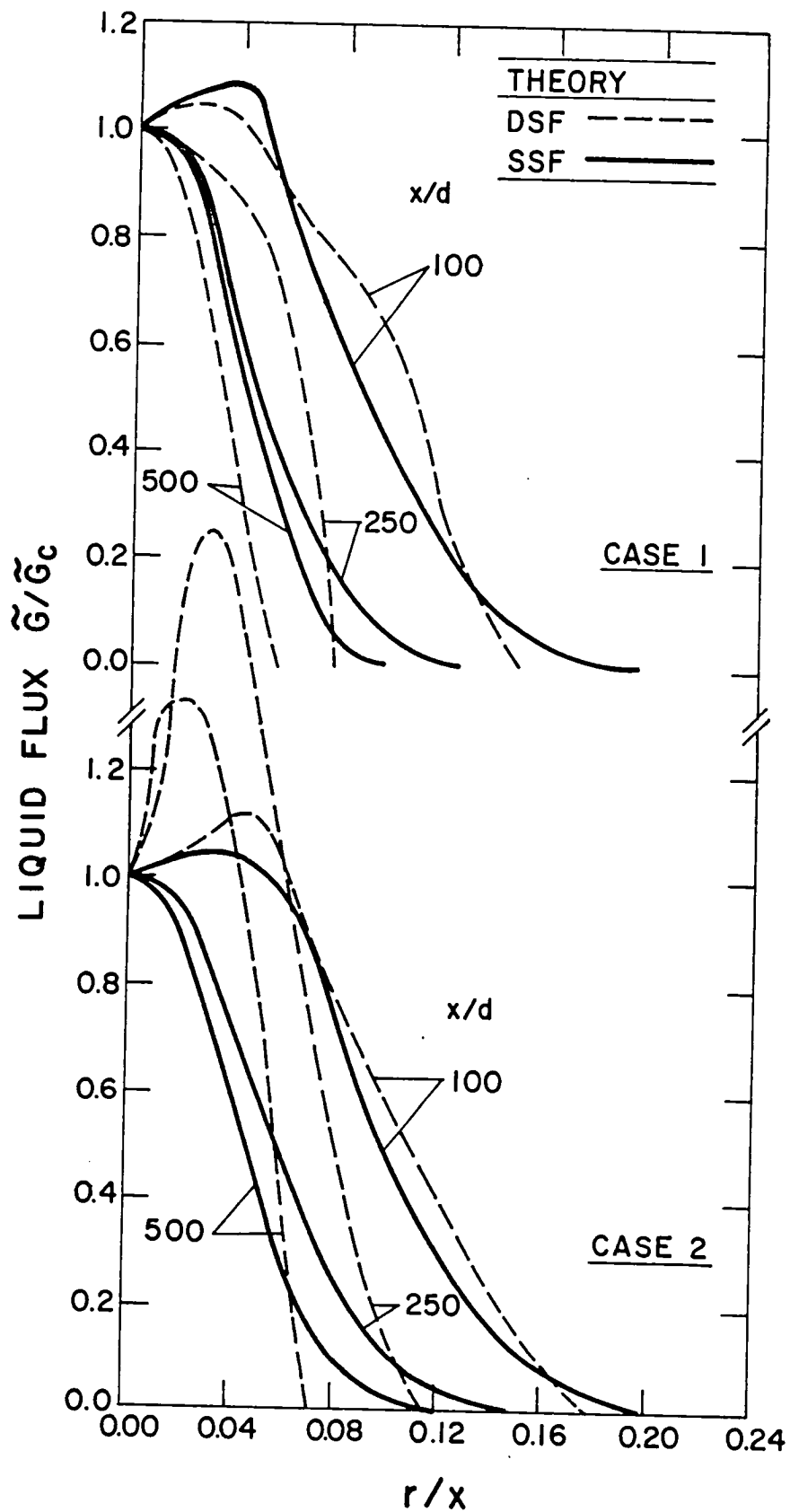
Figure 29. DSF and SSF model predictions of the radial variation of mean liquid flux in the evaporating sprays.
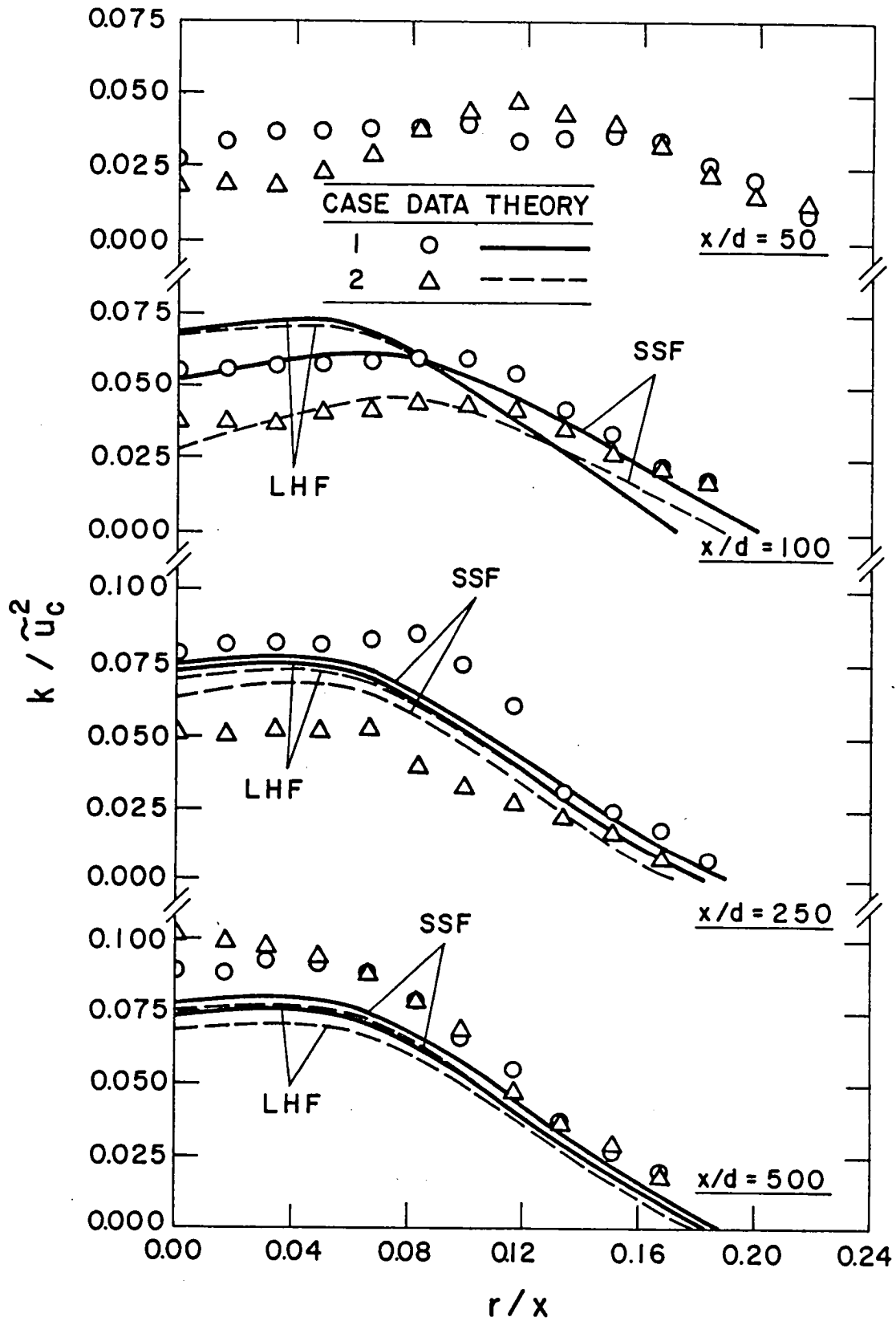
Figure 30.   Predicted and measured radial variation of turbulent
kinetic energy in the evaporating sprays.
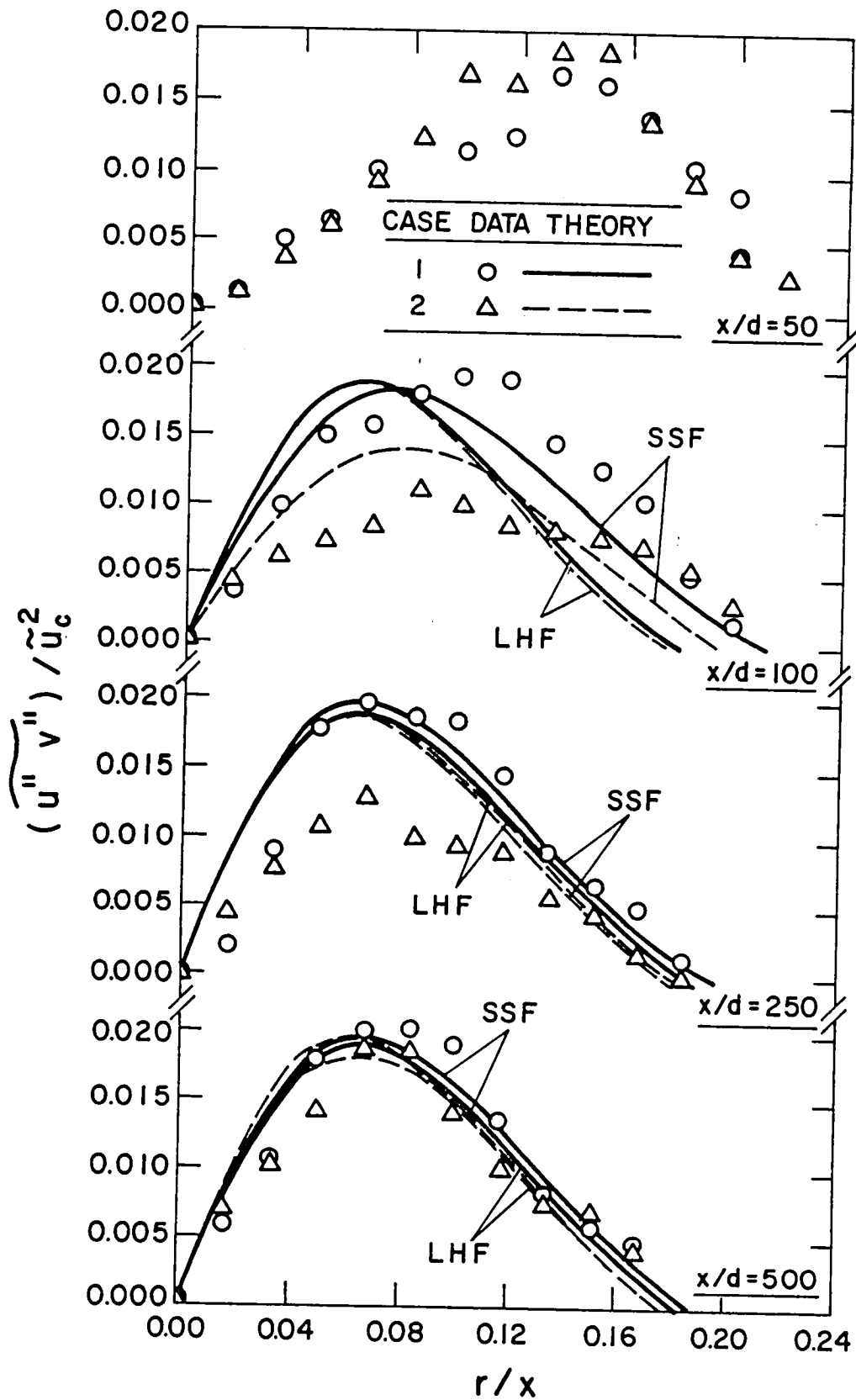
Figure 31. Predicted and measured radial variation of
Reynolds stress in the evaporating sprays.

64
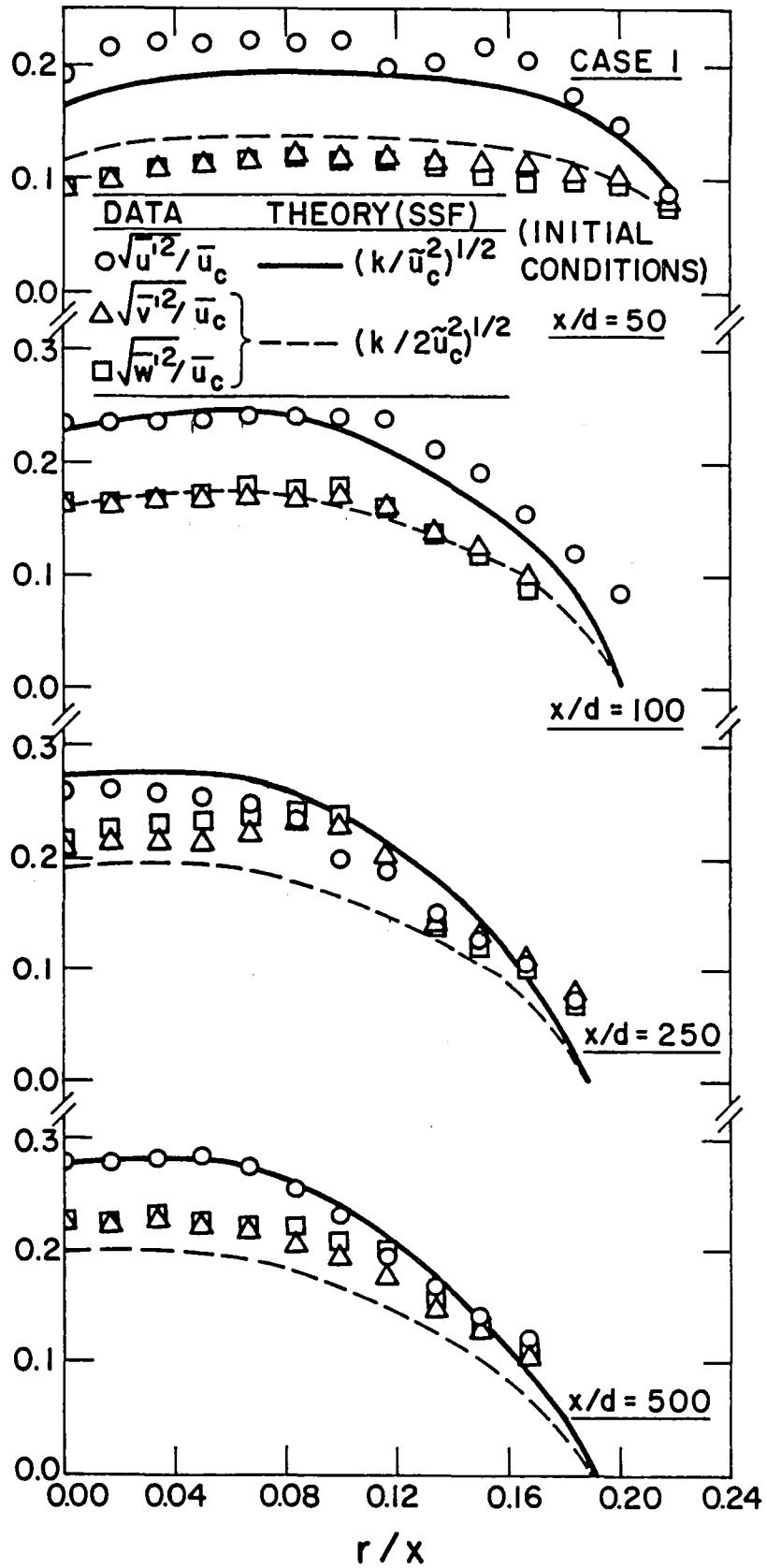
Figure 32. Predicted and measured radial variation of velocity
fluctuations for the case 1 evaporating spray.
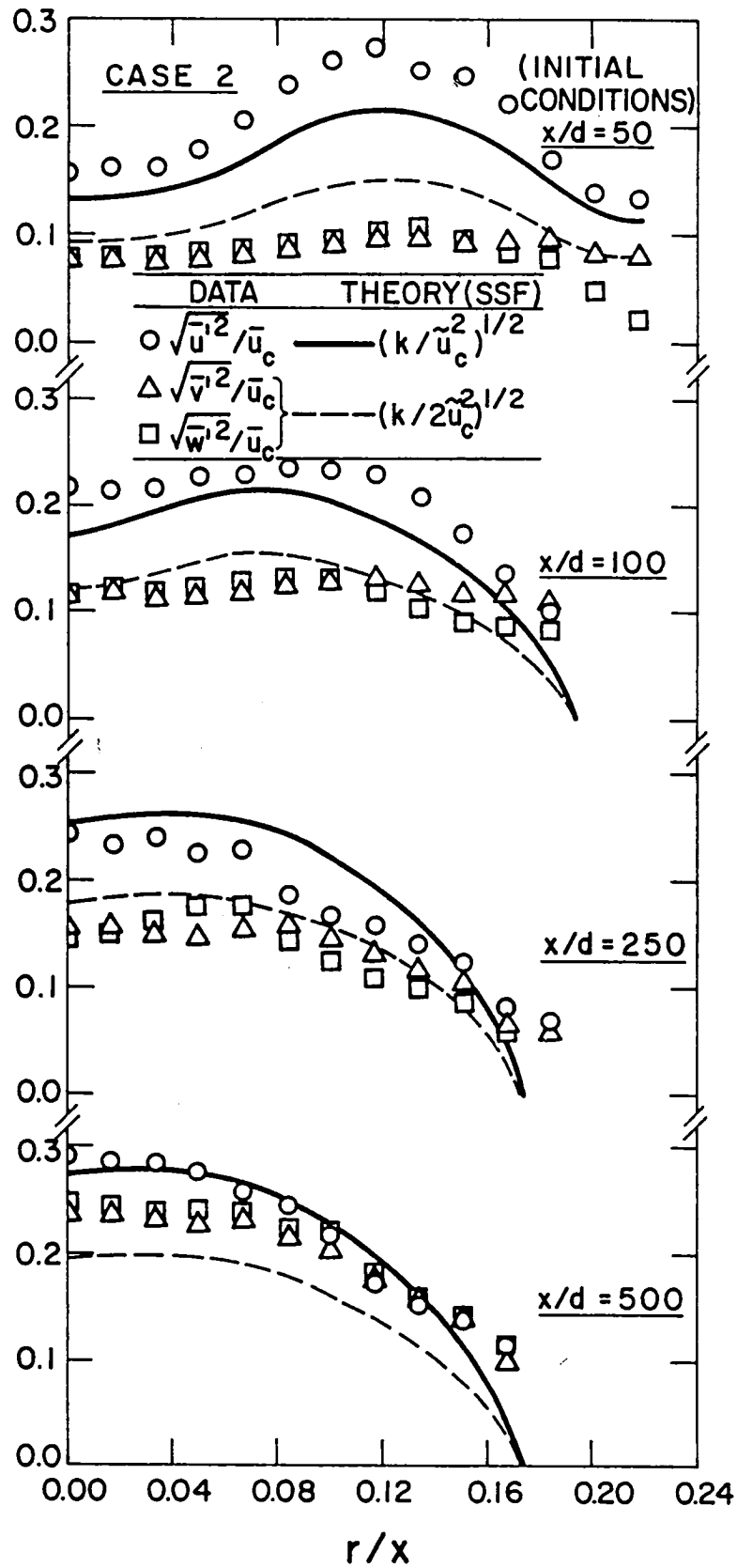
Figure 33. Predicted and measured radial variation of velocity
fluctuations for the case 2 evaporating spray.

observed in the nonevaporating sprays [10,11]. Predictions constructed
in this manner are in fair agreement with the measurements--
particularly in the region far from the injector. A notable feature of
the results, however, is that levels of anisotropy are rather high for
positions near the injector and generally exceed levels observed for
comparable values of x/d in single-phase jets [68,69]. Since this
region abuts the dense-spray portion of the flow, it seems likely that
the presence of drops are responsible for the higher degree of
anisotropy since effects of slip are preferentially transmitted into
the streamwise velocity component. High levels of anisotropy are also
of concern regarding the prescription of eddy properties in the present
SSF model, since this approach is based on the assumption of isotropic
turbulence. This suggests that multistress models of particle-laden
flows might profitably be examined in order to gain more insight
concerning effects of particles on turbulence properties.

4.6 Sensitivity Study

Early in the preceding discussion, it was noted that
specification of initial conditions is of vital importance to
predictions using separated flow models. In the present study, care
was exercised in obtaining well-defined initial conditions of all
necessary flow properties, at a position as close as possible to the
injector exit, viz. x/d = 50. However, while measurements of initial
conditions of gas-phase mean and turbulence properties were considered
sufficiently accurate, initial conditions of mean and fluctuating axial
and radial drop velocities were estimated to contain uncertainties that
could be beyond acceptable limits of experimental error.

Uncertainties exist in the measurements of mean and fluctuating
axial drop velocities due to the grouping of data into finite diameter
size-ranges and the use of insufficient sample sizes, especially for
the larger drops in the size distribution. Initial conditions of mean
and fluctuating radial drop velocities are also of concern. These drop
properties were not measured but were estimated from the measured
values of the corresponding axial drop velocities and the spray angles.

Due to these uncertainties regarding measurements of initial
conditions of drop properties, the sensitivity of the SSF model
predictions to the variation of these parameters was examined. The
results of this study are presented in Tables 5-7 and Tables 8-10 for
the case 1 and case 2 evaporating sprays. The entries show the
fractional change in the predicted variable caused by increasing the
input variable (at x/d = 50) by 25%--with all other variables
unchanged.

In general, gas-phase properties and SMD are relatively
insensitive to changes in the input variables. The total Freon-11 (gas
and liquid) concentration $\bar{Y}_F$, is also relatively insensitive since
Freon-11 vapor dominates in the predictions for the present test
conditions. The most sensitive variable is the liquid mass
flux--particularly for changes in mean and radial drop velocities.
Next in importance are mean axial drop velocities, which are mostly
sensitive to their own initial conditions. These effects are more

Table 5. Summary of Results of Sensitivity Study for the Case 1 Evaporating Spray at $x/d = 100$[a]

Output Variables	Input Variables			
	$\tilde{u}_p$	$(\widetilde{u_p''^2})^{1/2}$	$\tilde{v}_p$	$(\widetilde{v_p''^2})^{1/2}$
$\tilde{u}_c$	.03	-.00	-.00	-.00
$k_c/\tilde{u}_c^2$	-.02	-.00	-.00	-.00
$\tilde{Y}_{fc}$	-.00	-.00	-.03	.01
$\tilde{G}_c$	.16	-.01	-.10	.05
SMD_c	.02	-.01	.02	.01
$\tilde{u}_{p_c}$				
D_p (μm) = 17.5	.08	-.03	.04	.06
32.5	.14	.01	.02	-.02
52.5	.17	.02	-.00	-.00

[a]Entries show fractional change in predicted output variable by raising input variable at $x/d = 50$ by 25%.

Table 6.   Summary of Results of Sensitivity Study for the Case 1 Evaporating Spray at x/d = 250

Output Variables	Input Variables			
	$\tilde{u}_p$	$(\tilde{u}_p''^2)^{1/2}$	$\tilde{v}_p$	$(\tilde{v}_p''^2)^{1/2}$
$\tilde{u}_c$	.03	-.00	-.00	-.00
$k_c/\tilde{u}_c^2$	.02	-.00	-.01	-.00
$\tilde{Y}_{fc}$	-.02	-.02	-.04	-.02
$\tilde{G}_c$	.06	-.08	-.18	-.09
SMD_c	.02	-.00	-.04	-.00
$\tilde{u}_{p_c}$				
D_p (µm) = 17.5	-.03	-.01	-.10	-.04
32.5	.09	.04	.05	-.04
52.5	.05	-.00	-.02	-.00

Table 7. Summary of Results of Sensitivity Study for
the Case 1 Evaporating Spray at x/d = 500

Output Variables	Input Variables			
	$\tilde{u}_p$	$(\tilde{u}_p''^2)^{1/2}$	$\tilde{v}_p$	$(\tilde{v}_p''^2)^{1/2}$
$\tilde{u}_c$	.02	-.00	-.00	-.00
$k_c/\tilde{u}_c^2$	.01	-.00	-.00	-.00
$\tilde{Y}_{fc}$	-.03	-.00	.01	-.00
$\tilde{G}_c$	.45	-.02	-.10	.03
SMD_c	.03	-.01	.01	.02
$\tilde{u}_{p_c}$				
D_p (μm) = 17.5	-.10	-.18	-.00	-.05
32.5	-.02	-.05	-.03	-.03
52.5	--	--	--	--

Table 8. Summary of Results of Sensitivity Study for
the Case 2 Evaporating Spray at x/d = 100

Output Variables	Input Variables			
	$\bar{u}_p$	$(\widetilde{u''^2_p})^{1/2}$	$\bar{v}_p$	$(\widetilde{v''^2_p})^{1/2}$
$\tilde{u}_c$	.03	-.00	-.00	-.00
$k_c/\tilde{u}_c^2$	.03	-.00	-.01	-.00
$\tilde{Y}_{fc}$	.01	-.01	-.03	.03
$\tilde{G}_c$	.25	-.04	-.15	.13
SMD_c	-.01	-.01	-.01	-.02
$\tilde{u}_{p_c}$				
D_p (μm) = 15	.02	-.06	-.04	-.02
55	.15	-.00	.01	-.02
95	.20	.01	.01	.01

Table 9. Summary of Results of Sensitivity Study for
the Case 2 Evaporating Spray at x/d = 250

Output Variables	Input Variables			
	$\tilde{u}_p$	$(\tilde{u}_p''^2)^{1/2}$	$\tilde{v}_p$	$(\tilde{v}_p''^2)^{1/2}$
$\tilde{u}_c$	.04	-.00	-.01	-.00
$k_c/\tilde{u}_c^2$	.11	-.00	-.02	-.00
$\tilde{Y}_{fc}$	.03	-.01	-.07	-.00
$\tilde{G}_c$	.26	-.04	-.22	-.00
SMD_c	.01	-.00	-.04	.01
$\tilde{u}_{p_c}$				
D_p (μm) = 15	.06	-.00	.05	.02
55	.07	-.00	-.00	.01
95	.14	-.01	-.01	.01

Table 10.   Summary of Results of Sensitivity Study for the Case 2 Evaporating Spray at x/d = 500

Output Variables	Input Variables			
	$\tilde{u}_p$	$(\tilde{u}_p''^2)^{1/2}$	$\tilde{v}_p$	$(\tilde{v}_p''^2)^{1/2}$
$\tilde{u}_c$	.03	.00	.00	.00
$k_c/\tilde{u}_c^2$	.09	.00	-.02	-.00
$\tilde{Y}_{fc}$	.01	.01	-.02	.02
$\tilde{G}_c$	.21	.03	-.16	.07
SMD_c	-.04	-.03	-.04	-.02
$\tilde{u}_{p_c}$				
D_p (µm) = 15	.13	.07	.13	-.00
55	.04	.05	-.03	-.01
95	.09	-.01	-.00	-.00

important for the case 2 spray where a greater proportion of large drops, which tend to maintain the properties at the initial state due to their greater mass, exert a strong influence on flow properties. These findings are similar to the results obtained for the sensitivity study in the nonevaporating sprays [10,11].

5. SUMMARY AND CONCLUSIONS

5.1 Summary

Comprehensive measurements of the structure of fine and coarse evaporating sprays were completed to aid in the understanding of effects of drop size, coalescence, turbulence modulation and turbulent dispersion on spray properties. Sprays having nominal Sauter mean diameters of 31 and 58 microns were considered. These measurements included mean and fluctuating gas-phase velocities, liquid fluxes, drop-size distributions, mean and fluctuating axial drop velocities, mean concentration of injected fluid and mean gas-phase temperatures. Initial conditions of spray properties were measured at a location as close to the injector exit as possible, viz. $x/d = 50$, to provide appropriate initial conditions for separated flow models of spray processes. Uncertainties in proper average properties to determine drop transport were minimized by calibrating procedures using measurements of life histories of single drops supported in an air stream.

Measurements of the structure of the evaporating sprays were used to evaluate the predictions of three theoretical models, as follows: (1) a locally homogeneous flow (LHF) model, where slip between the phases is neglected; (2) a deterministic separated flow (DSF) model, where interphase slip is considered but turbulent dispersion of particles is neglected; and (3) a stochastic separated flow (SSF) model, where effects of interphase slip, turbulent dispersion and turbulent fluctuations are considered using random sampling for turbulence properties in conjunction with random-walk computations for drop motion.

The theoretical description of the continuous phase for all three models was based upon the Favre-averaged form of the conservation equations written in Eulerian coordinates. The dispersed phase was treated, for the separated flow models, by solving Lagrangian equations of motion for the particles. A modified version of the GENMIX program [26] combined with a second-order Runge-Kutta ordinary differential equation solver for drop motion were used to solve the governing equations.

A sensitivity study was conducted to investigate the influence of uncertainties in specification of initial conditions of drop properties on model predictions. The results are useful in identifying potential sources of error for both predictions and measurements.

5.2 Conclusions

The major conclusions and observations of this study are as follows:

1. The present measurements in nonevaporating sprays showed significant effects of slip between the gas and liquid phases. The rate of development of the coarser spray, having a higher loading ratio, was slower than that of the more finely atomized spray with a lower loading ratio. Present measurements were limited to the dilute portion of the flows, where void fractions were greater than 99.1%. In this region, drop coalescence and major effects of drops on turbulence properties were not observed. As the dense flow region was approached, however, gas-phase turbulent velocity fluctuations exhibited increased anisotropy--suggesting a significant modification of turbulence properties by drops. Additional measurements in the dense spray region would be required to confirm these effects. Turbulent dispersion of drops was observed as a significant phenomena in both sprays; yielding spray widths that were generally larger than most fully-developed, single-phase jets. Effects of dispersion were smaller than observed for nonevaporating sprays [10-11], due to decreasing mass of the dispersed phase by evaporation. Counteracting effects of turbulent dispersion and evaporation also caused the SMD to remain relatively uniform along the centerline of the sprays.

2. The LHF model generally overestimated the rate of flow development of the sprays, similar to past experience with this model [15-17]. However, the LHF model underestimated flow widths--unlike the results of earlier work in particle-laden jets [7,8]. Such enhanced turbulent dispersion of drops, for certain ranges of turbulence and drop properties, is often observed in multiphase flows. The effect was more evident for the present sprays than for the particle-laden jets due to the smaller density of the liquid, which allowed the drops to respond more readily to turbulent fluctuations; and greater initial slip and rates of deceleration in the sprays; due to smaller injector dimensions. Due to the possibility of preferential dispersion under some conditions, it may be concluded that the LHF model does not always provide an upper bound on the rate of development of sprays, as

suggested in the past [1]. In spite of these shortcomings, it is felt that the LHF model is still useful as a design tool, since it provides a reasonable first estimate of spray properties with much reduced requirements for defining initial conditions than separated flow models.

3. Differences between measurements and predictions of the DSF and LHF models were smaller than observed for nonevaporating sprays [10-11], since decreasing mass of the dispersed phase by evaporation causes the flow to approach a single-phase flow, where all models considered here are identical. The DSF model generally underestimated drop dispersion for the present measurements. This approach appears to have limited utility for modeling practical two-phase flows. Gosman and Ioannides [22] note, however, that uncertainties in initial conditions for multiphase flows are potentially a greater source of error than neglecting particle dispersion.

4. In contrast, the SSF model yielded reasonably good results for the present measurements. The SSF model also provided adequate treatment of enhanced drop dispersion in the sprays with no modification of the model from its original calibration (where effects of enhanced dispersion were not observed). While this is encouraging, additional evaluation of the model is needed-- particularly considering improved specifications of initial conditions. Predictions of the SSF model showed greatest errors for axial drop velocities in the near-injector region; however, sensitivity analysis showed that this property is strongly influenced by specification of initial drop velocities, where experimental uncertainties are greatest.

The SSF model, which employs assumptions of isotropy performed reasonably well in spite of effects of anisotropy exhibited by measurements near the dense regions of the sprays. However, further consideration of effects of anisotropy, perhaps using a multistress turbulence model, would be desirable. The SSF approach, however, appears to provide an attractive formulation for treating nonlinear interphase transport processes in drop-laden turbulent flows.

5. In general, present model predictions are relatively insensitive to the specification of gas-phase initial conditions. The specification of drop properties, however, exerts much more pronounced effects on predictions. This emphasizes the importance of measurements of initial condition of drop properties in order to obtain a convincing evaluation of separated flow models.

Potential problems in obtaining reliable initial conditions include difficulties in carrying out measurements in the dense spray regions and lack of understanding of the atomization process in sprays.

REFERENCES

1. Faeth G. M., "Evaporation and Combustion of Sprays," Prog. in Energy and Combust. Sci., Vol. 9, 1983, pp. 1-76.

2. Faeth, G. M., "Recent Advances in Modeling Particle Transport Properties and Dispersion in Turbulent Flow," Proceedings of the ASME-JSME Thermal Engineering Conference, Vol. 2, ASME, New York City, 1983, pp. 517-534.

3. Shuen, J-S., Chen, L-D. and Faeth, G. M., "Evaluation of a Stochastic Model of Particle Dispersion in a Turbulent Round Jet," AIChE J., Vol. 29, 1983, pp. 167-170.

4. Shuen, J-S., Chen, L-D. and Faeth, G. M., "Predictions of the Structure of Turbulent Particle-Laden Jets," AIAA J., Vol. 21, 1983, pp. 1483-1484.

5. Shuen, J-S., Chen, L-D. and Faeth, G. M., "Predictions of the Structure of Turbulent, Particle-Laden, Round Jets," AIAA Paper No. 83-0066.

6. Shuen, J-S., Solomon, A.S.P., Zhang, Q-F. and Faeth, G. M., "The Structure of Particle-Laden Jets and Nonevaporating Sprays," NASA CR-168059, 1983.

7. Shuen, J-S., Solomon, A.S.P., Zhang, Q-F. and Faeth, G. M., "A Theoretical and Experimental Study of Turbulent Particle-Laden Jets," NASA CR-168293, 1983.

8. Shuen, J-S., Solomon, A.S.P., Zhang, Q-F. and Faeth, G. M., "Structure of Particle-Laden Jets: Measurements and Predictions," AIAA Paper No. 84-0038, 1984.

9. Solomon, A.S.P., Shuen, J-S., Zhang, Q-F. and Faeth, G. M., "Measurements and Predictions for Nonevaporating Sprays in a Quiescent Environment," AIAA Paper No. 83-0151.

10. Solomon, A.S.P., Shuen, J-S., Zhang, Q-F. and Faeth, G. M., "Structure of Nonevaporating Sprays: Measurements and Predictions," AIAA Paper No. 84-0125, 1984.

11. Solomon, A.S.P., Shuen, J-S., Zhang, Q-F. and Faeth, G. M., "A Theoretical and Experimental Study of Turbulent Nonevaporating Sprays," NASA Contractor Report, 1984.

12. Yule, A. J., Ah Seng, C., Felton, P. G., Ungut, A. and Chigier, N. A., "A Study of Vaporizing Sprays by Laser Techniques," Combustion and Flame, Vol. 44, 1982, pp. 71-84.

13. Tishkoff, J. M., Hammond, D. C., Jr. and Chraplyvy, A. R., "Diagnostic Measurements of Fuel Spray Dispersion," J. Fluids Engr., Vol. 104, pp. 313-317, 1982.

14. Tishkoff, J. M., "Measurements of Particle Size and Velocity in a Fuel Spray," paper presented at the Second International Conference on Liquid Atomization and Spray Systems, Madison, WI, June 20-24, 1982.

15. Shearer, A. J., Tamura, H. and Faeth, G. M., "Evaluation of a Locally Homogeneous Flow Model of Spray Evaporation," J. of Energy, Vol. 3, September-October 1979, pp. 271-278.

16. Mao, C-P., Szekely, G. A., Jr. and Faeth, G. M., "Evaluation of a Locally Homogeneous Flow Model of Spray Combustion," J. of Energy, Vol. 4, March-April 1980, pp. 78-87.

17. Mao, C-P., Wakamatsu, Y. and Faeth, G. M., "A Simplified Model of High Pressure Spray Combustion," Eighteenth Symposium (International) on Combustion, The Combustion Institute, Pittsburgh, 1981, pp. 337-347.

18. El Banhawy, Y. and Whitelaw, J. H., "Calculation of the Flow Properties of a Confined Kerosene-Spray Flame," AIAA J., Vol. 18, December 1980, pp. 1503-1510.

19. Mongia, H. C. and Smith, K., "An Empirical/Analytical Design Methodology for Gas Turbine Combustors," AIAA Paper No. 78-998, 1978.

20. Boyson, F. and Swithenbank, J., "Spray Evaporation in Recirculating Flow," Seventeenth Symposium (International) on Combustion, The Combustion Institute, Pittsburgh, 1979, pp. 443-453.

21. Yuu, S., Yasukouchi, N., Hirosawa, Y. and Jotaki, T., "Particle Turbulent Diffusion in a Dust Laden Round Jet," AIChE J., Vol. 24, 1978, pp. 509-519.

22. Gosman, A. D. and Ioannides, E., "Aspects of Computer Simulation of Liquid-Fueled Combustors," AIAA Paper No. 81-0323, 1981.

23. Lockwood, F. C. and Naguib, A. S., "The Prediction of the Fluctuations in the Properties of Free, Round Jet, Turbulent, Diffusion Flames," Combustion and Flame, Vol. 24, 1975, pp. 109-124.

24. Bilger, R. W., "Turbulent Jet Diffusion Flames," Prog. Energy Combust. Sci., Vol. 1, pp. 87-109, 1976.

25. Jeng, S. M. and Faeth, G. M., "Species Concentrations and Turbulence Properties in Buoyant Methane Diffusion Flames," submitted to J. of Heat Transfer.

26. Spalding, D. B., GENMIX: A General Computer Program for Two-Dimensional Parabolic Phenomena, Pergamon Press, Oxford, 1978.

27. McCreath, C. G., Roett, M. F. and Chigier, N. A., "A Technique for Measurement of Velocities and Size of Particles in Flames," J. Physics E: Scientific Instruments, Vol. 5, pp. 601-604, 1972.

28. Al Tawell, A. M. and Landau, J., "Turbulence Modulation in Two-Phase Jets," Intl. J. Multiphase Flow, Vol. 3, pp. 341-351, 1977.

29. Wygnanski, I. and Fiedler, H., "Some Measurements in a Self Preserving Jet," Journal of Fluid Mechanics, Vol. 38, pp. 577-612, 1969.

30. Rodi, W., "The Prediction of Free Turbulent Boundary Layers by use of a 2-Equation Turbulence Model," Ph.D. Thesis, University of London, 1972; also cited in Launder, B. E. and Morse, A., "Numerical Prediction of Axisymmetric Free Shear Flows with a Reynolds Stress Closure," Turbulent Shear Flows I, (F. Durst et al., ed.), Springer-Verlag, Berlin, 1979, pp. 279-294.

31. Reid, R. C., Prausnitz, J. M. and Sherwood, T. K., The Properties of Gases and Liquids, 3rd Edition, McGraw-Hill, New York, 1977.

32. ASHRAE Thermodynamic Properties of Refrigerants, American Society of Heating, Refrigerating and Air-Conditioning Engineers, Inc., New York, 1969.

APPENDIX A

SUMMARY OF PROPERTIES OF THE SPRAY FLUIDS

A.1 Freon-11

$$M = 137.37 \text{ kg/kg mole}$$

$$Cp_g = 0.520 \text{ kJ/kg K}$$

$$Cp_f = 0.879 \text{ kJ/kg K}$$

$$h_{fg} = 181.32 \text{ kJ/kg (at } T_o = 298 \text{ K)}$$

$$\rho_f = 2143.7 - 2.235 \text{ T kg/m}^3 \text{ (T in K)}$$

$$\log_{10} P_g = A' - B'/T \text{ kPa (T in k)}$$

$$A' = 6.7828$$

$$B' = 1416.1$$

A.2 Air

$$M = 28.97 \text{ kg/kg mole}$$

$$Cp = 1.005 \text{ kJ/kg K}$$

A.3 Evaluation of Mixing Rules for Gaseous Mixture

A.3.1 Thermal Conductivity

The thermal conductivity of the gaseous mixture was calculated with the Mason and Saxena formulation of the Wassiljewa Equation [31].

$$\lambda_m = \sum_{i=1}^{N} \left[\frac{x_i \lambda_i}{\sum_{j=1}^{N} x_j \phi_{ij}} \right] \tag{A.1}$$

where,

$$\phi_{ij} = \frac{1}{8^{1/2}} \left(1 + \frac{M_i}{M_j}\right)^{-1/2} \left[1 + \left(\frac{\mu_i}{\mu_j}\right)^{1/2} \left(\frac{M_j}{M_i}\right)^{1/4}\right]^2 \qquad \text{(A.2)}$$

with $\phi_{ij} = 1$ when $i = j$

A.3.2 <u>Viscosity</u>

The mixture viscosity calculations employed the method of Wilke as described in Reference [31].

For a mixture of N components

$$\mu_m = \sum_{i=1}^{N} \left[\frac{x_i \, \mu_i}{\sum_{j=1}^{N} x_j \, \phi_{ij}}\right] \qquad \text{(A.3)}$$

where ϕ_{ij} is given by Equation (A.2).

The Freon-11 vapor thermal conductivity and viscosity were obtained from Reference [32].

APPENDIX B

STATE RELATIONSHIPS FOR
LHF PREDICTIONS OF THE EVAPORATING SPRAYS

The relationship between mixture enthalpy, composition, temperature and density and the mixture fraction is provided by the state relationship. The experimental results to be compared with the analysis were all obtained at relatively low pressures; therefore, all gases are assumed to be ideal gases. Since combustion is not treated, chemical reaction is ignored. Finally, it should be recalled that the mixing process is adiabatic and occurs at constant pressure, under the assumptions of the present analysis.

Considering N species in the flow, the expression for the composition of the mixture is:

$$Y_i = Y_{io} \, f + Y_{i\infty} \, (1 - f) \quad , \quad i=1, \ldots N \tag{B.1}$$

where each species may exist in both the gaseous or liquid state

$$Y_i = Y_{fi} + Y_{gi} \tag{B.2}$$

The total enthalpy of the flow during the mixing process can be expressed as

$$h = h_o \, f + h_\infty \, (1-f) \tag{B.3}$$

where at any condition

$$h = \sum_N (Y_{fi} \, h_{fi} + Y_{gi} \, h_{gi}) \quad , \quad i=1, \ldots N \tag{B.4}$$

The density of the mixture is given by

$$\rho = \left[\sum_N (Y_{fi} \, v_{fi} + Y_{gi} \, v_{gi}) \right]^{-1} \quad , \quad i = 1, \ldots N \tag{B.5}$$

where v_{fi} and v_{gi} are the partial specific volumes of species i in the liquid and gas phases.

Given the relationships between enthalpy and density of each species and the composition, temperature and pressure, Equations (B.1)-(B.5) are sufficient to describe the composition, temperature and density of the mixture. The relative composition of the gas and liquid phases is obtained from Equation (B.2) and the requirement that the chemical potential of each species must be the same in both phases.

For the present test conditions, both air and Freon-11 liquid and vapor leave the injector exit, while the surroundings contain no Freon-11. Properties of the spray fluids used in the present calculations are summarized in Appendix A. Figure 34 shows the state relationship for the case 2 evaporating spray. The total mass fractions of air and Freon-11 are linear. The presence of liquid causes the mixture temperature to vary more slowly than in the region where only gases are present, due to heat of vaporization requirements. The mass fraction of Freon-11 vapor reaches a maximum at the point where the liquid disappears.

The state relationship for the case 1 evaporating spray can be obtained from the case 2 results, by shifting the abscissa of Figure 34 by the ratio of the initial Freon-11 mass fractions, $(Y_{Fo})_{case\ 1}/(Y_{Fo})_{case\ 2} = 0.941$. The results are shown in Figure 35.
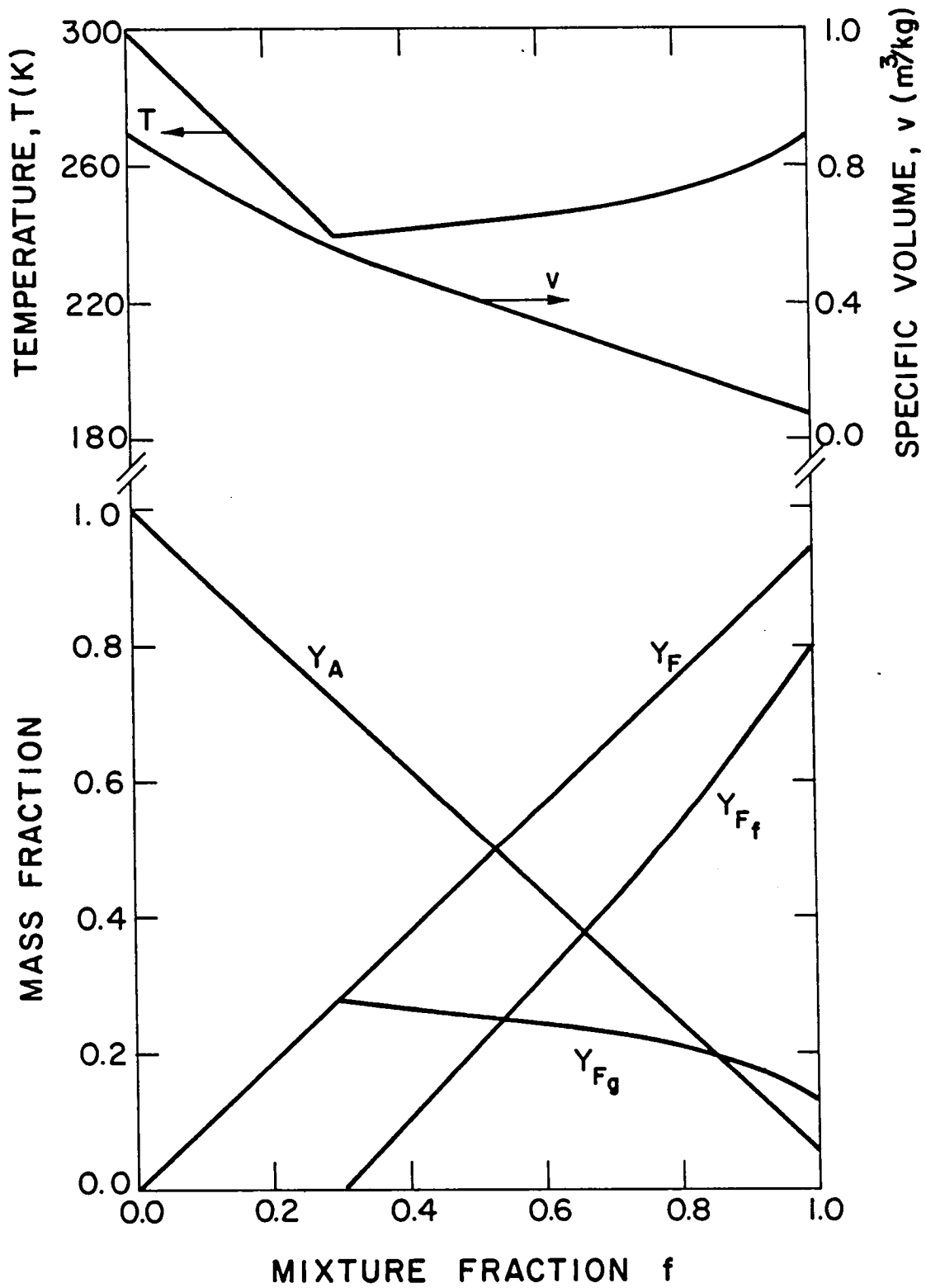
Figure 34. State relationship for the case 2
evaporating Freon-11 spray (LHF model).
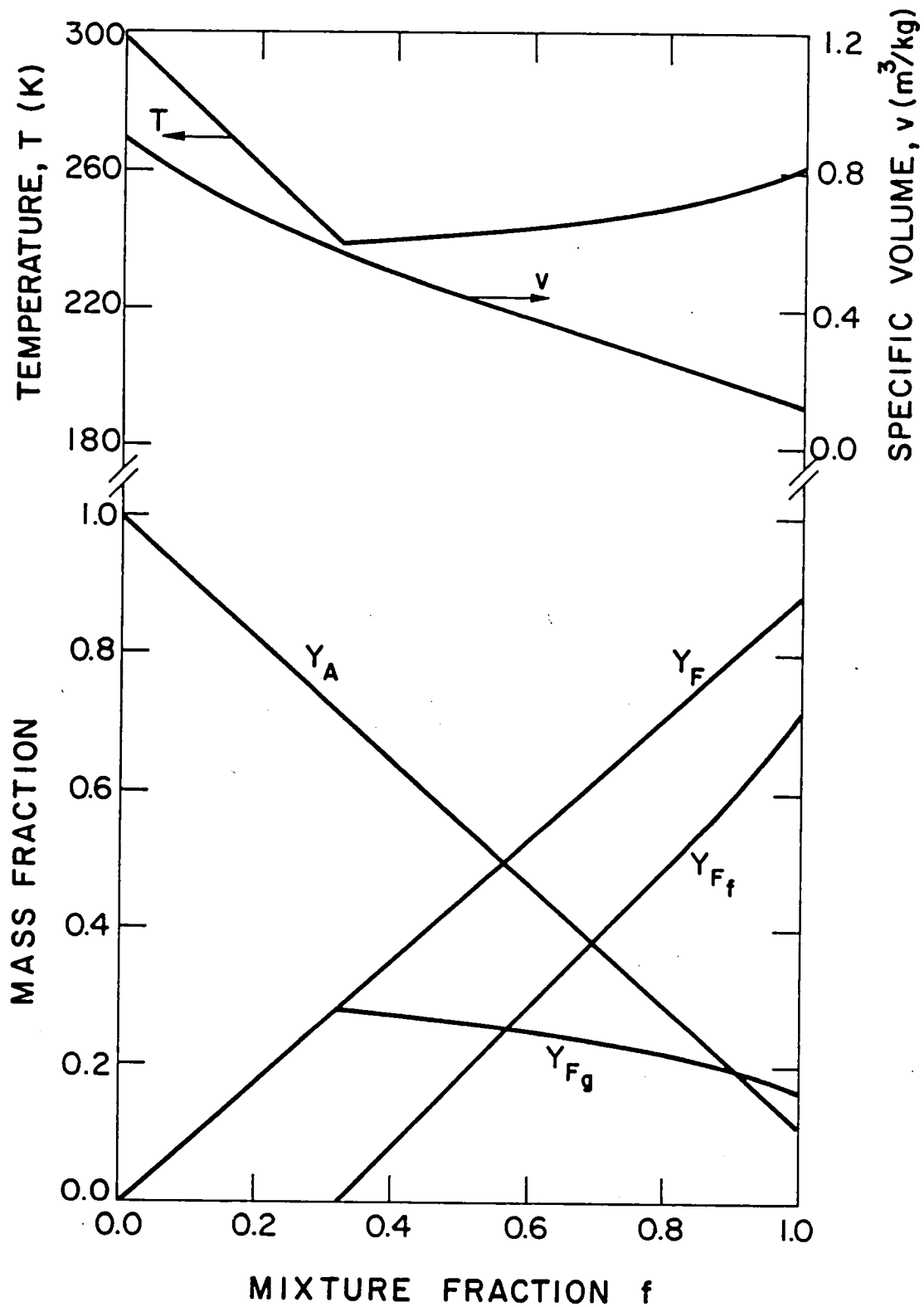
Figure 35. State relationship for the case 1
evaporating Freon-11 spray (LHF model).

APPENDIX C

DROPLET LIFE HISTORY CALIBRATION TESTS

C.1 Calibration Apparatus

The purpose of the calibration tests was to establish the proper reference condition to evaluate the fluid properties in Equations (2.13)-(2.21), as defined by Equation (2.24). The calibration experiment provided a well-defined test condition to evaluate the drop evaporation model, by providing a convective environment for the observation of a stationary evaporating drop.

A schematic of the overall experimental apparatus is shown in Figure 36. Motion pictures of the droplet evaporation process were taken to record the variation of droplet size with time. The droplet was suspended on a quartz probe of diameter approximately 150 μm. A pitot-static velocity probe was used to measure the velocity of the surrounding gas. The probe was connected to a Meriam model 34FB2 micromanometer in order to measure the difference between the static and stagnation pressure.

Turbulent air flow at the exit of a pipe provided the convective flow field for the droplet evaporation process. Fully-developed turbulent pipe flow was obtained from a pipe 32 mm in diameter and 610 mm in length. Four 16-mesh screens were placed near the pipe inlet to assist in developing the flow. Oil-free, dry air was supplied by a compressor. The air flow was controlled by a Matheson model 4 regulator and metered with a calibrated critical-flow orifice.

A Photosonic 1-B motion picture camera driven with a Kepco SM 36-5 AM d.c. power supply was used to record the variation of droplet size with time. The film speed was indicated by a timing light on the camera activated by an Adtrol Electronics pulse generator, model 501. Kodak Plus-X reversal film was used for all the tests. Backlighting for the photographic measurements was supplied by a conventional, 75 watt tungsten bulb. A diffuser screen was employed to obtain equal background intensity from the bulb.

Separate measurements of the drop temperature variation with time were made in order to estimate the wet-bulb temperature of the evaporation process. For these tests, the drop was suspended on the junction of a fine-wire thermocouple. The thermocouple was made from 0.076 μm chromel-alumel wire with a bead diameter of 0.2 mm. The reference junction was placed in an ice bath. A Hewlett-Packard X-Y plotter, model 7044A, was used to record the droplet temperature variation with time.

The temperature trace consisted of three regions; first a region of rapidly decreasing temperature; second, a constant temperature region; and third, a region where the temperature increases back to the
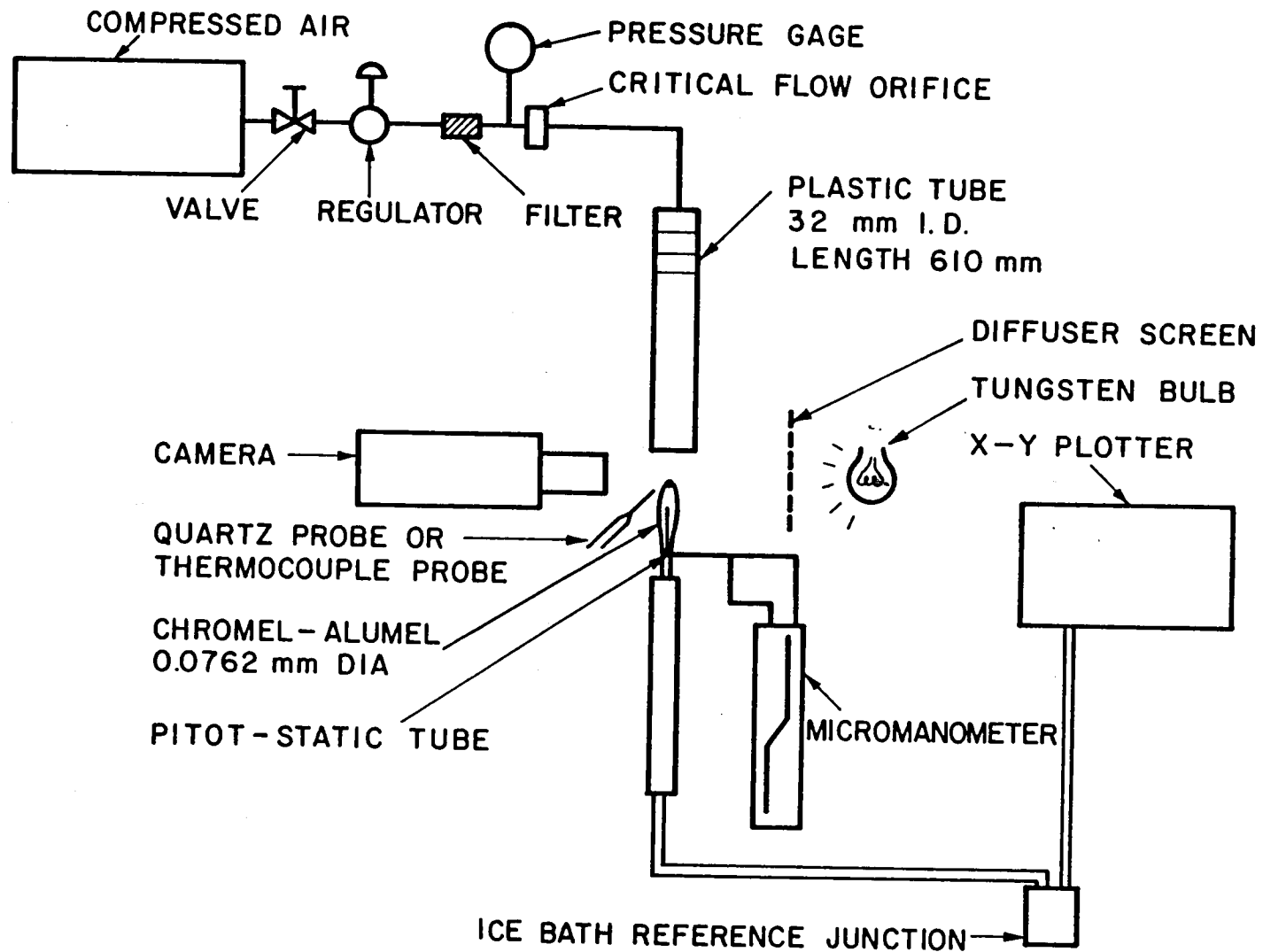
Figure 36. Schematic diagram of the drop life history calibration apparatus.

88

ambient gas temperature. The constant temperature is the wet-bulb temperature for the evaporation process. At this condition, all of the energy transferred to the drop is used to vaporize the liquid.

The analysis of the droplet size variation with time from the motion pictures was confined to the constant temperature region, by disregarding frames for an initial time period estimated from the droplet temperature tests. The films were analyzed using a Vanguard motion picture analyzer to view the film and measure the size of the droplet in each frame.

C.2 Theoretical Model of Droplet Life History Calibration Tests

The measurements of the life history of a stationary droplet in a well-defined environment were used to calibrate the drop evaporation model given by Equations (2.17)-(2.21). In this manner, errors in the drop life history calculations for the separated flow models (due to uncertainties in selecting proper average properties for transport parameters) were minimized.

All the assumptions outlined in Section 2.3.1, apply in the calculations for the calibration tests. Since the droplet is stationary, the drop momentum Equations (2.12)-(2.14) are not required. The governing equations are given by Equations (2.16)-(2.21) and (2.15) with only minor modification. Equation (2.16) is transformed to a function of time by noting that

$$u_p \frac{d}{dx} = \frac{d}{dt} \tag{C.1}$$

The ambient velocity, concentration and temperature are constant with time. Equations (2.16)-(2.21) are sufficient to solve for the surface temperature and diameter of the droplet as a function of time. Equation (2.16) is integrated numerically, where $\dot{m}''$ is given by a simultaneous solution of Equations (2.17) and (2.18). Average properties were computed at a mean state defined by Equation (2.26). The mixing rules employed are summarized in Appendix A.

C.3 Calibration Test Results

Several test conditions were considered with ambient velocities from 3 m/sec to 6 m/sec. This velocity range was selected so that the drop Reynolds numbers in the calibration experiment spanned the range encountered in the evaporating spray experiments.

The theoretical and experimental results for the variation of droplet size were examined. The closest agreement between predictions and measurements was achieved when a value of $\alpha = 0.75$ was used in Equation (2.24) to compute average gas-phase properties. Figure 37 is an illustration of some typical theoretical and experimental results. The drop diameter variation is plotted as a function of time for two different gas velocities. The agreement between predictions and
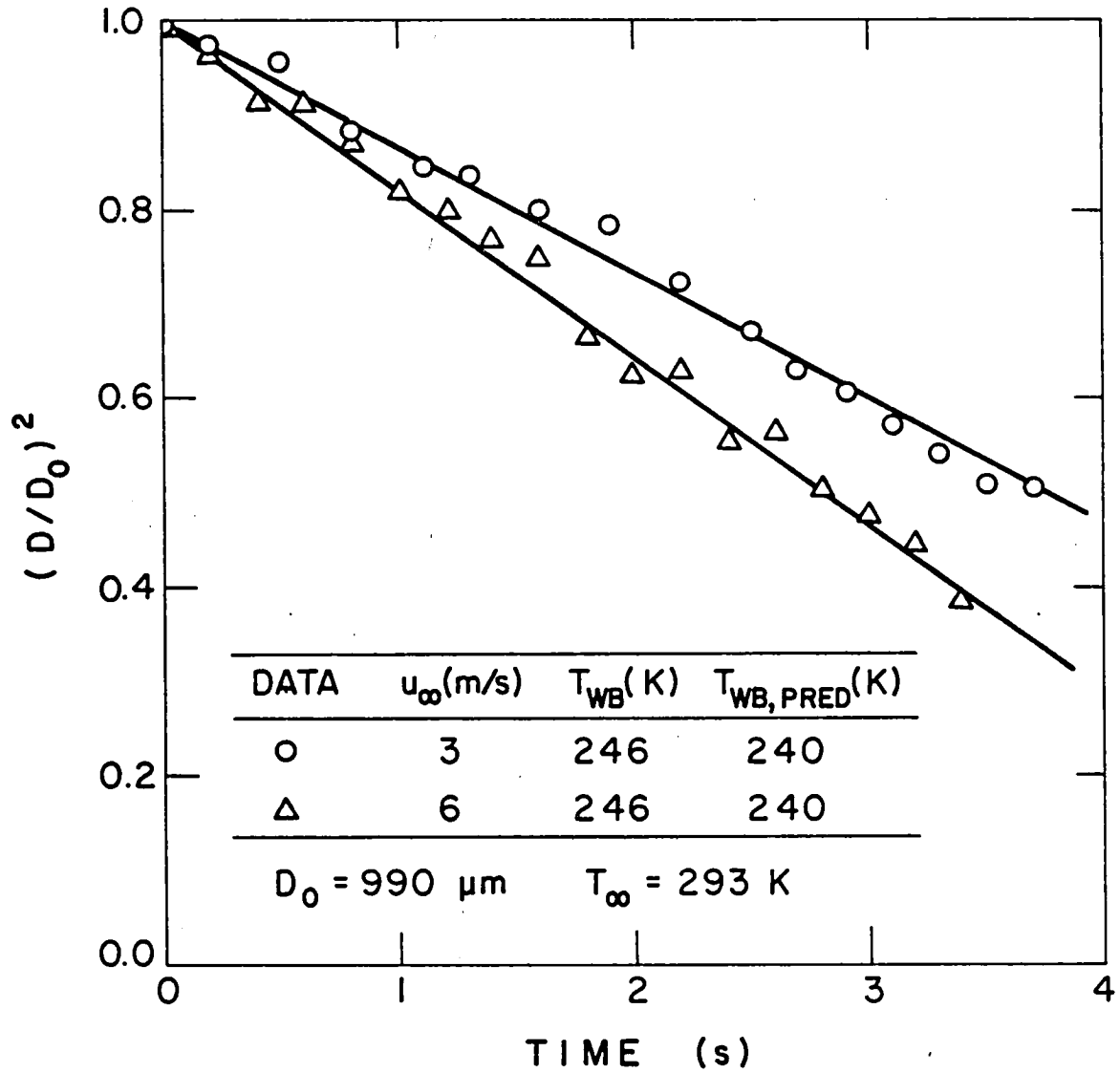
Figure 37. Drop life history calibration results.

measurements, with $\alpha = 0.75$, is seen to be quite good. The wet-bulb temperature of the drop is not a strong function of drop size or velocity. The predicted value is within $5^{\circ}C$ of the measured value, which is satisfactory for present purposes.

Based on the results of the calibration experiments, a value of $\alpha = 0.75$ was employed in Equation (2.24) to compute average gas-phase properties. No universality of this reference condition should be implied. The uncertainties in average properties and the transport correlations are such that calibration should be undertaken for each system to be investigated [1].

APPENDIX D

INITIAL CONDITIONS OF MEAN GAS-PHASE FREON-11 MASS FRACTION ($\tilde{Y}_{Fg}$)
AND SQUARE OF MASS FRACTION FLUCTUATIONS (g_{Fg}) AT x/d = 50
FOR THE SF MODEL PREDICTIONS OF THE EVAPORATING SPRAYS

Profiles of mean gas-phase Freon-11 mass fraction, $\tilde{Y}_{Fg}$, were needed at x/d = 50 to initiate both DSF and SSF model calculations for the case 1 and case 2 evaporating sprays. This information was deduced from measurements, at x/d = 50, of liquid flux (using slide impaction), mean axial drop velocities (using double-flash photography), and total Freon-11 concentrations (using isokinetic sampling and gas-chromatography). In the following, the analysis and assumptions used to compute $\tilde{Y}_{Fg}$ at x/d = 50 is outlined.

Freon-11 liquid, vapor and air exist in the two-phase mixture, so that conservation of species implies

$$Y_F + Y_a = 1 \tag{D.1}$$

where,

$$Y_F = Y'_{Ff} + Y'_{Fg} \tag{D.2}$$

The density of the mixture is given by

$$\rho = (Y'_{Ff}/\rho_f + Y'_{Fg}/\rho_g + Y_a/\rho_a)^{-1} \tag{D.3}$$

Let the drop concentration in a unit volume in the flow be denoted by C_f, then

$$C_f = \rho\, Y'_{Ff} \tag{D.4}$$

and the mass fraction of total Freon-11 (liquid + vapor) is given by

$$Y_F = \frac{C_f + \rho\, Y'_{Fg}}{\rho} \tag{D.5}$$

The quantity C_f can be computed from the liquid flux, $\tilde{G}_{fi}$, and the velocity, u_{pi}, of each drop size group i at a given radial location at x/d = 50 as follows:

$$C_f = \sum_{i=1}^{N} (\tilde{G}_{fi}/\tilde{u}_{pi}) \tag{D.6}$$

$\tilde{G}_{fi}$ is known from slide impaction measurements, cf., Section 3.3.2.3 while $\tilde{u}_{pi}$ is known from the drop velocity measurements, cf., Section 3.3.2.2.

A direct measurement of Y_F in Equation (D.4) is obtained from isokinetic sampling and gas-chromatography measurements of total concentration of injected Freon-11 described in Section 3.3.3.1.

It now remains to specify the temperature of the mixture so that the densities of each of the species can be calculated. This part of the analysis parallels that used for the equation of state computations for the SF models described in Section 2.3.2.2. The temperature of the drops is assumed to remain constant at the injected state, while an adiabatic mixing process is assumed for the gas phase. Therefore, assuming ideal gas behavior, the energy balance is given by Equation (2.31) as follows:

$$Y'_{Fg} \left(h_{fgo} + C_{pg} (T_o - T) \right) + Y_a C_{pa} (T_o - T) = 0 \qquad (D.7)$$

The densities of Freon-11 vapor and air can be found, using the ideal gas law, at the total pressure of the mixture

$$\rho_g = p \, M_g / R_o \, T \qquad (D.8)$$

$$\rho_a = p \, M_a / R_o \, T \qquad (D.9)$$

Equations (D.1)-(D.3), (D.5) and (D.7) provide five equations for the five unknowns Y'_{Fg}, Y'_{Ff}, Y_a, ρ and T. The mass fraction of Freon-11 vapor in the gas-phase is then computed from

$$\tilde{Y}_{Fg} = \frac{Y'_{Fg}}{Y'_{Fg} + Y_a} \qquad (D.10)$$

Table D.1 lists $\tilde{Y}_{Fg}$ as a function of radial location at $x/d = 50$ for the case 1 and case 2 evaporating sprays.

Profiles of the square of Freon-11 vapor mass fluctuations, g_{Fg}, were also needed at $x/d = 50$ to initiate SF model predictions for the evaporating sprays. A direct or indirect measurement of this quantity was not made; therefore, an estimate of the fluctuation intensity $(g_{Fg})^{1/2}/(\tilde{Y}_{Fg})_c$ was made from $(g)^{1/2}/\tilde{f}_c$ predictions at $x/d = 50$ of the LHF model. These values are listed in Table D.2 for the case 1 and case 2 evaporating sprays.

Table D.1. Initial Conditions of Mean Gas-Phase
Freon-11 Mass Fraction at x/d = 50 for
the Case 1 and Case 2 Evaporating Sprays

	$\tilde{Y}_{Fg}$	
r/x	Case 1	Case 2
0.00	0.306	0.447
0.05	0.251	0.352
0.10	0.134	0.238
0.15	0.013	0.126
0.20	0.019	0.000

Table D.2. Initial Conditions of Gas-Phase Freon-11
Mass Fraction Fluctuations at x/d = 50 for
the Case 1 and Case 2 Evaporating Sprays

	$G_{Fg}/(g_{Fg})_c$	
	Case 1	Case 2
r/x	$(g_{Fg})_c^{1/2}/(\tilde{Y}_{Fg})_c = 0.209$	$(g_{Fg})_c^{1/2}/(\tilde{Y}_{Fg})_c = 0.210$
0.000	1.00	1.00
0.007	1.02	1.01
0.014	1.05	1.04
0.021	1.09	1.10
0.028	1.15	1.16
0.035	1.22	1.23
0.042	1.28	1.31
0.049	1.34	1.36
0.056	1.38	1.40
0.063	1.42	1.43
0.070	1.45	1.44
0.077	1.45	1.43
0.084	1.43	1.41
0.091	1.40	1.37
0.099	1.35	1.31
0.106	1.29	1.23
0.113	1.22	1.14
0.120	1.12	1.03
0.127	1.00	0.90
0.134	0.88	0.76
0.141	0.67	0.61
0.148	0.45	0.46
0.155	0.22	0.30
0.162	0.12	0.00
0.169	0.10	0.00
0.176	0.06	0.00
0.183	0.00	0.00
0.190	0.00	0.00
0.197	0.00	0.00
0.204	0.00	0.00
0.211	0.00	0.00
0.218	0.00	0.00

APPENDIX E

DATA FOR THE EVAPORATING SPRAY (CASE 1)

E.1 Gas-Phase Properties

Table E.1.1. Axial Variation of Centerline Velocity

x/d	$\bar{u}_c/\bar{u}_o$
40	0.428
50	0.370
70	0.284
100	0.222
150	0.170
250	0.113
400	0.062
500	0.052

Table E.1.2.   Radial Variation of Quantities

x/d = 50

r/x	$\bar{u}/\bar{u}_c$	$\overline{u'v'}/\bar{u}_c^2$	$\sqrt{\overline{u'^2}}/\bar{u}_c$	$\sqrt{\overline{v'^2}}/\bar{u}_c$	$\sqrt{\overline{w'^2}}/\bar{u}_c$	$\bar{k}/\bar{u}_c^2$
0.0	1.0	0.0	0.193	0.095	0.094	.0276
0.0168	0.994	.00124	0.217	0.097	0.100	.0332
0.0335	0.996	.00505	0.221	0.110	0.111	.0366
0.0503	0.951	.00632	0.219	0.111	0.112	.0364
0.0670	0.895	.0105	0.221	0.114	0.117	.0373
0.0838	0.809	.01221	0.221	0.114	0.115	.0375
0.1005	0.725	.0116	0.223	0.118	0.114	.0383
0.1173	0.625	.01268	0.200	0.120	0.114	.0337
0.1340	0.555	.01692	0.204	0.120	0.110	.0341
0.1508	0.496	.0164	0.219	0.116	0.103	.0360
0.1675	0.406	.0139	0.206	0.115	0.098	.0326
0.1843	0.309	.0105	0.175	0.106	0.095	.0254
0.2010	0.216	.0087	0.150	0.101	0.094	.0208
0.218	0.095	.00258	0.084	0.075	0.079	.0095

Table E.1.3.   Radial Variation of Quantities

x/d = 100

r/x	$\bar{u}/\bar{u}_c$	$\overline{u'v'}/\bar{u}_c^2$	$\sqrt{\overline{u'^2}}/\bar{u}_c$	$\sqrt{\overline{v'^2}}/\bar{u}_c$	$\sqrt{\overline{w'^2}}/\bar{u}_c$	$\bar{k}/\bar{u}_c^2$
0.0	1.0	0.0	0.238	0.165	0.164	0.0554
0.0168	0.971	0.00356	0.237	0.166	0.162	0.0549
0.0335	0.940	0.0100	0.238	0.167	0.167	0.0562
0.0503	0.892	0.0146	0.238	0.166	0.173	0.0571
0.0670	0.858	0.0158	0.242	0.167	0.179	0.0592
0.0838	0.794	0.0181	0.242	0.168	0.180	0.0596
0.1005	0.690	0.0194	0.243	0.169	0.179	0.0598
0.1173	0.554	0.0193	0.239	0.161	0.159	0.0542
0.1340	0.463	0.0146	0.213	0.138	0.135	.0413
0.1508	0.377	0.0128	0.194	0.124	0.115	0.0331
0.1675	0.274	0.01026	0.156	0.096	0.088	0.0206
0.1843	0.135	0.0052	0.121	--	--	--
0.2010	0.091	0.00170	0.085	--	--	--

Table E.1.4.   Radial Variation of Quantities

$x/d = 250$

r/x	$\bar{u}/\bar{u}_c$	$\overline{u'v'}/\bar{u}_c^2$	$\sqrt{\overline{u'^2}}/\bar{u}_c$	$\sqrt{\overline{v'^2}}/\bar{u}_c$	$\sqrt{\overline{w'^2}}/\bar{u}_c$	$\bar{k}/\bar{u}_c^2$
0.0	1.0	0.0	0.257	0.209	0.215	0.0779
0.0168	0.993	0.00202	0.259	0.213	0.224	0.0813
0.0335	0.931	0.00897	0.256	0.215	0.228	0.0819
0.0503	0.797	0.01784	0.253	0.212	0.233	0.0816
0.0670	0.688	0.0197	0.247	0.222	0.237	0.0832
0.0838	0.561	0.01868	0.236	0.236	0.241	0.0847
0.1005	0.435	0.0185	0.199	0.229	0.238	0.0743
0.1173	0.357	0.0146	0.188	0.207	0.202	0.0595
0.1340	0.259	0.00894	0.151	0.139	0.139	0.0307
0.1508	0.186	0.00664	0.128	0.132	0.115	0.0235
0.1675	0.150	0.00497	0.110	0.110	0.100	0.0171
0.1843	0.078	0.00131	0.076	0.0757	0.070	0.0082

Table E.1.5.   Radial Variation of Quantities

x/d = 500

r/x	$\bar{u}/\bar{u}_c$	$\overline{u'v'}/\bar{u}_c^2$	$\sqrt{\overline{u'^2}}/\bar{u}_c$	$\sqrt{\overline{v'^2}}/\bar{u}_c$	$\sqrt{\overline{w'^2}}/\bar{u}_c$	$\bar{k}/\bar{u}_c^2$
0.0	1.0	0.0	0.279	0.221	0.223	0.0882
0.0168	0.968	0.00585	0.279	0.220	0.223	0.088
0.0335	0.875	0.0151	0.282	0.225	0.231	0.0918
0.0503	0.821	0.01797	0.286	0.221	0.230	0.0918
0.0670	0.763	0.0202	0.276	0.214	0.226	0.0865
0.0838	0.581	0.0202	0.254	0.204	0.219	0.0770
0.1005	0.501	0.0189	0.231	0.192	0.208	0.0667
0.1173	0.406	0.0136	0.193	0.178	0.199	0.0543
0.1340	0.304	0.00827	0.167	0.147	0.153	0.036
0.1508	0.200	.00602	0.142	0.129	0.131	0.027
0.1675	0.135	.00489	0.122	0.106	0.119	0.201

Table E.1.6. Axial Variation of Mean Gas-Phase Temperature Decrement and Mean Mixture Fraction (or Total Freon-11 Concentration, $\bar{Y}_{Fc}/\bar{Y}_{Fo}$) in the Case 1 Evaporating Spray

x/d	$(\bar{T}_c-\bar{T}_\infty)/(\bar{T}_o-\bar{T}_\infty)^a$	$\bar{f}_c/\tilde{f}_o{}^b$
50	--	0.420
70	--	0.317
100	--	0.226
150	--	0.153
250	0.508	0.062
300	0.437	--
400	0.254	0.029
500	0.168	0.024
600	0.138	0.019

$^a\bar{T}_o$ = 261 K

$^b\tilde{f}_o$ = 1.0

Table E.1.7. Radial Variations of Mean Gas-Phase Temperature
Decrement in the Case 1 Evaporating Spray

r/x	$\frac{x/d = 250}{(\bar{T}-\bar{T}_\infty)/(\bar{T}_c-\bar{T}_\infty)}$	$\frac{x/d = 500}{(\bar{T}-\bar{T}_\infty)/(\bar{T}_c-\bar{T}_\infty)}$
0.0	1.0	1.0
0.0168	0.970	0.992
0.0335	0.939	0.902
0.0503	0.687	0.869
0.0670	0.603	0.803
0.0838	0.402	0.689
0.1005	0.346	0.623
0.1173	0.296	0.459
0.1340	0.229	0.344
0.1508	0.156	0.262
0.1675	0.089	0.197
0.1843	0.0502	0.131
0.2010	--	0.0656
0.2176	--	0.0492

Table E.1.8. Radial Variation of Mean Mixture Fraction
(or Total Freon-11 Concentration, $\tilde{Y}_F/\tilde{Y}_{Fc}$)
in the Case 1 Evaporating Spray

r/x	x/d = 50 $\tilde{f}/\tilde{f}_c$	x/d = 100 $\tilde{f}/\tilde{f}_c$	x/d = 250 $\tilde{f}/\tilde{f}_c$	x/d = 500 $\tilde{f}/\tilde{f}_c$
0.0	1.0	1.0	1.0	1.0
0.0168	0.987	0.981	0.984	0.984
0.0335	0.946	0.947	0.953	0.967
0.0503	0.880	0.860	0.840	0.915
0.0670	0.786	0.789	0.758	0.851
0.0838	0.731	0.677	0.628	0.760
0.1005	0.627	0.534	0.493	0.669
0.1173	0.506	0.421	0.411	0.548
0.1340	0.443	0.307	0.335	0.457
0.1508	0.341	0.263	0.269	0.385
0.1675	0.288	0.184	0.207	0.282
0.1843	0.229	0.121	0.172	0.209
0.2010	0.189	--	--	--
0.2180	0.131	--	--	--

E.2. Liquid-Phase Properties

Table E.2.1. Radial Variation of Liquid Flux and SMD
at x/d = 50 in the Case 1 Evaporating Spray

r/x	$\tilde{G}/\tilde{G}_c$	SMD (μm) (Slide Impaction)	SMD (μm) (Photographic)
0.00	1.00	30.3	31.3
0.05	0.96	30.2	31.2
0.10	0.68	28.7	31.7
0.15	0.42	31.5	29.4
0.20	0.12	30.9	30.4

$^a\tilde{G}_c$ = 5.332 kg/m^{2}s

Table E.2.2. Radial Variation of Drop Size Distributions at x/d = 50
for the Case 1 Evaporating Spray (Slide Impaction Results)

(Entries are Relative Percentage Number Frequency)

Diameter	0.00	6.36	12.72	19.08	25.44	31.80	38.16	44.52	50.88	57.24
Size Range	--	--	--	--	--	--	--	--	--	--
(μm)	6.36	12.72	19.08	25.44	31.80	38.16	44.52	50.88	57.24	63.60
r/x										
0.00	17.9	15.5	22.5	18.8	11.5	9.1	1.8	0.9	0.8	0.3
0.05	20.0	15.0	20.2	19.6	12.5	8.9	1.8	0.8	0.8	0.3
0.10	15.8	13.4	24.6	22.3	11.9	9.2	1.6	0.5	0.6	0.03
0.15	30.4	14.9	17.1	17.3	9.3	4.9	3.4	1.6	0.8	0.1
0.20	41.7	14.6	15.5	14.0	5.0	4.6	2.9	0.5	1.0	0.1

Table E.2.3. Radial Variation of Drop Size Distributions at x/d = 50
for the Case 1 Evaporating Spray (Photographic Results)

(Entries are Relative Percentage Number Frequency)

Diameter Size Range (μm)	15 -- 20	20 -- 25	25 -- 30	30 -- 35	35 -- 40	40 -- 45	45 -- 50	50 -- 55	55 -- 60
r/x									
0.00	14.7	33.1	26.9	11.3	7.2	4.2	1.5	0.8	0.3
0.05	19.4	29.5	26.4	11.3	7.5	3.1	1.8	0.6	0.4
0.10	17.5	30.4	26.7	11.0	6.5	5.1	1.8	0.7	0.4
0.15	21.8	34.2	26.2	10.6	2.3	2.9	1.3	0.6	0.2
0.20	23.0	33.1	22.4	9.7	4.3	5.8	1.2	0.6	--

Table E.2.4.   Initial Conditions of Mean Axial Drop Velocities
              (m/s) at x/d = 50 for the Case 1 Evaporating Spray

r/x	0.00	0.05	0.10	0.15	0.20
Diameter Size Range (μm)					
15-20	27.20	25.24	19.54	13.60	7.80
20-25	28.51	27.08	20.78	14.19	8.31
25-30	28.50	26.82	21.08	14.70	8.91
30-35	28.41	27.93	21.44	15.20	9.07
35-40	27.52	27.30	22.15	14.92	11.36
40-45	28.32	27.93	21.59	16.70	11.26
45-60	27.78	28.59	22.31	18.22	11.93

Table E.2.5.   Initial Conditions of Fluctuating Axial Drop Velocities
(m/s) at x/d = 50 for the Case 1 Evaporating Spray

r/x	0.00	0.05	0.10	0.15	0.20
Diameter Size Range (μm)					
15-20	2.01	2.45	2.60	2.57	3.05
20-25	2.34	2.78	2.81	2.51	2.90
25-30	2.27	2.85	2.79	3.01	3.82
30-35	2.56	2.09	3.57	3.55	3.56
35-40	2.06	2.96	3.43	2.58	4.59
40-45	2.32	2.24	2.16	1.98	3.20
45-60	1.66	2.18	2.52	2.31	4.65

Table E.2.6.   Axial Variation of Drop Size Distributions Along the Centerline
of the Case 1 Evaporating Spray (Photographic Results).

(Entries are Relative Percentage Number Frequency)

Diameter Size Range (μm)	15 -- 20	20 -- 25	25 -- 30	30 -- 35	35 -- 40	40 -- 45	45 -- 50	50 -- 55	55 -- 60
x/d									
100	18.66	29.69	24.74	11.48	8.22	4.41	2.05	0.63	0.12
150	21.87	30.07	25.13	12.26	7.22	2.15	0.86	0.43	--
250	22.72	31.44	25.90	11.53	5.79	1.49	1.12	--	--

Table E.2.7.   Axial Variation of SMD Along the
              Centerline of the Case 1 Evaporating Spray
              (Photographic Results)

x/d	SMD (μm)
100	31.50
150	29.61
250	28.74

Table E.2.8. Mean Axial Drop Velocities (m/s) Along the
Centerline of the Case 1 Evaporating Spray

x/d	100	150	250
Diameter Size Range (μm)			
15-20	16.5	12.9	8.1
20-25	16.3	13.2	8.2
25-30	16.8	13.5	8.7
30-35	17.6	14.0	9.4
35-40	18.0	14.7	9.8
40-45	17.8	15.5	9.8
45-60	19.8	16.9	9.9

Table E.2.9. Fluctuating Axial Drop Velocities (m/s) Along
the Centerline of the Case 1 Evaporating Spray

x/d	100	150	250
Diameter Size Range (μm)			
15-20	2.60	1.87	1.28
20-25	2.49	1.71	1.14
25-30	2.28	1.69	1.29
30-35	2.00	1.80	1.66
35-40	1.88	1.91	1.91
40-45	1.93	1.99	2.03
45-60	1.56	1.48	2.08

APPENDIX F

DATA FOR THE EVAPORATING SPRAY (CASE 2)

F.1 Gas-Phase Properties

Table F.1.1. Axial Variation of Centerline Velocity

x/d	$\bar{u}_c/\bar{u}_o$
40	0.590
50	0.538
70	0.495
100	0.419
150	0.307
250	0.234
400	0.117
500	0.095

Table F.1.2.   Radial Variation of Quantities

x/d = 50

r/x	$\bar{u}/\bar{u}_c$	$\overline{u'v'}/\bar{u}_c^2$	$\sqrt{\overline{u'^2}}/\bar{u}_c$	$\sqrt{\overline{v'^2}}/\bar{u}_c$	$\sqrt{\overline{w'^2}}/\bar{u}_c$	$\bar{k}/\bar{u}_c^2$
0.0	1.0	0.0	.156	.074	.075	.0177
0.0168	1.104	.00149	.161	.077	.077	.0189
0.0335	1.164	.00385	.162	.074	.077	.0188
0.0503	1.168	.00612	.178	.078	.083	.0223
0.0670	1.072	.00954	.208	.081	.090	.0289
0.0838	1.008	.0125	.239	.086	.093	.0366
0.1005	.885	.0170	.263	.092	.095	.0433
0.1173	.771	.0163	.274	.097	.103	.0475
0.1340	.657	.0187	.253	.097	.108	.0425
0.1508	.515	.0185	.249	.091	.093	.0395
0.1675	.463	.0136	.221	.092	.083	.0321
0.1843	.259	.0094	.169	.093	.077	.0216
0.2010	.142	.0042	.138	.084	.049	.0143
0.218	.091	.0028	.134	.082	.020	.0125

Table F.1.3.   Radial Variation of Quantities

x/d = 100

r/x	$\bar{u}/\bar{u}_c$	$\overline{u'v'}/\bar{u}_c^2$	$\sqrt{\overline{u'^2}}/\bar{u}_c$	$\sqrt{\overline{v'^2}}/\bar{u}_c$	$\sqrt{\overline{w'^2}}/\bar{u}_c$	$\bar{k}/\bar{u}_c^2$
0.0	1.0	0.0	0.218	0.116	0.117	0.0373
0.0168	0.995	0.00435	0.213	0.120	0.118	0.0368
0.0335	1.017	0.00614	0.214	0.111	0.120	0.0363
0.0503	1.032	0.00752	0.227	0.115	0.124	0.0401
0.0670	0.933	0.00838	0.229	0.117	0.132	0.0418
0.0838	0.828	0.0113	0.236	0.124	0.133	0.0444
0.1005	0.695	0.0102	0.233	0.127	0.127	0.0433
0.1173	0.567	0.00858	0.230	0.132	0.118	0.0421
0.1340	0.437	0.0082	0.209	0.127	0.103	0.0352
0.1508	0.291	0.00783	0.174	0.118	0.090	0.0262
0.1675	0.248	0.00713	0.138	0.117	0.086	0.0201
0.1843	0.172'	0.00556	0.127	0.110	0.082	0.0175
0.2010	0.118	0.00291	0.0995	---	---	---

Table F.1.4.   Radial Variation of Quantities

x/d = 250

r/x	$\bar{u}/\bar{u}_c$	$\overline{u'v'}/\bar{u}_c^2$	$\sqrt{\overline{u'^2}}/\bar{u}_c$	$\sqrt{\overline{v'^2}}/\bar{u}_c$	$\sqrt{\overline{w'^2}}/\bar{u}_c$	$\bar{k}/\bar{u}_c^2$
0.0	1.0	0.0	0.242	0.153	0.144	0.0514
0.0168	0.926	0.00434	0.232	0.154	0.150	0.0500
0.0335	0.825	0.00787	0.239	0.148	0.162	0.0526
0.0503	0.714	0.0107	0.226	0.146	0.174	0.0513
0.0670	0.621	0.0128	0.228	0.152	0.174	0.0527
0.0838	0.532	0.01022	0.185	0.157	0.143	0.0397
0.1005	0.400	0.00947	0.167	0.144	0.123	0.0319
0.1173	0.320	0.00879	0.159	0.132	0.108	0.0272
0.1340	0.250	0.00559	0.141	0.117	0.100	0.0218
0.1508	0.183	0.00435	0.124	0.108	0.086	0.0172
0.1675	0.118	0.00149	0.082	0.066	0.058	0.00722
0.1843	0.085	0.00078	0.069	0.061	--	--

Table F.1.5. Radial Variation of Quantities

x/d = 500

r/x	$\bar{u}/\bar{u}_c$	$\overline{u'v'}/\bar{u}_c^2$	$\sqrt{\overline{u'^2}}/\bar{u}_c$	$\sqrt{\overline{v'^2}}/\bar{u}_c$	$\sqrt{\overline{w'^2}}/\bar{u}_c$	$\bar{k}/\bar{u}_c^2$
0.0	1.0	0.0	0.291	0.237	0.248	0.1012
0.0168	0.902	0.00665	0.286	0.238	0.241	0.0983
0.0335	0.840	0.0117	0.285	0.232	0.240	0.0963
0.0505	0.764	0.0141	0.275	0.227	0.241	0.0926
0.067	0.699	0.0186	0.257	0.228	0.235	0.0866
0.0838	0.592	0.0185	0.245	0.215	0.227	0.0789
0.1005	0.45	0.0141	0.218	0.201	0.221	0.0684
0.1173	0.341	0.00978	0.174	0.177	0.181	0.0472
0.1340	0.256	0.00776	0.151	0.155	0.158	0.0359
0.1508	0.156	0.00708	0.141	0.133	0.146	0.0294
0.1675	0.101	0.00452	0.114	0.098	0.115	0.0179

Table F.1.6. Axial Variation of Mean Gas-Phase Temperature Decrement and Mean Mixture Fraction (or Total Freon-11 Concentration, $\tilde{Y}_{Fc}/\tilde{Y}_{FO}$) in the Case 2 Evaporating Spray

x/d	$(\bar{\tilde{T}}_c - \bar{\tilde{T}}_\infty)/(\bar{\tilde{T}}_O - \bar{\tilde{T}}_\infty)^a$	$\tilde{f}_c/\tilde{f}_O{}^b$
50	---	0.550
70	---	0.409
100	---	0.345
150	---	0.240
250	---	0.162
400	---	0.079
500	0.654	0.063
600	0.617	0.049

$^a\bar{\tilde{T}}_O = 268$ K

$^b\tilde{f}_O = 1.0$

Table F.1.7. Radial Variation of Mean Gas-Phase Temperature
Decrement in the Case 2 Evaporating Spray

r/x	$x/d = 250$ $(\bar{T}-\bar{T}_\infty)/(\bar{T}_c-\bar{T}_\infty)$
0.0	1.000
0.0168	0.900
0.0335	0.797
0.0503	0.651
0.0670	0.589
0.0838	0.495
0.1005	0.432
0.1173	0.380
0.1340	0.339
0.1508	0.260
0.1675	0.234
0.1843	0.177
0.2010	0.130
0.2176	0.093
0.2344	0.067

Table F.1.8. Radial Variation of Mean Mixture Fraction
(or Total Freon-11 Concentration, $\tilde{Y}_F/\tilde{Y}_{FC}$)
in the Case 2 Evaporating Spray

r/x	x/d = 50 $\tilde{f}/\tilde{f}_c$	x/d = 100 $\tilde{f}/\tilde{f}_c$	x/d = 250 $\tilde{f}/\tilde{f}_c$	x/d = 500 $\tilde{f}/\tilde{f}_c$
0.0	1.0	1.0	1.0	1.0
0.0168	0.935	0.992	0.988	0.984
0.0335	0.894	0.979	0.958	0.949
0.0503	0.855	0.920	0.880	0.901
0.0670	0.807	0.810	0.763	0.778
0.0838	0.733	0.726	0.579	0.611
0.1005	0.671	0.640	0.486	0.520
0.1173	0.589	0.535	0.403	0.419
0.1340	0.495	0.404	0.329	0.326
0.1508	0.435	0.305	0.259	0.251
0.1675	0.365	0.252	0.212	0.176
0.1843	0.307	0.184	0.170	0.154
0.2010	0.265	0.130	0.143	---
0.2180	0.191	---	---	---
0.2340	0.127	---	---	---

F.2. Liquid-Phase Properties

Table F.2.1. Radial Variation of Liquid Flux and SMD
at x/d = 50 in the Case 2 Evaporating Spray

r/x	$\tilde{G}/\tilde{G}_c$ [a]	SMD (μm) (Slide Impaction)	SMD (μm) (Photographic)
0.00	1.00	62.6	59.7
0.05	0.92	62.6	60.6
0.10	0.62	58.8	57.6
0.15	0.29	60.2	57.5
0.20	0.13	54.8	59.1

[a]$\tilde{G}_c$ = 7.413 kg/m^{2}s

Table F.2.2. Radial Variation of Drop Size Distributions at x/d = 50
for the Case 2 Evaporating Spray (Slide Impaction Results)

(Entries are Relative Percentage Number Frequency)

Diameter	0.00	6.36	12.72	19.08	25.44	31.80	38.16	44.52	50.88	57.24
Size Range	---	---	---	---	---	---	---	---	---	---
(μm)	6.36	12.72	19.08	25.44	31.80	38.16	44.52	50.88	57.24	63.60
r/x										
0.00	3.2	4.7	7.1	10.0	9.0	11.1	12.0	14.3	8.0	4.9
0.05	3.8	4.1	7.1	9.1	8.0	12.2	13.6	13.2	9.0	5.0
0.10	4.5	5.9	6.8	10.2	9.0⁻	13.1	15.0	12.3	7.4	4.3
0.15	4.2	5.7	6.5	9.0	8.3	14.0	16.0	11.0	9.0	3.0
0.20	5.0	6.2	7.1	10.4	10.0	13.5	16.4	11.8	7.0	3.1

(Continued)

Table F.2.2. Radial Variation of Drop Size Distributions at x/d = 50
for the Case 2 Evaporating Spray (Slide Impaction Results)

(Entries are Relative Percentage Number Frequency)

Diameter	63.60	69.96	76.32	82.68	89.04	95.4	101.76
Size Range	--	---	---	---	---	---	--
(μm)	69.96	76.32	82.68	89.04	95.4	101.76	108.12
r/x							
0.00	4.1	2.7	1.9	2.0	1.6	1.3	1.1
0.05	3.2	4.0	1.8	2.0	1.8	1.1	1.1
0.10	3.0	3.1	1.2	1.7	1.0	1.0	0.5
0.15	4.0	2.5	2.0	1.5	1.7	1.5	0.2
0.20	4.5	1.0	2.0	0.6	0.3	1.0	0.1

Table F.2.3   Radial Variation of Drop Size Distributions at x/d = 50
for the Case 2 Evaporating Spray (Photographic Results)

(Entries are Relative Percentage Number Frequency)

Diameter Size Range (μm)	10 --- 20	20 --- 30	30 --- 40	40 --- 50	50 --- 60	60 --- 70	70 --- 80	80 --- 90	90 --- 100	100 --- 110	110 --- 120
r/x											
0.00	2.85	21.61	20.23	19.98	18.11	8.26	3.85	2.66	1.73	0.50	0.22
0.05	2.72	13.41	23.17	23.22	16.32	10.46	5.37	3.03	1.47	0.60	0.21
0.10	2.51	20.41	25.64	20.93	14.67	7.46	5.14	1.61	0.93	0.44	0.26
0.15	2.88	31.91	23.87	16.49	10.94	6.13	3.38	2.45	1.24	0.58	0.13
0.20	4.44	32.22	20.49	12.66	15.66	4.64	6.14	1.42	1.25	0.97	0.09

Table F.2.4. Initial Conditions of Mean Axial Drop Velocities (m/s) at x/d = 50 for the Case 2 Evaporating Spray

r/x	0.00	0.05	0.10	0.15	0.20
Diameter Size Range (μm)					
10-20	19.80	20.34	14.92	6.67	1.94
20-30	19.97	20.56	15.05	7.10	2.24
30-40	21.15	21.16	15.96	9.29	3.56
40-50	20.68	22.01	16.91	12.10	4.09
50-60	21.12	22.55	17.41	13.80	5.65
60-70	20.28	21.84	17.70	14.68	6.44
70-80	20.52	21.38	18.02	15.35	7.39
80-90	19.34	20.96	17.91	15.79	8.93
90-100	18.81	20.24	18.33	16.30	10.88
100-120	19.53	19.90	18.26	16.20	11.31

Table F.2.5.   Initial Conditions of Fluctuating Axial Drop Velocities
(m/s) at x/d = 50 for the Case 2 Evaporating Spray

r/x	0.00	0.05	0.10	0.15	0.20
Diameter Size Range (μm)					
10-20	2.20	2.14	1.53	2.16	1.08
20-30	2.26	2.19	1.79	2.31	1.25
30-40	1.94	2.08	1.72	2.88	1.95
40-50	1.81	2.29	2.11	3.58	2.03
50-60	1.68	1.83	1.66	3.16	2.63
60-70	1.51	1.83	1.31	2.60	2.88
70-80	1.48	1.66	1.44	3.04	3.11
80-90	1.69	1.65	1.28	1.82	3.02
90-100	1.78	1.26	1.27	1.43	2.51
100-120	1.19	0.92	1.43	1.78	2.42

Table F.2.6.   Axial Variation of Drop Size Distributions Along the Centerline of the Case 2 Evaporating Spray (Photographic Results)

(Entries are Relative Percentage Number Frequency)

Diameter Size Range (μm)	10 --- 20	20 --- 30	30 --- 40	40 --- 50	50 --- 60	60 --- 70	70 --- 80	80 --- 90	90 --- 100	100 --- 110	110 --- 120
x/d											
100	5.66	19.93	19.50	18.11	18.37	9.67	4.27	2.87	0.84	0.53	0.27
150	5.21	17.19	19.34	18.01	19.41	11.41	4.44	3.35	0.95	0.45	0.24
250	6.18	14.47	15.76	19.27	18.79	13.45	6.25	3.64	1.66	0.51	0.04
400	4.00	12.78	12.16	20.45	20.89	14.60	6.81	4.40	2.35	1.56	---
500	6.07	13.96	15.75	20.70	19.58	15.19	7.27	1.34	0.15	---	---

Table F.2.7.   Axial Variation of SMD Along the Centerline
of the Case 2 Evaporating Spray
(Photographic Results)

x/d	SMD (µm)
100	59.5
150	60.2
250	62.1
400	65.2
500	57.8

Table F.2.8. Axial Variation of Mean Axial Drop Velocity (m/s)
              Along the Centerline of the Case 2 Evaporating Spray

x/d	100	150	250	400	500
Diameter Size Range (μm)					
10-20	15.6	11.9	7.7	3.9	3.0
20-30	15.8	11.8	7.8	4.3	3.2
30-40	15.9	11.7	8.7	4.7	3.4
40-50	16.0	12.8	8.0	5.1	3.6
50-60	16.8	11.8	8.0	5.5	3.9
60-70	16.0	11.7	8.2	6.0	3.6
70-80	15.9	11.6	8.6	6.3	4.0
80-90	15.1	12.4	8.8	5.8	4.2
90-100	15.7	12.3	8.9	6.9	4.4
100-110	15.7	12.7	9.3	7.2	---
110-120	15.7	13.1	10.1	---	---

Table F.2.9.   Axial Variation of Fluctuating Axial Drop Velocity (m/s) Along the Centerline of the Case 2 Evaporating Spray

x/d	100	150	250	400	500
Diameter Size Range (μm)					
10-20	2.61	2.14	1.24	0.98	0.75
20-30	2.48	2.24	1.45	0.92	0.80
30-40	2.53	2.32	1.69	0.88	0.84
40-50	2.26	2.27	1.77	0.89	0.87
50-60	2.37	2.86	1.68	0.94	0.86
60-70	2.00	2.67	1.68	1.07	0.88
70-80	1.84	2.13	1.75	1.26	0.91
80-90	1.70	1.72	1.63	1.38	0.98
90-100	1.86	1.54	1.36	1.44	1.11
100-110	1.55	1.61	1.37	1.49	---
110-120	1.62	1.88	1.57	---	---

1. Report No. NASA CR-174760	2. Government Accession No.	3. Recipient's Catalog No.
4. Title and Subtitle A Theoretical and Experimental Study of Turbulent Evaporating Sprays		5. Report Date September 1984
		6. Performing Organization Code
7. Author(s) A.S.P. Solomon, J-S. Shuen, Q-F. Zhang and G. M. Faeth		8. Performing Organization Report No. None
		10. Work Unit No.
9. Performing Organization Name and Address The Pennsylvania State University Mechanical Engineering Building University Park, Pennsylvania 16802		11. Contract or Grant No. NAG 3-190
		13. Type of Report and Period Covered Contractor Report
12. Sponsoring Agency Name and Address National Aeronautics and Space Administration Washington, D.C. 20546		14. Sponsoring Agency Code 505-31-42

15. Supplementary Notes

16. Abstract Measurements and analysis limited to the dilute portions of turbulent evaporating sprays, injected into a still air environment were completed. Mean and fluctuating velocities and Reynolds stress were measured in the continuous phase. Liquid phase measurements included liquid mass fluxes, drop sizes and drop size and velocity correlation. Initial conditions needed for model evaluation were measured at a location as close to the injector exit as possible. The test sprays showed significant effects of slip and turbulent dispersion of the discrete phase. The measurements were used to evaluate three typical models of these processes: (1) a locally homogeneous flow (LHF) model, where slip between the phases were neglected; (2) a deterministic separated flow (DSF) model, where slip was considered but effects of drop dispersion by turbulence were ignored; and (3) a stochastic separated flow (SSF) model, where effects of interphase slip and turbulent dispersion were considered using random-walk computations for drop motion. For all three models, a $k-\varepsilon$ model was used to find the properties of the continuous phase. The LHF and DSF models did not provide very satisfactory predictions for the present measurements. In contrast, the SSF model performed reasonably well--with no modifications in the prescription of eddy properties from its original calibration. Some effects of drops on turbulence properties were observed near the dense regions of the sprays. Treatment of such dense flow effects will require extension of the present SSF model. The SSF approach, however, appears to provide an attractive formulation for treating nonlinear interphase transport processes in drop-laden turbulent flows.

17. Key Words (Suggested by Author(s)) Spray modeling Turbulence interactions Combustor	18. Distribution Statement Unclassified - unlimited STAR Category 07
19. Security Classif. (of this report) Unclassified	20. Security Classif. (of this page) Unclassified	21. No. of pages 137	22. Price* A07

National Aeronautics and
Space Administration

Washington, D.C.
20546

Official Business
Penalty for Private Use, $300

SPECIAL FOURTH CLASS MAIL
BOOK

NASA

POSTMASTER: If Undeliverable (Section 158
Postal Manual) Do Not Return